Experimental Study of Highly Transient Thermo-Fluid Dynamic Phenomena in He II

by

Takeshi Shimazaki

A Doctoral dissertation presented to
the Doctoral Program in Engineering
University of Tsukuba

March 1996

ABSTRACT

EXPERIMENTAL STUDY OF HIGHLY TRANSIENT THERMO-FLUID DYNAMIC PHENOMENA IN He II

by Takeshi Shimazaki

Highly transient thermo-fluid dynamic phenomena are experimentally investigated with a superconductive temperature sensor. The characteristic time of quantized vortex development which is one of the governing parameters of the highly transient heat transport phenomena in He II is measured by analyzing the temperature profile data. The result suggests partial inadequacy of the vortex development equation presented by Vinen. It is found that the wave height variation of the second sound thermal shock wave well agrees with the prediction by the equal area rule if the effect of quantized vortex lines is neglected. Among three major heat transport processes, the second sound wave mode, the restricted thermal counterflow and evaporation, each contribution to the heat transport is quantitatively investigated. As a result, their contributions are found to be uniquely treated if the parameter $q_p t_H^{\frac{1}{2}}$ where q_p is the heat flux and t_H is the heating time is introduced.

Contents

Chapter 1

INTRODUCTION

The starting point of the study of liquid helium is the liquefaction of helium. Helium had been left as the last liquid which had not been able to be liquefied. But finally helium was successfully liquefied by Onnes in 1908. Through the so-called liquefaction competition low temperature production technique was greatly developed. Then low temperature physics developed strikingly during this period. Superconductivity was also discovered in 1927 by Onnes and the superfluidity of helium was discovered by Kapitza in 1927. Superconductivity and superfluidity are the typical phenomena which are regarded as the appearance of quantum effect in macroscopic level. Superfluidity is the unique property of He II. For instance He II flows through an extremely fine channel without any appreciable pressure drop as if it were an inviscid fluid. Its apparent thermal conductivity is several hundreds times higher than that of pure copper. It has several attractive properties for cryogen, and so it is expected to be the efficient coolant for superconducting magnets and space-borne infrared telescopes. A deep understanding of heat transport properties of superfluid helium is indispensable for such practical applications.

The unique properties which are interesting from the point of view of both quantum

physics and practical engineering are generally explained by the phenomenological macroscopic theory presented by Landau [1]. His phenomenological theory called the Landau two-fluid equations is the most successful theory to explain the superfluidity until now. He II is considered as being composed of two different fluid components, the normal fluid and superfluid components in this model. The normal fluid component behaves nothing but an ordinary classical Navier-Stokes fluid which has finite viscosity and entropy while the superfluid component does not. It has no viscosity and entropy. Since the superfluid component has no viscosity, those two components can flow without any appreciable interactions with each other. The two-fluid equations can give both qualitatively and quantitatively satisfactory explanations of steady heat transport phenomena in He II as long as the superfluid breakdown does not occur. The two-fluid equations lose its validity in the superfluid breakdown state, in which quantized vortices are generated and the mutual friction force between the normal fluid component and quantized vortices arises. The quantized vortices are generated and develop when the relative velocity between the normal fluid and superfluid components exceeds a certain threshold value. This situation corresponds to a heat flux which exceeds a threshold value is fed from a heat source to He II. The Gorter-Mellink mutual friction term [2] is usually introduced to the two-fluid equations to take account of the effect of the mutual friction force. However, the approach is found to be only valid to steady or quasi steady thermo-fluid dynamic phenomena. In the highly transient thermo-fluid dynamic phenomena where the time-scale of bulk thermo-fluid dynamic behavior gets to be comparable to or shorter than that of the evolution of quantized vortices, the effect of the development and decay of quantized vortices should be taken into account. The process of vortex development and decay was

treated on the basis of a phenomenological approach by Vinen [3][4][5] and numerically by Schwartz [6]. But those formulae can not completely explain some of extremely complicated behaviors of quantized vortices so the exact form of the formulae are still under consideration. Further investigations are still required to reveal the complete mechanism of highly transient heat transport phenomena in He II. The Vinen vortex line density equation is widely used in the study of transient thermo-fluid dynamic phenomena in He II. However the inadequacy of the equation especially in the case of intense pulsed heating has been pointed out these days.

As a result of the two-fluid nature, there exist two different modes of traveling sound waves. One is the first sound wave and the other is the second sound wave. First sound wave is the same as the ordinary sound wave. It is a pressure wave. The two fluid components move together in phase so He II moves with the same velocity of the components. On the other hand the two fluid components move in counter phase i.e. the two components move towards the opposite directions with the same speed so there is no net movement of He II as a whole in the case of the second sound wave. It can be said that the second sound wave is a traveling disturbance of entropy or a thermal wave. The second sound wave with finite amplitude nonlinearly develops into a thermal shock wave. It should be noted that due to the second sound wave, heat fed to He II from a heat source can be transported in a wave mode different from the usual diffusion process in He II. Propagation of the second sound wave or the thermal shock wave being a the typical example of the highly transient heat transport phenomena has been investigated by many researchers. Pioneering works on the propagation of the thermal shock wave and the effect of the interaction with quantized vortices have been carried out by Liepmann and Laguna

at California institute of technology [7]. Recently the theoretical investigations not only of the propagation of the second sound wave but also of the superfluid hydrodynamics with the effect of quantized vortices have been carried out by Nemirovskii at the Institute of the Thermophsics [8]. And extensive experimental and numerical investigations of thermal shock wave and tangled mass of quantized vortices are carried out by the group of the Max-Planck-Institut [9].

Through those investigations, the development and the decay of the quantized vortices are recognized as governing phenomena on transient heat transport. The high density quantized vortices cause dissipative effect on the heat transport in He II. But some aspects of the effects of quantized vortices on the heat transport still remain open questions. The propagation property of a thermal shock wave and its interaction with quantized vortices have been investigated in a couple of experiments [10] but the resolution of the measuring devices used in those experiments such as a temperature sensor and a visualizing technique are not sufficient to detect the complete shape of a propagating thermal shock wave.

The objective of this study is to experimentally investigate the highly transient thermo-fluid dynamic phenomena in superfluid helium for the practical application of He II. In this study a thin film superconductive temperature sensor which possesses high temperature sensitivity and quick response time is used. It allows a high resolution temperature measurement both in time and space. Complete wave form variation of a thermal shock wave during propagation can be measured with the superconductive temperature sensor. The propagation property of a thermal shock wave is investigated by the direct measurement of the wave form variation. The experimental results are compared with a theoretical prediction. Moreover, a thermal shock wave is utilized as a probe to diagnose

the behavior of quantized vortices. The deformation of a thermal shock wave due to the interaction with quantized vortices is carefully observed to measure the characteristic time of the development of quantized vortices which is one of the most important governing parameters of the highly transient heat transport phenomena. The characteristic time in the case of very large heat flux heating in which the characteristic time had not been measured in the other experiments is attempted to be measured. The development of quantized vortex lines in these cases is found to have different characteristics from that in the case of small heat flux heating. In the case of a pulsed heating with a large heat flux, high density quantized vortices are generated and a thermal boundary layer is formed in the vicinity of a heating surface. Even boiling in the layer is observed in some case. The thermal situation resembles that upon a superconducting magnet quench. The study of the heat transport phenomena in such case is indispensable to investigate the stability of superfluid cooled superconducting magnets. The heat transport property of He II in such situation is quantitatively investigated including the effects of the second sound wave mode heat transport which could not be measured by means of the conventional temperature sensors.

Chapter 2

THEORETICAL BACKGROUND

2.1 Superfluid helium

The phase diagram of helium is schematically shown in Fig. 2.1. It is very interesting to note that helium has two liquid phases. Helium liquefies at $4.2K$, and at $2.17K$ liquid helium exhibits another transition into the another liquid phase. The first liquid phase between $4.2K$ and $2.17K$ is called He I which behaves like an ordinary viscous fluid. The second liquid phase below $2.17K$ is called He II or superfluid helium having unique properties called superfluidity. The transition temperature of $2.17K$ is called the λ -temperature, T_λ and boundary line between He I and He II is named the λ -line. One of the unique properties of He II, the superfluidity, is superleak. It can flow through extremely fine capillaries and narrow slit without producing any appreciable pressure drop. It behaves like an inviscid fluid.

Unusual hydrodynamic behavior of He II is well explained in terms of the two-fluid model introduced by Tisza [12], which was then led to Landau tow-fluid equation [1]. In

this model He II is considered as a mixture of two fluid components, the normal fluid component with non-zero viscosity and superfluid component with zero viscosity. The normal fluid component can be considered to correspond to the excited portion of helium so it associates with entropy (see Fig. 2.2). On the other hand the superfluid component corresponds to helium atoms which occupy the quantum ground state, Bose-Einstein condensation phase, so it does not associate with entropy. The ratios of the normal fluid density and superfluid density to the total density are given as a function of temperature. Below T_λ the density of superfluid component increases as helium temperature decreases. Fig. 2.3 shows these density ratios as a function of temperature under saturated vapor pressure condition. The superfluid component can flow freely in narrow channel though the normal fluid component is clamped owing to its viscosity. Consequently, superfluid helium seems to be able to flow extremely fine channel.

Another typical example of the superfluidity is the thermal counterflow. Suppose two vessels containing He II are connected by a tube, one of which has a heater as shown in Fig. 2.4. If the heater is switched on, the superfluid component flows towards the heater due to the gradient of the chemical potential. It in contact with the heater absorbs heat, and then it turns into the normal fluid component. The normal fluid component flows towards the another vessel, being at the opposite end of the tube, owing to mass conservation. The two fluid components flow towards the opposite directions with the same speed. There is no net flow of He II in the flow system as a while. The superfluid and normal fluid components flowing in the opposite direction in the tube cause no interaction with each other because the superfluid component has no viscosity. As a result, heat is extremely efficiently transported by the normal fluid component. The

flow is called internal convection or thermal counterflow and is a key mechanism for the apparently high thermal conductivity of He II. The relative velocity between the normal fluid and superfluid components in the thermal counterflow is in proportion to the heat flux from a heater as long as the applied heat flux is not so large. However if the heat flux which is larger than a certain critical value is applied, the relative flow velocity exceeds a threshold value and then quantized vortices are generated. Quantized vortices interact with the normal fluid component and generate mutual friction force. The relative velocity can not be proportional to the heat flux. Dissipative effects arise in the flow. This is the superfluid breakdown.

2.2 Landau two-fluid equations

The basic hydrodynamic equations for He II in the case that dissipative effects are absent are first introduced by Landau [1]. The equations consist of the law of the mass, entropy and momentum conservations. Since superfluid helium consists of two interpenetrating fluid components, two momentum equations are required. The densities of the normal fluid and superfluid components are denoted by ρ_n and ρ_s, respectively. And each component is assigned its own velocity field of $\vec{v}_n$ and $\vec{v}_s$. The total density of He II, ρ is defined by $\rho = \rho_n + \rho_s$. The equation of conservation of mass is

$$\frac{\partial \rho}{\partial t} + \mathrm{div}\vec{j} = 0, \tag{2.1}$$

where $\vec{j} = \rho_s \vec{v}_s + \rho_n \vec{v}_n$. The total mass flow is expressed by the sum of the flows of normal fluid and superfluid components.

Since dissipation is neglected and the entropy is transported only by the normal fluid

component, the equation of conservation of entropy takes the form

$$\frac{\partial(\rho s)}{\partial t} + \mathrm{div}(\rho s \vec{v}_n) = 0. \tag{2.2}$$

The flow of superfluid component is driven by the gradient of chemical potential. The momentum equation for the superfluid component is

$$\frac{D\vec{v}_s}{Dt} + \nabla\mu = 0, \tag{2.3}$$

where μ is the chemical potential per volume of He II and its gradient is given as follows

$$\nabla\mu = \frac{\nabla P}{\rho} - S\nabla T - \frac{\rho_n}{2\rho}\nabla(\vec{v}_n - \vec{v}_s)^2.$$

Here, the equation for the total momentum is introduced.

$$\frac{\partial \vec{j}_i}{\partial t} + \frac{\partial \boldsymbol{\Pi}_{ik}}{\partial x_k} = 0, \tag{2.4}$$

where $\Pi_{ik} = P\delta_{ik} + \rho_n v_{ni} v_{nk} + \rho_s v_{si} v_{sk}$ is the momentum flux density tensor.

Now it is clear that the Landau two-fluid equations form a closed set of eight equations for eight independent variables.

2.3 Quantized vortices

When the relative velocity between the normal fluid and superfluid components v_{ns} exceeds a certain critical value (it is approximately several m/s though it depends on the size of a flow channel), quantized vortices are generated. The normal fluid component interacts with quantized vortices and mutual friction force arises. As a result, energy dissipation gets to be significant in the He II flow, that is to say superfluid breakdown. The appearance of quantized vortex lines in He II is one of the macroscopic manifestation

of quantum effects. One of the striking feature of them is that the circulation around a vortex line is quantized with quantum number of 1

$$\kappa = \frac{h}{m_4} n \qquad (n = 1), \tag{2.5}$$

where h is the Planck constant, m_4 is the mass of a helium atom and n is the quantum number. That is why vortex lines in He II are called quantized vortex lines. It is known that the radius of vortex core is 1.3Å. The origin of quantized vortex lines is still an open question.

It has been stated that the Gorter-Mellink mutual friction term F_{ns} [2] could be added to the momentum equations to take the mutual friction into account,

$$\vec{F}_{ns} = \rho_n \rho_s A(T)(v_{ns} - v_0)^2 \vec{v}_{ns}, \tag{2.6}$$

where $A(T)$ is the Gorter-Mellink constant, v_0 is the critical relative velocity. This approach can give appropriate results both qualitatively and quantitatively for steady or quasi-steady thermo-fluid dynamic phenomena. It is, however, known that this approach loses applicability for highly transient cases. When the time scale of the bulk thermo-fluid dynamic phenomena becomes comparable to or shorter than that of the characteristic time of evolution of vortex tangle, the development and decay of quantized vortices should be taken into account. The behavior of quantized vortices was first noted by Feymann [13] and then was formulated by Vinen [3][4][5] from phenomenorogical consideration. Vinen observed the temperature gradient and variation in the attenuation of second sound wave in a long rectangular channel when the weak heat current ($q_p \leq 0.4 W/cm^2$) is applied. The characteristic time of vortex development τ_{vinen} is empirically found to be given as a function of applied heat flux as follows

$$\tau_{vinen} = a'(T_B) q_p^{-3/2}, \tag{2.7}$$

where $a'(T_B)$ is the factor experimentally obtained as a function of temperature. It is observed that quantized vortices start to decay when heater is switched off. Vinen deduced the vortex line density equation which is the dynamic balance equation of generation and decay of vortex lines,

$$\frac{dL}{dt} = \alpha \left| v_{ns} \right| L^{3/2} - \beta L^2 + \gamma \left| v_{ns} \right|^{5/2}, \tag{2.8}$$

where L is the vortex line density which is defined as the total vortex line length per unit volume. α and β are the growth and decay coefficients given by Vinen, and γ is calculated from experimental value of $a'(T_B)$ and thermodynamical properties of He II. The first term of the right hand side of this equation describes the generation of quantized vortices and the second one does the decay of quantized vortices. The third term is the source term of the vortex. Without this term the vortex density never develops if the initial vortex density $L = 0$. The Vinen vortex line density equation has been widely used in many investigations but, in these days, its inadequacy to the cases of large heat flux is pointed out.

2.4 Propagation of wave in He II

The structure of the two-fluid Eq.s (2.1)-(2.4) suggests that there are two kinds of propagating wave modes. The first experimental confirmation was provided by Peshkov [14] in 1944. It was the first striking evidence of the applicability for the two fluid idea.

The following notations are introduced to investigate the propagation of small disturbances [15]. The small deviation from a steady state is denoted by δ and the constant equilibrium value is denoted by subscript zero in which $\vec{v}_s = \vec{v}_n = 0$.

$$\rho = \rho_0 + \delta\rho\left(\vec{r}, t\right), \qquad s = s_0 + \delta s\left(\vec{r}, t\right),$$

$$P = P_0 + \delta P\,(r,t)\,, \qquad T = T_0 + \delta T\,(\vec{r},t)\,,$$

$$\vec{v}_n = \delta\vec{v}_n\,(\vec{r},t)\,, \qquad \vec{v}_s = \delta\vec{v}_s\,(\vec{r},t)\,. \tag{2.9}$$

Using above notations and neglecting all terms quadratic in the small quantities the two-fluid equations are linearized and become as follows.

$$\frac{\partial\delta\rho}{\partial t} \quad +\rho_{n,0}\nabla\cdot\delta\vec{v}_n + \rho_{s,0}\nabla\cdot\delta\vec{v}_s = 0, \tag{2.10}$$

$$\rho_0\frac{\partial\delta s}{\partial t} \quad +s_0\frac{\partial\delta\rho}{\partial t} + \rho_0 s_0\nabla\cdot\delta\vec{v}_n = 0, \tag{2.11}$$

$$\frac{\partial\delta\vec{v}_s}{\partial t} \quad -s_0\nabla\delta T + \frac{1}{\rho_0} + \nabla\delta P = 0, \tag{2.12}$$

$$\rho_{n,0}\frac{\partial\delta\vec{v}_n}{\partial t} \quad +\rho_{s,0}\frac{\partial\delta\vec{v}_s}{\partial t} + = -\nabla\delta P. \tag{2.13}$$

Now longitudinal traveling waves with the frequency ω and the wave number k_0 are introduced to investigate the response of He II to small disturbances.

$$\begin{aligned} T &= T_0 + T'\exp\left(ik_0x - i\omega t\right), \\ P &= P_0 + P'\exp\left(ik_0x - i\omega t\right), \\ \vec{v}_n &= v_n'\exp\left(ik_0x - i\omega t\right)\vec{e}_x, \\ \vec{v}_s &= v_s'\exp\left(ik_0x - i\omega t\right)\vec{e}_x, \end{aligned} \tag{2.14}$$

where $\vec{e}_x$ is a unit vector in the x direction. A set of four homogeneous equations are obtained by substituting these expressions of monochromatic wave into Eq.s (2.10)-(2.13). Then we get

$$-i\omega\frac{\partial\rho}{\partial P}P' \quad -i\omega\frac{\partial\rho}{\partial T}T' + ik_0\rho_{n,0}v_n' + ik_0\rho_{s,0}v_s' = 0, \tag{2.15}$$

$$-i\omega\frac{\partial\rho s}{\partial P}P' \quad -i\omega\frac{\partial\rho s}{\partial T}T' + ik_0\rho_0 s_0 v_n' = 0, \tag{2.16}$$

$$i\frac{k_0}{\rho_0}P' \quad -ik_0 s_0 T' - i\omega v_s' = 0, \tag{2.17}$$

$$ik_0P' \quad -i\omega\rho_{n,0}v_n' - i\omega\rho_{s,0}v_s' = 0. \tag{2.18}$$

The set of the equations requires that its determinant must vanish for the existence of a non-trivial solution. Then a dispersion law in quadratic in u^2 is derived. (see appendix A for the derivation)

$$\left(1-\frac{u^2}{u_1^2}\right)\left(1-\frac{u^2}{u_2^2}\right)=1-\frac{C_V}{C_P}, \tag{2.19}$$

where

$$C_V = T\left(\frac{\partial s}{\partial T}\right)_\rho, \quad C_P = T\left(\frac{\partial s}{\partial T}\right)_P,$$
$$u^2 = \frac{\omega^2}{k_0^2}, \quad u_1^2 = \left(\frac{\partial P}{\partial \rho}\right)_s, \quad u_2^2 = \frac{\rho_s s^2 T}{\rho_n C_V}. \tag{2.20}$$

It should be noted that the right hand side of Eq. (2.19) can be neglected at temperatures and pressures under consideration. Then the solution of Eq. (2.19) is given

$$u = u_1 = \left(\frac{\partial P}{\partial \rho}\right)_s^{1/2}, \tag{2.21}$$

$$u = u_2 = \left(\frac{\rho_s s^2 T}{\rho_n C_V}\right)_s^{1/2}. \tag{2.22}$$

Two modes of propagating waves having different propagation speeds are obtained. Here, u_1 and u_2 are called the first and second sounds, respectively. The first sound wave corresponds to an ordinary sound in Euler fluid. It is important to note that in this sound wave mode the normal fluid and superfluid components move in phase. It is a propagating density fluctuation having a propagation speed of approximately $230m/s$. The propagation speed of first sound wave as a function of temperature is shown in Fig. 2.5. On the other hand the second sound wave is a quite unique sound which appears only in He II. There is no center of mass motion but a relative motion between the normal fluid and superfluid components. Since the normal fluid component associates with the entropy and the superfluid component does not, the second sound wave can be regarded as a propagating entropy fluctuation or a thermal wave. Its propagating speed is a strong

function of temperature but typically is $20m/s$ as shown in Fig. 2.6 . It is very interesting to note that heat can be transported in a wave form in He II. Internal convection (thermal counterflow) can be regarded as the second sound wave of frequency zero.

2.5 Thermal shock wave

The expressions of the propagation speed of two independent linear wave modes are obtained by linearizing the two-fluid equations in the last section. Within this approximation all the points of the wave profile are assumed to propagate with the same speed. But this assumption can be applied only when the amplitude of the wave is small. For the wave with finite amplitude, the nonlinear terms of the two-fluid and thermodynamic equations are not negligible and provide the different propagation speed for the point of different amplitude in the wave. Then the points with higher propagation speed catch up the points with slower propagating speed through propagation. As a result, the wave steepens the some portion of the wave profile and ultimately becomes a shock wave.

The propagation speed with nonlinear effects can be investigated by solving the two-fluid and thermodynamic equations up to second order in the deviation from the equilibrium state [15]. The two-fluid equations on the one dimensional case can be written in following form by keeping the terms up to second order.

$$-u\frac{\partial\rho}{\partial P}\frac{\partial P}{\partial x}-u\frac{\partial\rho}{\partial T}\frac{\partial T}{\partial x}-2uw\frac{\partial\rho}{\partial w^2}\frac{\partial w}{\partial x}+\rho\frac{\partial v}{\partial x}+v\frac{\partial\rho}{\partial x}=0, \tag{2.23}$$

$$\left[-\rho u\frac{\partial s}{\partial P}+\rho v_n\frac{\partial s}{\partial P}+ws\frac{\partial\rho_s}{\partial P}\right]\frac{\partial P}{\partial x}+\left[\rho-u\rho\frac{\partial s}{\partial T}\rho v_n\frac{\partial s}{\partial x}+ws\frac{\partial\rho_s}{\partial T}\right]\frac{\partial T}{\partial x}+\left[-2uw\rho\frac{\partial s}{\partial w^2}+\rho_s s\right]\frac{\partial w}{\partial x}=0, \tag{2.24}$$

$$\left[uw\frac{\partial(\rho_n/\rho)}{\partial P}+\frac{1}{\rho}\right]\ \frac{\partial P}{\partial x}+\left[u\frac{\partial(\rho_n/\rho)}{\partial T}-s\right]\frac{\partial T}{\partial x}$$
$$+\left[v-u-\frac{\rho_n}{\rho}w\right]\ \frac{\partial v}{\partial x}+\left[\frac{\rho_n}{\rho}u-\frac{\rho_n\rho_s}{\rho^2}w-\frac{\rho_n}{\rho}v\right]\frac{\partial w}{\partial x}=0, \tag{2.25}$$

$$\frac{\partial P}{\partial x}+[-\rho u+\rho v]\frac{\partial v}{\partial x}+\frac{2\rho_n\rho_s}{\rho}w\frac{\partial w}{\partial x}=0, \tag{2.26}$$

where $w\equiv v_n-v_s$ is the relative velocity between normal fluid and superfluid components, v is the velocity of the net mass flow of He II. Again the longitudinal traveling wave with frequency ω and wave number k_0 are introduced. The Eq.s (2.23), (2.24), (2.25) and (2.26) become a set of four homogeneous equations in the four unknown variables P', T', v' and w'. In order for the existence of the nontrivial solution of the homogeneous equations the determinant must vanish. It is the same situation as the derivation of the sound propagation speed in first order of deviation from the equilibrium state in the last section. Then the equation of dispersion law is give by

$$\begin{aligned}(u^2-u_1^2)(u^2-u_2^2) &+ 2u^3w\left[-\frac{2\rho_s}{\rho}+\frac{s}{\rho_n}\frac{\partial\rho_n}{\partial T}\left(\frac{\partial s}{\partial T}\right)^{-1}\right]\\ &+ 2uw\left(\frac{\partial\rho}{\partial P}\right)^{-1}\left[\frac{2\rho_s}{\rho}-\frac{s}{\rho_n}\frac{\partial\rho_n}{\partial T}\left(\frac{\partial s}{\partial T}\right)^{-1}\right]=0.\end{aligned} \tag{2.27}$$

Two modes of propagating waves are obtained.

$$u = u_1 \tag{2.28}$$

$$u = u_2+\left[\frac{2\rho_s}{\rho}-\frac{s}{\rho_n}\frac{\partial\rho_n}{\partial T}\left(\frac{\partial s}{\partial T}\right)^{-1}\right]w \tag{2.29}$$

It can be seen that there is no difference in the expressions of first sound wave between those in the first order and the second order. However several correction terms which are linear in the equilibrium relative velocity w are added to the second sound wave in the first order. In Eq. (2.29), the second term of the right hand side which is evaluated by the values in the equilibrium state gives the correction of the deviation of the propagation

speed of the point with relative velocity of w from the u_2 which is evaluated in the first order. It is practically convenient that all terms in Eq. (2.29) are evaluated by the values in the equilibrium state. u_2 can be expressed by

$$u_2 = u_{2,0} + \frac{\partial u_2}{\partial T}\frac{dT}{dw}w + \frac{\partial u_2}{\partial P}\frac{dP}{dw}w, \tag{2.30}$$

where $u_{2,0}$ is the propagation speed of second sound wave in the equilibrium state. From Eq.s (2.15) and (2.18) the relation between T' and v_s' can be obtained.

$$\left(\frac{\partial \rho}{\partial P} - \frac{k_0^2}{\omega^2}\right) P' + \frac{\partial \rho}{\partial T} T' = 0 \tag{2.31}$$

From Eq. (2.17) P' can be written

$$P' = \rho_0 u (v_s' + \frac{1}{u} s_0 T'). \tag{2.32}$$

Substituting this into Eq. (2.31)

$$\left(\frac{\partial \rho}{\partial P} - \frac{1}{u^2}\right) (\rho_0 u v_s' + \rho_0 s_0 T') + \frac{\partial \rho}{\partial T} T = 0. \tag{2.33}$$

The relation between T' and v_s' is obtained.

$$T' = \frac{\rho_0 u \left(1 - u^2 \dfrac{\partial \rho}{\partial P}\right)}{u^2 \dfrac{\partial \rho}{\partial T} - \rho_0 s_0 \left(1 - u^2 \dfrac{\partial \rho}{\partial P}\right)} \tag{2.34}$$

Since at most temperature (i.e. $T_B > 0.8K$)

$$\left(\frac{\partial \rho}{\partial T}\right) \ll 1, \tag{2.35}$$

it can be ignored in the present order of the approximation. From Eq. (2.34) the following relation is obtained at lowest order

$$T' = -\frac{u_2}{s} v_s'. \tag{2.36}$$

Using the identity

$$v_s = v - \frac{\rho_n}{\rho} w,$$

Eq. (2.36) becomes

$$T' = -\frac{u_2}{s}\left(v' - \frac{\rho_n}{\rho} w\right). \tag{2.37}$$

For second sound wave, pressure variation can be neglected and the velocity of the net mass flow of He II $v \approx 0$. Substituting Eq. (2.37) into Eq. (2.30), u is evaluated by the values in the equilibrium state.

$$u = u_{2,0} + \left[\frac{\rho_n u_2}{\rho s} + \frac{\partial u_2}{\partial T} + \frac{2\rho}{\rho} - \frac{s}{\rho_n}\frac{\partial \rho_n}{\partial T}\left(\frac{\partial s}{\partial T}\right)^{-1}\right] w. \tag{2.38}$$

Using Eq.s (2.20) and ignoring small terms, final form of the propagation speed of the second sound wave in the second order of the deviation from the equilibrium state is obtained.

$$u = u_{2,0} + \frac{sT}{C_V}\left[\frac{\partial}{\partial T}\log\left(u_2^3 \frac{\partial s}{\partial T}\right)\right] v_n. \tag{2.39}$$

Here the coefficient of v_n is written

$$B = \frac{sT}{C_V}\left[\frac{\partial}{\partial T}\log\left(u_2^3 \frac{\partial s}{\partial T}\right)\right]. \tag{2.40}$$

B is called steeping coefficient which represents the intensity of the nonlinear effect on the propagating speed of the point with a certain amplitude. The variation of B as a function of temperature is given Fig. 2.7. The sign of the nonlinear coefficient of propagation speed of disturbance in aerodynamics usually takes positive. And the case in which coefficient takes negative is quite unusual. The normal fluid velocity v_n and the temperature variation ΔT are related to the applied heat flux q_p by the equations,

$$\begin{aligned} v_n &= q_p/\rho s T, \\ \Delta T &= \rho C_P u_{2,0}. \end{aligned} \tag{2.41}$$

Then the relation between v_n and ΔT are given by

$$v_n = \frac{u_{2,0} C_P}{sT} \Delta T. \tag{2.42}$$

Substituting Eq. (2.42) into Eq. (2.39), it is rewritten in terms of ΔT

$$u = u_{2,0} + u_{2,0} \left[\frac{\partial}{\partial T} \log \left(u_2^3 \frac{\partial s}{\partial T} \right) \right] \Delta T. \tag{2.43}$$

It is very interesting that B can be both positive and negative depending on the temperature in He II. The reason of the existence of the nonlinear coefficient with negative sign is the strong temperature dependence of the physical property of He II. When B is positive the points with larger amplitude travel faster than those with smaller amplitude. Wave peak will catch up troughs through propagation. As a result discontinuity is formed at the leading edge of a traveling wave form. This is called frontal shock wave and is familiar in the aerodynamics. The schematic drawings of a frontal thermal shock wave is shown in Fig. 2.8. On the other hand when B is negative, the points with smaller amplitude will catch up those with larger amplitude. Then the discontinuity is formed at the trailing edge of the wave profile. This is called back shock wave which is hardly seen in aerodynamics (see Fig. 2.8). There can exist one more interesting form of a thermal shock wave in He II. At $T_B = 1.87K$ B vanishes and B changes its sign when temperature crosses $T_B = 1.87K$. If the second sound wave with sufficiently large amplitude to cross the temperature $T_B = 1.87K$ is generated at just below the temperature, the discontinuities are formed on both sides of the wave profile. It is also shown in Fig. 2.8. This is called double shock wave.

2.6 Wave form variation through propagation

The propagation speed of a thermal shock wave is given by one half the sum of the speed of sound on the both leading and trailing edges of the shock wave, that is Eq. (2.39), as

$$u = u_{2,0} + \frac{1}{2}\frac{sT}{C_V}\left[\frac{\partial}{\partial T}\log\left(u_2^3\frac{\partial s}{\partial T}\right)\right]v_n. \tag{2.44}$$

For simplicity it is rewritten as

$$u = u_{2,0} + Bv_n/2. \tag{2.45}$$

Substituting Eq. (2.42) into Eq. (2.44), the propagation speed of a thermal shock wave is given in terms of the temperature variation ΔT.

$$u = u_{2,0} + \frac{1}{2}u_{2,0}\left[\frac{\partial}{\partial T}\log\left(u_2^3\frac{\partial s}{\partial T}\right)\right]\Delta T. \tag{2.46}$$

For simplicity it is rewritten as

$$u = u_{2,0} + b\Delta T/2, \tag{2.47}$$

where

$$b = u_{2,0}\left[\frac{\partial}{\partial T}\log\left(u_2^3\frac{\partial s}{\partial T}\right)\right].$$

Without any dissipative effects, the energy within a thermal pulse is conserved through propagation and the wave form variation occurs only due to the hydrodynamic nonlinearity. It is known that the propagation of a second sound wave with a finite amplitude is subjected to the Burgers equation in the former work of approximation in the second order of the smallness from equilibrium state [10][24].

$$\frac{\partial v_n}{\partial t} + (u_{2,0} + Bv_n)\frac{\partial v_n}{\partial x} = \mu_2\frac{\partial^2 v_n}{\partial x^2}, \tag{2.48}$$

where

$$\mu_2 = \frac{\rho_s}{2\rho\rho_n}\left(\frac{4}{3}\eta + \zeta_2 - 2\rho\zeta_1 + \rho^2\zeta_3 + \frac{\rho_n x}{\rho_s C}\right), \tag{2.49}$$

where η, ζ_1, ζ_2 and ζ_3 are the viscosity coefficients. The equal area rule which is equivalent to the result of the Burgers equation can be applied for the wave form variation through propagation. The wave form variation of a trapezoidal heat pulse is considered on the basis of the equal area rule in the following. The process of wave form variation is divided into two stages bounded by the formation of a triangular profile.

The wave form variation before the formation of a triangular profile in the case of positive B-factor is schematically drawn in Fig. 2.9. This profile shows the spatial distribution of temperature. Suppose a trapezoidal heat pulse with an initial amplitude of ΔT_0. The wave is propagating from left side to right side. The spatial length of the rising, the plateau and the falling portions of the wave profile are denoted by l_a, l_b and l_c, respectively. The time duration corresponding to those portions are given using $u_{2,0}$ by

$$\begin{aligned} t_{shol} &= \frac{l_a}{u_{2,0}} = \frac{l_c}{u_{2,0}}, \\ t_{plat} &= \frac{l_b}{u_{2,0}}. \end{aligned} \tag{2.50}$$

The propagation speed at the points B: $u_{2,0} + b\Delta T_0$, and at A: $u_{2,0}$ do not change through the process. But those of the points C: $u_{2,0} + b\Delta T_0$ and D: $u_{2,0}$ change to $u_{2,0} + b\Delta T_0/2$ when temperature discontinuity is formed. The point C travels with the speed of $b\Delta T_0$ relative to the point D so the point C catches up the point D during propagation. The time interval denoted by $t_{C\to D}$ is

$$t_{C\to D} = \frac{u_{2,0} t_{shol}}{b\Delta T_0}. \tag{2.51}$$

That when the point B catches up the points C and D, the trapezoidal profile becomes the triangular profile. $t_{B\to D}$ which is the time interval needed for the point B to catch

up the points C and D is considered next. Since the propagation speed at the point D changes from $u_{2,0}$ to $u_{2,0} + b\Delta T/2$ at which the point C catches up, $t_{B\to D}$ is divided into $t_{B\to D1}$ and $t_{B\to D2}$ in the evaluation. The point B travels with the speed of $b\Delta T_0$ relative to the point D so $t_{B\to D1}$ is given by

$$\begin{aligned} t_{B\to D1} &= t_{C\to D} - t_{plat} \\ &= \frac{u_{2,0}t_{shol}}{b\Delta T_0} - t_{plat}. \end{aligned} \tag{2.52}$$

Initial distance between the point D and the point B is $(t_{shol} + t_{plat})u_{2,0}$ and the relative speed of the point B to the point D becomes $b\Delta T_0/2$ after the formation of discontinuity. Then the following equation is obtained.

$$(t_{shol} + t_{plat})u_{2,0} = t_{B\to D1}b\Delta T_0 + t_{B\to D2}b\Delta T_0/2 \tag{2.53}$$

$t_{B\to D2}$ is given by

$$\begin{aligned} t_{B\to D2} &= \frac{2}{b\Delta T_0}\left[(t_{shol} + t_{plat})u_{2,0} - \left(\frac{u_{2,0}t_{shol}}{b\Delta T_0} - t_{plat}\right)b\Delta T_0\right] \\ &= \frac{2}{b\Delta T_0}\left[(u_{2,0} + b\Delta T_0)t_{plat}\right] \\ &= \frac{2u_{2,0}t_{plat}}{b\Delta T_0} + 2t_{plat}. \end{aligned} \tag{2.54}$$

As a result the total time $t_{trape\to tri}$ needed to change a trapezoidal heat pulse into a triangular profile is

$$\begin{aligned} t_{trape\to tri} &= t_{shol} + t_{plat} + \frac{u_{2,0}t_{shol}}{b\Delta T_0} - t_{plat} + \frac{2u_{2,0}t_{plat}}{b\Delta T_0} + 2t_{plat} \\ &= \frac{u_{2,0}}{b\Delta T_0} + (t_{shol} + 2t_{plat}) + 2t_{plat} + t_{shol}. \end{aligned} \tag{2.55}$$

The propagating distance $Z_{trape\to tri}$ of the heat pulse through the wave form change from trapezoidal to triangular is given by

$$Z_{trape\to tri} = \left[(t_{shol} + t_{plat}) + t_{B\to D1}\right]u_{2,0} + t_{B\to D2}\left(u_{2,0} + \frac{b\Delta T_0}{2}\right)$$

$$= \left[(t_{shol} + t_{plat}) + \frac{u_{2,0}t_{shol}}{b\Delta T_0} - t_{plat}\right] u_{2,0} + \left(\frac{2u_{2,0}t_{plat}}{b\Delta T_0} + 2t_{plat}\right)\left(u_{2,0} + \frac{b\Delta T_0}{2}\right)$$

$$= u_{2,0}t_{shol}\left(1 + \frac{u_{2,0}}{b\Delta T_0}\right) + \left(\frac{2u_{2,0}^2}{b\Delta T_0} + 3u_{2,0} + b\Delta T_0\right) t_{plat}. \quad (2.56)$$

The wave length of the final triangular profile l_1 is

$$\begin{aligned} l_1 &= (t_{plat} + 2t_{shol})u_{2,0} + (\frac{b\Delta T_0}{2})t_{B\to D} \\ &= (t_{plat} + 2t_{shol})u_{2,0} + \frac{b\Delta T_0}{2}\left(\frac{2u_{2,0}t_{plat}}{b\Delta T_0} + 2t_{plat}\right) \\ &= (2u_{2,0} + b\Delta T_0)t_{plat} + 2u_{2,0}t_{shol}. \end{aligned} \quad (2.57)$$

Next it is considered that the variation of the wave height after the formation of a triangular profile on the basis of the equal area rule [1]. The triangular wave profile ABC with a height of ΔT_0 and a length of l_1 is shown in Fig. 2.10. If each point of the wave profile moves with the speed given by Eq. (2.43), the wave ABC should becomes profile A'B'C' through propagation keeping its initial wave height. Since the profile A'B'C' violates the single value nature of a profile, the profile A'DE is obtained. As there is no energy dissipation, the area of the profiles ABC and A'DE must be equal. The discontinuity DE moves with the speed given by Eq. (2.47).

Angle θ is

$$\tan\theta = \frac{\Delta T_0}{[l_1 + (b\Delta T_0)\, t_{tria}]}, \quad (2.58)$$

where t_{tria} is the time after the formation of a triangular profile. Using angle θ, area of the $\triangle$ A'DE is given by

$$S_{A'DE} = \frac{1}{2}l^2 \tan\theta = \frac{1}{2}l^2 \cdot \frac{\Delta T_0}{[l_1 + (b\Delta T_0)\, t_{tria}]}, \quad (2.59)$$

where l is the length of the wave at time t_{tria} . According to the equal area rule $\triangle$ ABC $= \triangle$ A'DE

$$\frac{1}{2}l_1\Delta T_0 = \frac{1}{2}l^2 \frac{\Delta T_0}{[l_1 + (b\Delta T_0)\, t_{tria}]}. \quad (2.60)$$

Then the wave length l is

$$l = l_1 \left[1 + (b\Delta T_0)\, t_{tria}/l_1\right]^{1/2}. \tag{2.61}$$

$\triangle$ ABC = $\triangle$ A'DE can also be described in terms of ΔT . Since $\Delta T l = \Delta T_0 l_1$

$$\Delta T l_1 \left[1 + (b\Delta T_0)\, t_{tria}/l_1\right]^{1/2} = \Delta T_0 l_1,$$

$$\Delta T = \Delta T_0 \left[1 + (b\Delta T_0)\, t_{tria}/l_1\right]^{-1/2}. \tag{2.62}$$

To compare with the experimental results, t_{tria} is written in terms of propagating distance of a wave after the formation of a triangular profile Z_{tria} .

$$t_{tria} = \frac{Z_{at}}{u_{2,0} + b\Delta T_0/2}. \tag{2.63}$$

Substituting Eq. (2.63) into Eq.s (2.61) and (2.62) the wave height and the length at Z_{tria} are obtained by

$$l = l_1 \left[1 + \frac{(b\Delta T_0)\, Z_{tria}}{l_1 \left(u_{2,0} + b\Delta T_0/2\right)}\right]^{1/2}, \tag{2.64}$$

$$\Delta T = \Delta T_0 \left[1 + \frac{(b\Delta T_0)\, Z_{tria}}{l_1 \left(u_{2,0} + b\Delta T_0/2\right)}\right]^{-1/2}. \tag{2.65}$$

2.7 Dresner's analytical approach

Steady or quasi-steady heat transport phenomena in the superfluid breakdown state are analytically investigated by Dresner [25]. He investigated one-dimensional time variation of the temperature distribution near a planar heat source on the basis of the energy conservation law and the Gorter-Mellink relation when a pulsed heating is carried out. The Gorter-Mellink relation gives the equation which relates the heat flux and the temperature gradient for a fully developed superfluid turbulent flow in which the dense vortex

lines are generated.

$$q = -k(\nabla T)^{\frac{1}{3}}, \tag{2.66}$$

where

q : heat flux,

∇T : temperature gradient,

k : thermal conductance parameter.

The equation of energy conservation is written as

$$\nabla \cdot q + s\frac{\partial T}{\partial t} = 0, \tag{2.67}$$

where s is the volumetric heat capacity, t is the time after the onset of heating. Substituting Eq. (2.66) into Eq. (2.67), the governing equation of the heat transport in superfluid turbulent flow is obtained.

$$k\frac{\partial}{\partial z}\left(\frac{\partial T}{\partial z}\right)^{\frac{1}{3}} = s\frac{\partial T}{\partial t}, \tag{2.68}$$

where z is the distance from a heater. The boundary and initial conditions for the pulsed heating from a planar heat source are

$$\int_{-\infty}^{+\infty} s\,(T - T_B)\,dz = Q, \tag{2.69}$$

$$T\,(z, 0) = T_B, \tag{2.70}$$

$$T\,(\infty, t) = T_B, \tag{2.71}$$

where Q is the total amount of heat applied from a planar heat source. The particular solution of Eq. (2.68) being subject to the boundary conditions is

$$\frac{(kt/s)^{3/2}\,(T - T_B)}{(Q/s)^2} = \frac{4/3\sqrt{3}}{(x^4 + b^4)^{1/2}}, \tag{2.72}$$

$$x = z\,(Q/s)\,/\,(kt/s)^{-3/2},$$

$$b = 2\left[\Gamma\,(1/4)\right]^2/3\sqrt{3\pi} = 2.855.$$

According to Eq. (2.72) experimental data of time variation of the temperature distribution can be reduced to a single curve if the similarity parameters of

$$\Phi = \Delta T t^{3/2},$$

$$\Psi = z/t^{3/2},$$

where ΔT is the temperature variation from the equilibrium temperature. The curve in Fig. 2.11 shows an example of the solution of Eq. (2.68) for the conditions of $T_B = 1.70K$ and $Q = 40 \times 10^{-3} J/cm^2$. The curve is composed of two asymptotic lines. Substituting the similarity parameters of Φ and Ψ into Eq. (2.72), it becomes

$$\Phi = \frac{4/3\sqrt{3}k^{-3/2}s^{-1/2}Q^2}{\left(Q^4 s^2 k^{-6}\Psi^4 + b^4\right)^{1/2}} \quad . \tag{2.73}$$

If temperature is fixed, K, s and b are constant. Here, if Ψ becomes very large corresponding to the case t is small, i.e. just after the end of heating, an asymptotic solution to Eq. (2.73) can be written as

$$\Phi = \underbrace{4/3\sqrt{3}k^{3/2}s^{-3/2}}_{f(T)}\,\Psi^{-2}, \tag{2.74}$$

where $f(T)$ is a temperature dependent factor. Φ can be regarded as a function only of Ψ^{-2} and corresponds to the portion of the line which has an inclination of -2 in a double logarithmic plot. In the other extreme case of very small Ψ where t is large, i.e. long after the end of heating, Eq. (2.73) becomes asymptotically

$$\Phi = \underbrace{4/3\sqrt{3}\cdot b^{-2}k^{-3/2}s^{-1/2}}_{g(T)}\,Q^2, \tag{2.75}$$

where $g(T)$ is also another temperature dependent factor. In this case Φ is constant if the total amount of applied heat is given. It corresponds to the horizontal portion of a curve.

The comparison of this result with the experimental results and relating discussion will be given in Section 5.8.

Chapter 3

SUPERCONDUCTIVE TEMPERATURE SENSOR

3.1 Principle of a superconductive temperature sensor

A superconductive temperature sensor which has high temperature sensitivity and short response time is used to detect highly transient heat transport phenomena in He II. Fig. 3.1 shows the picture of the superconductive sensor. This sensor measures temperature variation by utilizing the abrupt change of resistivity of thin superconductive metal film due to superconducting transition. This type of sensor was originally developed by the group at Max-Planck-Institut [20]. Superconducting phenomena occurs in a number of materials such as metals and oxides when all the temperature, magnetic field and current density are below certain critical values. The electrical resistivity of the material vanishes, and Meissner effect appears in the superconductive state. If one of these three

quantities exceeds a critical value, superconductive transition from superconductive state to normal state occurs.

Superconductors can be classified into two types, type I superconductor and type II superconductor. Type I superconductor is pure metal, and type II superconductor is alloys and oxides. The former exhibits an almost discontinuous change from normal state resistivity to that of superconductive state, and vice versa. Fig. 3.2 shows the ideal resistivity variation of type I superconductor. The latter exhibits gradual superconductive transition (see Fig. 3.3). If one of the quantities exceeds a threshold value, the superconductive state breaks down and then resistivity gradually increases up to the normal Ohmic resistivity as the increase of the quantity. It is well known that pure tin is a type I superconductor. Its superconductive transition occurs near $3.7K$ within the temperature range of no more than $10^{-3}K$. It exhibits quite a sensitive resistivity change to temperature variation within the temperature range. Tin is utilized for a sensitive bolometer for the detection of infrared radiation. The temperature sensor for temperature measurement of highly transient thermo-fluid dynamic phenomena such as a thermal shock wave in He II would require the superconductive transition to occur within several hundreds mK at arbitrary temperatures below $T_\lambda = 2.17K$.

Superconductive transition of type II superconductor is adequate for the temperature measurement in He II. In the present study thin metal film consisting of gold and tin is used. Gold which does not become a superconductor acts as impurities for tin and depresses the superconductive transition of the film. The transition can be made more gradual at below T_λ.

3.2 Superconductive temperature sensor

Fig. 3.4 shows a schematic drawing of a superconductive temperature sensor. It quite resembles a conventional hot wire probe in shape to be used for the flow velocity measurement in aerodynamic experiments. The temperature variation is measured with a tiny sensing element on which surface a superconductive thin film is formed. It consists of gold and tin. Tin film with a thickness of 980Å is fabricated on 230Å of gold film by vacuum deposition on a side surface of quartz fiber with a length of $1.3mm$ and $40\mu m$ in diameter. The quartz fiber is glued with silver paste between metal needles. This shape can minimize disturbances to flow field to be measured. Since the heat capacity of the sensing element itself is quit small, the response time of the sensor is very short (not more than $10\mu s$). Fig. 3.5 shows a typical static voltage-current characteristic of the sensor taking the temperature as a parameter. The voltage drop across the sensing element is measured while gradually increasing the biased current I with keeping the temperature constant. The each curve goes horizontally from the origin until the bias current reaches a critical value which depends on the temperature. When the current reaches the critical value, the curve starts to rise. Generally the critical value becomes larger for the lower temperature. The current at which the variation of the voltage drop with the temperature increase is steepest is selected as the optimum bias current. Fig. 3.6 shows the typical variation of the voltage drop with the temperature taking the biased current as a parameter. The gradient of the curve give the sensitivity of the sensor. It can be seen that the higher biased current yields the higher sensitivity and also the region of high sensitivity shifts to lower temperature region.

3.3 Calibration of a superconductive temperature sensor

It is difficult to produce the superconductive temperature sensors which have the same characteristics. Every superconductive temperature sensor must be calibrated by a dynamical method at the beginning of experiment. Constant current is applied to a temperature sensor. The resistivity change due to temperature variation is measured as a voltage drop across a sensing element. The dynamical calibration is carried out by measuring a weak ($\leq 10W/cm^2$) and short ($\leq 100\mu s$) second sound heat pulse emitted from a planar heater with a calibrating temperature sensor fixed at a distance of $5mm$ from the heater. The theoretical temperature amplitude, ΔT_{theory} for applied heat flux q_p is given by the simple acoustic theory of second sound.

$$\Delta T_{theory} = q_p/\rho c_{20} C_P. \tag{3.1}$$

Since the relation holds only if any kinds of second sound wave attenuation is negligible, it is required to use a weak and short heat pulse and short distance of a temperature sensor from a heater. Detected voltage drop is compared with a theoretical temperature amplitude and then calibration coefficient ξ is obtained by the following equation.

$$\xi = \Delta V/\Delta T_{theory}, \tag{3.2}$$

where ΔV is the detected voltage drop across a sensing element.

The working range of a temperature sensor, which should be around the superconducting transition temperature, is roughly determined by the ratio of the thicknesses of gold and tin layers. It can be easily understood that higher ratio of tin layer results in

higher transition temperature. The optimum thicknesses of gold and tin layers for the present experiment determined from the numerous preliminary experiments are 230Å of gold and 980Å of tin. Fine trimming of the working temperature is made by adjusting the bias current to a temperature sensor. The bias current should practically be small enough to minimize the self heating from a sensing element which has finite electrical resistance. Typically the bias current is selected to be between 1 and $3mA$. The sensitivity is attained as large as $100\mu V/mK$. It is better by one order than that of a carbon resistance thermometer.

Chapter 4

EXPERIMENTAL SETUP

4.1 He II dewar and evacuation system

The picture of whole experimental setup is shown in Fig. 4.1. Fig. 4.2 shows the schematic illustration of the dewars, one is set inside of the other, and the evacuation system. The dewar is a cylindrical glass container having evacuated between the double walled space for thermal insulation. And also the inside wall is silvered to reduce radiation heat input from outside environment. Narrow unsilvered slit of $1cm$ in width is made on both side of wall from top to bottom for direct visual observation. He II is contained in the inner dewar. Liquid nitrogen inside of the outer dewar reduces the direct incident of thermal radiation from ambient temperature environment to He II. Experimental apparatus is hung by stainless tubes from the flange which is supported on the top of He II dewar.

He II bath temperature can be reduced by reducing the vapor pressure by pumping off along to the saturated vapor pressure curve. He II dewar is connected to a mechanical vacuum pump ($500l/min.$) via a control valve and a pressure regulating valve. The He

II bath pressure signal is transferred to the pressure regulating valve controller. The He II bath temperature is controlled by regulating the vapor pressure.

4.2 Main assembly and data acquisition system

Fig. 4.3 is the picture of the cryogenic flange inserted into the He II dewar. Fig. 4.4 is the picture of the main assembly of the experimental apparatus. Schematic drawing of main assembly of the experimental apparatus immersed in a He II bath is shown in Fig. 4.5. It consists of three main parts, a planar thin film heater, a cylindrical thermal shock tube and a superconducting temperature sensor. The planar heater, square Ni/Cr thin film, 27×27mm and 400Å in thickness, is formed on a Pyrex grass substrate by means of vacuum deposition. Copper electrode of 5000Å is also fabricated along both sides of the Ni/Cr film. Typical electrical resistance of the heater is 30Ω. The pulsed heating is done by means of Joule heating.

The cylindrical thermal shock tube which is made of Teflon is $150mm$ in length, $25mm$ in diameter and $35mm$ in outer diameter. The bottom portion of the tube in contact with the heater is shaped into a knife edge to minimize the heat capacity of the portion and to maintain tight seal with the heater surface. The tube maintains the one dimensional character of a thermal pulse. The superconductive temperature sensor is introduces from the upper end of the thermal shock tube. It is mounted on the movable temperature sensor mount so the distance from the heater to the sensor can be varied between 0.1 and $150mm$ with a $0.1mm$ step parallel to the shock tube axis.

Fig. 4.6 shows the block diagram of the whole experimental data acquisition system. Trapezoidal current pulse from a programmable arbitrary wave form generator is fed to

the heater via a high speed power amplifier, and pulsed heat flux is applied to He II. Rising time of the trapezoidal current pulse from zero to a constant value and falling time are fixed to be $6\mu s$. Total heating time , t_H, is varied arbitrary from $30\mu s$ to $4000\mu s$ depending on the purpose of measurement. The superconductive temperature sensor has two pairs of shielded lines which are also shielded by doubled stainless tubes. One is for a constant current supply and the other is connected to the low noise amplifier. The temperature variation due to the pulsed heating by the heater is detected with the temperature sensor and the signal is amplified by a factor of 100 with the low noise amplifier. All signals are transmitted to a personal computer via a digital oscilloscope to be stored on a floppy disk. Through the whole experimental runs, each successive measurement is carried out after a rest time of $120s$ to minimize the uncertainty in the effect of residual vortex lines generated by former heating. It is well known that residual vortex lines considerably affect the vortex development especially in the case of intense heating [18].

Chapter 5

RESULTS AND DISCUSSION

5.1 Three types of thermal shock wave

There are three types of thermal shock waves in He II according to the sign of the steeping coefficient defined by Eq. (2.40). These are a frontal shock wave, a back shock wave and a double shock wave as given in Fig. 5.1, 5.2 and 5.3, respectively, which are measured with a superconductive temperature sensor fixed at a distance of z from a planar thin film heater placed at the bottom of the shock tube. These waves are generated by a trapezoidal heat pulse of $t_H = 30\mu s$. The frontal shock wave in Fig. 5.1 is measured at temperature $T_B = 1.70K$. A temperature discontinuity is clearly observed at the front of a propagating wave profile. Back shock wave in Fig. 5.2 is observed at $T_B = 2.05K$. A discontinuity is formed at the back of a wave profile. Slight disturbance on the wave profile is just a electrical noise. Double shock wave in Fig. 5.3 is observed at $T_B = 1.86K$ which is slightly below the temperature at which the steeping coefficient vanishes. It is practically difficult to generate a pure double shock wave, because rather strong heat pulse is required for a wave profile extending both higher and lower temperatures than the temperature at

which the steeping coefficient vanishes and, furthermore, a long propagation distance is also required for a profile to form two temperature discontinuities due to weak nonlinearity in this temperature region as seen from Fig. 2.7. The large heat flux heating tends to generate high density quantized vortex lines to cause wave profile deformation due to the interaction with quantized vortices during propagation. The wave profile given in Fig. 5.3 may be the best example for the double shock wave.

These results demonstrate that the superconductive temperature sensor possesses a sufficient temperature sensitivity and a short response time to measure the temperature variation associated with a thermal shock wave.

Multiple thermal shock wave profiles generated by trapezoidal heat pulses of a number of values of the heat flux are shown in Fig. 5.4, where all the profiles are superposed by synchronizing at the wave front. Bath temperature T_B is $1.69K$ in order to produce the frontal shock waves and the heating time t_H is selected to be $100\mu s$. Heat flux q_p is varied from 20 to $40W/cm^2$. The superconductive temperature sensor is fixed at a distance z of $5mm$ from the heater. When the applied heat flux is small, the measured wave profile is almost trapezoidal except the wave front steepening due to the hydrodynamic nonlinear effect. The measured shock wave height is found to be in proportion to the applied heat flux and to agree with the theoretical value obtained by Eq. (3.1) as long as the heat flux is sufficiently small. As the applied heat flux increases, additional wave deformation owing to the interaction with quantized vortices generated near a heater becomes to be apparent. And the wave height loses the linear dependence on heat flux. The slight temperature rises following the main wave profiles are also observed as heat flux increases. These come from the dissipative effect.

Similar result for back shocks measured at $T_B = 1.90K$ is shown in Fig. 5.5. The result obtained at $T_B = 2.10K$ is also shown in Fig. 5.6. The results are qualitatively the same as Fig. 5.4 but the wave deformation due to the interaction with quantized vortex lines becomes more noticeable than that at lower heat flux.

5.2 Measurement of characteristic time of quantized vortex development

The characteristic time of quantized vortex development is measured as a function of applied heat flux and temperature by analyzing the thermal shock wave deformation data. Quantized vortex lines are generated when the relative velocity v_{ns} exceeds a critical value. The vortex lines need finite development time in order to reach very high density enough to cause significant wave form deformation. If the quantized vortex line density is not sufficiently high to cause an appreciable wave form deformation, a thermal shock wave profile changes only as a result of hydrodynamic nonlinear effect, that is to say the plateau portion of a trapezoidal thermal pulse does not decline. On the other hand, if the density of quantized vortex becomes high enough to cause strong interaction, a thermal pulse is deformed through the thermal boundary layer and thus a partial declination in the plateau portion is observed as illustrated in Fig. 5.7. The time duration t_{ve} in the figure from the wave front to the point at which the wave height begins to reduce is defined as the characteristic time. The decision of t_{ve} is rather a difficult procedure in the case of small heat flux as the wave height only gradually reduces due to the gradual development of quantized vortex lines. The noise superposed on measured wave profiles also makes it

difficult. Therefore the end point of t_{ve} is defined as the point at which the reduction of wave height exceeds 3σ of the data fluctuation in the plateau portion.

Measured wave profiles at $T_B = 1.70K$ and $z = 10mm$ are shown in Fig. 5.8. The heating time is fixed at $t_H = 1000\mu s$. The heat flux q_p is varied from 5 to $26W/cm^2$. It can be observed from this figure that the point where the reduction becomes noticeable gets to close to the wave front as heat flux increases. It is interesting to note that the wave form for $q_p = 26W/cm^2$ becomes even considerably shorter than t_H and is accompanied with "thermal tail " that is a slightly high temperature region than the equilibrium temperature. This interesting feature is discussed in detail later. Another example of wave profiles measured at different temperature, $T_B = 1.90K$ is shown in Fig. 5.9. The wave deformation seems to occur for smaller heat flux than the former case of $T_B = 1.70K$.

Fig. 5.10 shows the result of t_{ve} as a function of applied heat flux q_p for two different temperatures, and Fig. 5.11 is their double logarithmic plot. Experimental data obtained at $1.70K$ are represented by closed diamonds and the data at $1.90K$ by open circles in the figures. The data points are obtained two independent experimental runs for both cases. Solid and broken lines are the linear regression results, of which inclinations are -2.2 at $1.70K$ and -2.0 at $1.90K$. It may be concluded from the data that t_{ve} is inversely proportional to q_p^2.

Further measurement results measured at temperatures between $1.60K$ and $2.03K$ are shown in the same double logarithmic plot together with corresponding linear regression results in Fig. 5.12. It should be mentioned that the data obtained at lower temperatures appear in the upper region in the Fig. 5.12. As the temperature rises, the data shift towards the lower region. It means that the development of quantized vor-

tices becomes faster as the temperature rises. From many experimental results for the heat flux ranging from 5 to $40W/cm^2$, it is found that the relation between t_{ve} and q_p is approximately given by

$$t_{ve} = c'(T_B)q_p^{-2}, \tag{5.1}$$

and it can be written in the other form

$$q_p t_{ve}^{\frac{1}{2}} = c(T_B), \tag{5.2}$$

where $c'(T_B)$ and $c(T_B)$ are temperature dependent coefficients given experimentally. Fig. 5.13 shows the variation of $c(T_B)$ with the temperature. It decreases monotonically with the rise of temperature. It seems that this result is quit important because it is obtained at the heat flux range, intermediate to large values, which had not been obtained in previous experiments. In the report by Vinen [3] [4][5]the relation between t_{ve} and q_p is given by Eq. (2.7) for very small heat fluxes ($q_p \leq 0.4W/cm^2$), which has a different functional form from Eq. (5.1).

The discrepancy between the result of the Vinen vortex line density equation and experimental result for the case of large heat flux with respect to the characteristic time for vortex development has been pointed out in a couple of numerical simulations of thermal shock wave propagation [21]. It is reported that the vortex line density equation needs a finite initial condition L_0 which defines the initial vortex line density in undisturbed He II in order to reproduce the measured thermal shock wave deformation owing to the interaction with quantized vortices. The introduction of initial vortex line density L_0 is quite popular in numerical simulation of propagating thermal shock wave but the physical meaning of L_0 is not clear. For instance, the value of L_0 which gives sufficient numerical result is apparently too large for the value of the undisturbed He II considering the final

value of the vortex line density. The typical final equilibrium value of the vortex line density is $10^7 cm/cm^3$ while L_0 needs to be as high as $10^6 cm/cm^3$. If L_0 is set to be zero, γ of the source term in Eq. (2.8) needs to be several thousands times larger than that obtained by Vinen [22]. Present experimental results imply that the Vinen vortex line density equation needs appropriate modification in the case of the large heat flux heating.

5.3 Wave form variation through propagation

Wave form variation during propagation is measured with a superconductive temperature sensor by changing the distance between a temperature sensor and a heater. The results are shown in Fig.s 5.14 and 5.15. Each wave profile is measured with a temperature sensor fixed at a distance z as indicated beneath each profile and is drawn at the corresponding location which is calculated by supposing that the full scale of the abscissa corresponds to $z = 100mm$ in each figure. Fig. 5.14 shows the result under the conditions of $T_B = 1.69K$, $q_p = 9W/cm^2$ and $t_H = 30\mu s$. Since the heat flux is relatively small and the heating time is short, each profile is free from the influence of quantized vortices. A trapezoidal wave form is observed in the vicinity of a heater ($z = 1.5mm$), and is deformed only due to the hydrodynamic nonlinear effect during propagation. The trapezoidal profile first steepens at the wave front to result in the formation of a temperature discontinuity. The plateau portion diminishes through further propagation and finally the wave form becomes triangular. The triangular profile further changes according to the Burgers equation which is approximated by the equal area rule. Fig. 5.15 shows the result for the higher heat flux of $q_p = 40W/cm^2$ at the same temperature as the last example. The profile changes more quickly than in Fig. 5.14. It is caused not only by

the stronger nonlinear effect because of the higher temperature amplitude but also by the interaction with quantized vortices. The wave height even in the very vicinity of the heater becomes lower than the theoretical value due to the effect of the interaction with quantized vortices. Fig.s 5.16 and 5.17 show the results of propagating back shock waves. The trapezoidal profile forms temperature discontinuity at the back of wave profile and is deformed into a triangular profile through propagation.

Fig. 5.18 shows the wave height variation during propagation. Ordinate represents the normalized wave height by the theoretical value at $z = 0$ given by Eq. (3.1). Abscissa is the distance from a temperature sensor to a heater at $z = 0$. Several experimental data are plotted by taking the applied heat flux as a parameter. Solid lines represent the theoretical wave height variation given by Eq.s (2.56) and (2.65) on the basis of the equal area rule. The location of the formation of a triangular profile seems to slightly deviate for small heat flux cases. But generally the experimental data agree well with the theoretical value. The double logarithmic plot of Fig. 5.18 is shown in Fig. 5.19. The agreement of the experimental data with the theoretical result becomes more clearer. The variation of wave height after the formation of a triangular profile obeys a square root relation to z in the region. The similar result of a back shock wave is shown in Fig.s 5.20 and 5.21. In the case of an intense heating such as $q_p = 40W/cm^2$ the wave height is decreased even in the very vicinity of a heater by the strong interaction with high density quantized vortices in the region but it varies approximately with theoretical prediction in the later stage of propagation.

It is found that the experimental data of the variation of a thermal shock wave height during propagation fairly well agree with the theoretical prediction by the equal area rule

in the both cases of a frontal and back shock waves. However, strictly speaking, there are slight systematical discrepancies between the experimental data and the theoretical prediction. The experimental data of frontal shock waves tend to deviate slightly downward from the prediction in particular for small q_p. On the contrary, those of back shock waves deviate upward. The deviation may be caused by the self-focusing of a thermal shock wave owing to nonuniform heating. There is a possibility of the occurrence of nonuniform heating in a local region along the contact line of the heater and the bottom end of the cylindrical shock tube side wall.

In addition, the experimental data are compared with the result obtained by solving the two-fluid equation system numerically [27]. Fig. 5.22 shows the comparison among the experimental data, the numerical result and the analytical solution on the basis of the equal area rule in the case of relatively small q_p where the effect of quantized vortex lines is small. They well agree with each other. It can be also concluded that the equal area rule well approximates the solution of the two-fluid equation.

The variation of the wave length during propagation is plotted in Fig. 5.23. It seems that the plot is more convenient to understand the wave deformation. The variation of the wave length can be divided into three stages. It does not change before the formation of a temperature discontinuity. This is the first stage. The wave length starts to change just after the formation of a temperature discontinuity prior to the completion of a triangular wave form where the wave height starts to change. The variation of the wave length is linear to the propagation distance since the height of the wave does not change in this stage. In the final stage the triangular profile changes its height and length with conserving energy as given by Eq.s (2.65) and (2.64). The each solid lines which

represents the theoretical prediction in the figure consists of three curves. For instance, the end point of the first stage z_1 and second stage z_2 are $z_1 = 12.7mm$ and $z_2 = 76.5mm$ for $q_p = 3.2W/cm^2$ and $z_1 = 4.6mm$ and $z_2 = 27.9mm$ for $q_p = 9.0W/cm^2$, respectively.

The variation of the amount of heat transported in the form of a thermal shock wave is investigated. The amount of heat passing through unit area is calculated by integrating the measured wave profile. This quantity is nothing but the area of a wave profile in a $\Delta T - t$ diagram. It is defined by the following equation.

$$E_w = c_{20}\rho C_P \int_0^{t_w} \Delta T(t)dt \quad , \tag{5.3}$$

where t_w is the twice half value width of the measured wave profile in time. The definition is schematically illustrated in Fig. 5.24. The integration is carried out from the wave front to the point corresponding to $t = t_w$. The initial heat pulse from is schematically shown in Fig. 5.25 and the total amount of heat fed from a hater is given by

$$E_{w,0} = q_p(t_1 + 2t_2 + t_3)/2, \tag{5.4}$$

where t_1 is the rising time, t_2 is the time duration of the constant current portion and t_3 is the falling time. It is clear that the heating time t_H is equal to $t_1 + t_2 + t_3$. The results are plotted in Fig. 5.26. It is found that the whole applied heat is transported by a thermal shock wave when the heat flux is not so large (in the cases of $q_p = 3.2$ and $9.0W/cm^2$). The amount of heat almost does not change during propagation. In the case of the large heat flux heating, $q_p = 40W/cm^2$ since the wave height is suppressed due to the interaction with quantized vortex lines in the very vicinity of a heater only part of input heat is transported by a thermal shock wave. However, out of this region it is hard to observe the dissipative effect due to the interaction with quantized vortex lines.

It means that the effect of the self-induced vortices is substantially negligible under the present heating condition.

5.4 Wave deformation and limiting profile

Fig. 5.27 shows the superposed wave profiles generated under various initial heating conditions of q_p and t_H. The applied heat flux from a heater is varied from 5 to $40 W/cm^2$ and the heating time is selected to be $500\mu s$ and $1000\mu s$. This figure shows the wave deformation due to the interaction with quantized vortices. As long as the heat flux is below a critical value and heating time is short, the wave form is free from the influence of the interaction with quantized vortices(see wave forms 1 and 2). The wave height is exactly equal to the value given by the simple acoustic theory and the length of it is just same as t_H. Wave form changes only because the hydrodynamic nonlinearity for small q_p. The deformation of a wave form becomes noticeable when the heat flux or the heating time becomes sufficiently large or long. In the case of wave form 3, heating time is rather long, $1000\mu s$, though the heat flux is not so large. It is seen that the wave height at the wave front is nearly equal to the theoretical value given by Eq. (3.1), but gradually diminishes towards the trailing edge, and that the length becomes longer than the initial heat pulse, and moreover a diffusive tail is formed almost continuously following the main body of a propagating thermal pulse. Wave form 4 shows the wave deformation in the case of higher heat flux and shorter heating time than in the case of wave form 3. The wave height diminishes more rapidly than that of wave form 3.

Further increase in the heat flux leads to quite an interesting feature, the formation of limiting profile. Intense pulsed heating makes quantized vortex lines develop to very

high density in quite a short time. As a result of the rapid development of quantized vortices, a thermal wave form is subjected to the strong interaction with vortices even from the wave front and then it becomes considerably shorter than t_H as shown by the wave forms of 5 and 6. Moreover, these two wave forms found to be almost coincide with each other in spite of the big difference in the heating time. This kind of tendency is also reported in another experiment [17]. The unique wave form is named the limiting profile. The wave shape is determined only in the initial stage of heating and is not affected by subsequent heating and so the wave form becomes insensitive to the difference in heating time. Typical limiting profiles measured at $T_B = 1.70K$ of a frontal shock temperature region and $1.90K$ of a back shock are shown in Fig. 5.28 where both onset times of heating are synchronized. It is seen the propagation speed of a frontal shock wave is faster than that of a back shock wave. It can be also seen that the difference in the locations of temperature discontinuities which are formed at the wave front at $T_B = 1.70K$ and at back of the profile at $T_B = 1.90K$. The general features of a limiting profile can be summarized as follows almost independently of the temperature; the profile is formed for $q_p > 30W/cm^2$, it is almost independent of the heating time longer than approximately $200\mu s$, the profiles is almost triangular and the half value width is approximately $100\mu s$.

In the case of an intense heating a thermal boundary layer is formed in the vicinity of a heater due to accumulation of dense quantized vortices. In the boundary layer heat is not transported by the efficient pure thermal counterflow mechanism within a second sound thermal pulse.

5.5 Highly transient heat transport in a second sound wave mode

The amount of heat transported by a second sound wave is investigated under the various heating conditions. The result obtained at $T_B = 1.70K$ is shown as a function of applied heat flux q_p in Fig. 5.29. Ordinate and abscissa represent E_w and q_p, respectively. Two experimental data for $t_H = 500\mu s$ and $1000\mu s$ are plotted. The solid lines in Fig. 5.29 represent the total amount of initial heat fed from a heater. Experimental data coincide with the solid lines when the heat flux is small. It means applied heat is wholly transported by the second sound wave mode as long as the superfluid breakdown does not occur in this situation. As the applied heat flux increases, superfluid break down occurs. The wave profile is deformed through the interaction with quantized vortices. The amount of heat transported by the second sound wave mode deviates downwards from the solid lines. It can be seen that the deviation occurs at lower heat flux for the longer heating time. With a further increase in the heat flux, the amount of heat reaches maximum value and then gets to decrease. The drastic decrease of the amount of heat in spite of still increasing heat flux is caused by the onset of boiling on a heater surface.

It is found that in the very large heat flux region, the amount of heat loses the dependence on the heating time, and so the experimental data of different heating time almost coincide with each other. In this case the wave profiles turn into the limiting profile. The wave form becomes considerably shorter than that of the applied heat pulse, so only limited amount of heat is transported by the second sound wave mode. The experimental data obtained at different temperature of $1.95K$ is shown in Fig. 5.30 where

the experimental data for three different heating times (200, 500 and $1000\mu s$) are plotted. Qualitatively the same results are obtained except that the data for $t_H = 200\mu s$ deviate upward from those of other longer heating times at the very large heat flux region. Since the heating time of $200\mu s$ is almost the same as the length of a limiting profile, it is not sufficiently long to form a full limiting profile.

The temperature dependence of the amount of heat transported in the second sound wave mode is shown in Fig. 5.31. Temperature is varied from 1.60 to $2.05K$ and heating time is fixed at $1000\mu s$. Solid line represents the total amount of input heat from a heater. Fig. 5.32 shows the similar result but heating time is selected to be $500\mu s$. The amount of heat shows the clear temperature dependence. It is seen that the heat flux at which the amount start to deviate from the solid line becomes lower as the temperature rises. It is also found that the amount of heat strongly depending on the temperature arises within the heat flux range approximately between 10 to $30W/cm^2$. This dependency becomes more prominent at temperatures above $1.95K$. The temperature dependence may be resulted from the dependence of the rate of development of quantized vortex on the temperature. This kind of tendency is also observed in the experiments of the visualization investigation of the onset of boiling [26]. The onset of boiling becomes abruptly fast if the temperature rises above $T_B = 2.0K$ in that experiment.

5.6 Formation of a thermal boundary layer

The heat which is not transported in the second sound wave mode accumulates in the vicinity of a heater, that is the thermal boundary layer, and raises the temperature in the layer. Afterward heat is transported through the layer by the restricted thermal

counterflow which is the thermal counterflow affected by the dense quantized vortices. Because of the mutual friction force due to the interaction between dense quantized vortices and the normal fluid component, the relative velocity in the counterflow can not be larger than a critical value. The temperature rise as a result of the formation of a thermal boundary layer can be recognized as the secondary temperature rise following the thermal shock wave profile. Fig. 5.33 shows the superposed transient temperature traces measured at different locations of a temperature sensor. The distance from a heater to a sensor is varied between 0.5 to $30mm$ as indicated in this figure. Ordinate represents the temperature rise and the abscissa is the time. The point corresponding to the onset of heating is marked by " Heater ON" on the abscissa. Each of the traces consists of the propagating thermal shock wave as an initial spiky triangular profile and the secondary gradual temperature rise which indicates the thermal boundary layer reaches the sensor location. The peak of secondary temperature rise moves away from a heater at a speed of the order of $1m/s$. It is much slower than the propagation speed of the second sound wave, of the order of $20m/s$. The temperature rise continues over $20ms$. It implies that the decay of quantized vortices is quite slow as compared with the time of its development. Moreover the third temperature rise is also detected at approximately $18ms$ after the onset of heating with the temperature sensor fixed at a distance of $0.5mm$ from a heater in Fig. 5.33. This is the signal of the onset of boiling on the heater. At the first glance, it is a little strange that boiling signal is detected at $17ms$ after the end of pulsed heating. But it can be understood in the following way. The onset time of boiling must be earlier than $18ms$, in fact, $18ms$ is just a time which is needed to develop the vapor film reaching the location of the temperature sensor, $0.5mm$. The vapor layer development is

a rather slow process.

The visualization study of the onset of boiling by Schulieren method and shadowgraph [26] gives the onset time of boiling in the case of a vertical transparent planer heater. The typical result is shown in Fig. 5.34. According to the result of this study, spotwise transient nucleate boiling first appears at several tens μs after the onset of heating, and the onset of film boiling is observed after several ms under the similar heating condition of present heating. The appearance of the third temperature rise is not reproducible, though the thermal shock wave and the secondary temperature rise are reproducible. It is understood that boiling is a rather random phenomena in both time and space. The signal of the third temperature rise can be detected up to $z = 10mm$ in the present heating condition. Fig.s 5.35 and 5.36 are the results obtained for different heat fluxes of $26W/cm^2$ and $15W/cm^2$, respectively. It is clearly seen that the development of the secondary temperature rise becomes small and is not detected far from a heater. In the case of $q_p = 15W/cm^2$ shown in Fig. 5.36 the clear secondary temperature rise is only observed at $z = 1mm$ and $2mm$.

The time variation of the temperature distribution near a heater including a thermal boundary layer reconstructed from the data presented in Fig.s 5.33 , 5.35 and 5.36 are shown in Fig.s 5.37, 5.38 and 5.39, respectively. The ordinate and abscissa represent the temperature rise from an equilibrium temperature and the distance from a heater. The time after the onset of heating t_D is taken as a parameter. The temperature distributions are plotted up to $t_D = 8ms$ every $1ms$ after the end of heating. The temperature $T_B = 1.70K$ and the heating time $t_H = 1000\mu s$ are fixed but the heat flux is varied among those figures. The result obtained for $q_p = 40W/cm^2$ is shown in Fig. 5.37. The thermal

boundary layer with a large temperature gradient is clearly observed in the vicinity of a heater for several ms after the onset of heating ($t_D = 2 - 5ms$). The thermal boundary layer is formed because of the accumulation of dense quantized vortices generated by the large heat flux heating. It should be noted that the thermal shock wave has already reached at a distance of 40 to $80mm$ from a heater in those times so it is not seen in this figure. The thickness of the thermal boundary layer can be defined as $6mm$. The result for $q_p = 20W/cm^2$ in Fig. 5.38 also shows the formation of a thermal boundary layer but its temperature and thickness are lower and thinner than those given in Fig. 5.37. The thermal boundary layer gradually diminishes its peak temperature and, at the same time, expands outward from a heater with the laps of time. The time variation of the temperature distribution in the thermal boundary layer resembles that caused by usual diffusion process. It is found from the experimental fact that the heat transport process in the thermal boundary layer in which the restricted thermal counterflow is a governing heat transport process resembles the usual diffusion process. The result of rather small heat flux of $q_p = 15W/cm^2$ shown in Fig. 5.39 exhibits a different time variation of the temperature distribution. The range of the ordinate is reduced appropriately. Because the applied heat flux is not sufficiently large to generate dense quantized vortices, major part of the input heat is transported in the second sound wave mode and an only thin thermal boundary layer is formed in a quite short period just after the end of a heating. Experimental data up to $t_D = 3ms$ are plotted in this figure. It is clearly seen that the shape of the traveling thermal shock wave does not become a limiting profile and major part of input heat is transported in the form of a wave. This tendency is suggested by the transient temperature traces in Fig. 5.36.

The result at for different temperature of $T_B = 1.90K$ is also shown in Fig. 5.40. The temperature variation is qualitatively the same as that of $T_B = 1.70K$ but quantitatively is not quite same in both the maximum temperature and thickness. The peak temperature becomes lower and the thickness of the layer gets to be thinner. It may be because the temperature dependence of the heat capacity, quantized vortex lines development rate and the decay rate.

Finally it should be noted that the temperature slightly drops in the very vicinity of a heater in the later phase. The reason of the temperature drop is still an open question but it may strongly relates to the drift and decay of the quantized vortex tangle at a heater toward outward from a heater.

5.7 Highly transient heat transport through a thermal boundary layer

It is seen from the discussions in the former sections that there are three heat transport processes involved in highly transient heat transport in He II in the case of large heat flux heating. The first is the second sound wave mode which is the predominant process when applied heat flux is not large enough to generate dense quantized vortices. The second one is the heat transport by the restricted thermal counterflow under the influence of high density quantized vortices which is the governing heat transport process through a thermal boundary layer. The third one is boiling on a heater. The heat consumed in boiling process is further transported outward by the restricted thermal counterflow in the later stage. It is, however, more appropriate to regard the heat is stored in the vapor

layer formed in the vicinity of a heater in the consideration in the present time scale. The amount of heat transported by the restricted thermal counterflow is calculated from the experimental result of the time variation of a temperature distribution in the vicinity of a heater. The amount of heat consumed for the boiling is defined as the heat which does not transported by the other two processes.

The contribution of those processes are shown in Fig. 5.41, where the filled symbols indicate the boundary between the second sound wave mode and the restricted thermal counterflow, and the open symbols indicate that between the restricted thermal counterflow and the evaporation. These results are obtained under the condition $T_B = 1.70K$ and $t_H = 1000\mu s$. If the heat flux is less than $5W/cm^2$, the entire heat is transported in the second sound wave mode. When the heat flux increases beyond $5W/cm^2$, superfluid breakdown occurs and some portion of heat generated by a heater accumulates in a thermal boundary layer and then is transported outward from a heater region by the restricted thermal counterflow. Above $15W/cm^2$, the onset of boiling is observed on a heater surface and input heat begins to be consumed in evaporation. The contribution of the second sound wave mode decreases and those of the restricted thermal counterflow and evaporation increase as the heat flux increases. In this figure a set of the experimental result obtained at $T_B = 1.90K$ and $q_p = 40W/cm^2$ is also plotted for comparison. At the higher temperature, the superfluid breakdown occurs at lower heat flux and the contribution of the restricted thermal counterflow and evaporation becomes more significant even at lower heat flux than at lower temperatures, that is the boundaries between the three contributions as given in Fig. 5.41 shift leftwards. Fig. 5.42 shows the similar result, where the ordinate is absolute amount of heat transported by those processes. Here

most of the data are those obtained at $T_B = 1.70K$, $t_H = 1000\mu s$, but some data for $t_H = 2000\mu s$ are added for reference, which are denoted by squares. The total amount of heat applied from unit area of a heater is represented by broken lines for two cases of heating times. It is seen that the contribution of the second sound wave mode decreases abruptly above $q_p = 15W/cm^2$. On the other hand the contributions of the restricted counterflow and evaporation increase with the increase of the heat flux. It can be also seen that the amount of heat transported by the second sound wave mode in the case of $t_H = 2000\mu s$, $q_p = 20W/cm^2$ is almost the same as that in the case of $t_H = 1000\mu s$, $q_p = 20W/cm^2$ because the wave form is reduced to a limiting profile losing their dependence on the heating time for large heat flux.

The ratio of the amounts of heat transported by those three processes to the total input heat are plotted for different heating times of $t_H = 1$, 2 and $4ms$ in Fig. 5.43. It is seen that the two boundaries dividing three processes vary with the heating time. However, it is found that the dependence of the boundaries on t_H can be almost eliminated if a variable

$$q_p t_H^{1/2}$$

is taken as the abscissa as shown in Fig. 5.44. Several curves are found to reduce to almost universal two boundaries irrespectively of the heating time. It is seen from the figure that the second sound wave mode is only mechanism of the highly transient heat transport when $q_p t_H^{1/2} \leq 0.2$. When $q_p t_H^{1/2}$ exceeds 0.2, the contribution of the restricted thermal counterflow arises. If $q_p t_H^{1/2}$ become larger than 0.5, boiling in the thermal boundary layer on a heater occurs and the contributions of the restricted thermal counterflow and evaporation become more significant with the increase of $q_p t_H^{1/2}$. In this figure a broken

and a dotted broken lines are drawn to indicated specific values of $q_p t_H^{1/2}$. The dotted broken line indicates the value of $q_p t_H^{1/2} = 0.23$ at which quantized vortex lines appear to induce the superfluid breakdown as discussed in Section 5.2. According to the Fig. 5.13, $c(T_B) = 0.23$ gives the characteristic time of quantized vortices development at $T_B = 1.70K$. The value of $q_p t_H^{1/2}$ indicated by this dotted broken line well coincide with the value at which the contribution of the restricted thermal counterflow arises. A broken line represents the criterion of onset of boiling obtained empirically by Tsoi and Lutset [23] The value is also consistent with the value at which the contribution of the evaporation arises.

5.8 Comparison of experimental results with an analytical solution by Dresner

Applied heat is transported by such three processes as the second sound wave mode, the restricted thermal counterflow and consumption for evaporation. It is seen that the thermal behavior in the restricted thermal counterflow region including the thermal boundary layer resembles that in the usual diffusion process. The experimental data are compared with the analytical result Eq. (2.72) introduced by Dresner in Fig. 5.45. The broken line shows the analytical solution obtained in terms of the total heat input Q. It does not agree with the experimental data. The consequence indicates that the accurate estimation of Q is essential to make a comparison between them as Dresner's formulation does not consider the contributions of second sound wave mode heat transport and evaporation. To make a fair comparison, the only contribution of the restricted thermal

counterflow needs to be extracted from total heat transport. According to the Fig. 5.44 the amount of heat transported by restricted thermal counterflow mechanism is 22% of the total amount. The solid line represents the analytical solution obtained by substituting 22% of the input heat for Q in Eq. (2.72). The curve shows a fair agreement with the experimental data. Fig. 5.46 shows the similar result in the case of $q_p = 20W/cm^2$. The amount of heat transported by the restricted thermal counterflow is 27% of the total heat amount. The broken line goes far above the experimental data but the solid line agrees with the experimental data.

5.9 A series of highly transient therm-fluid dynamic phenomena after a pulsed heating

The results obtained by the high resolution temperature measurement of the highly transient thermo-fluid dynamic phenomena in He II contribute to the total understanding of a series of transient thermo-fluid dynamic phenomena. Combining the results obtained in the present study with the other two studies such as the visualization study of the transient thermo-fluid dynamic phenomena in He II with a laser photography interferometer by Iida et al. [28] and the visualization study of transient boiling phenomena in He II by Katsuki et al. [26]. in our laboratory, the general view of a series of transient thermo-fluid dynamic phenomena in He II are obtained and is schematically drawn in Fig. 5.47. The ordinate represents the magnitude of the physical quantity of the each phenomenon. It represents the propagation distance for the first and second waves. It represents the vortex line density and the thickness of the thermal boundary layer for

the quantized vortex line development and the formation of a thermal boundary layer, respectively. For boiling the ordinate represents the radius of the vapor bubble and the thickness of the vapor layer. The abscissa represents the logarithmic time t after the onset of the intense pulsed heating. In the case of the intense heating, the following a series of transient thermo-fluid dynamic phenomena are occur. The first sound and the second sound waves are generated just after the onset of the heating. Since only part of heat is transported by the second sound wave, dense quantized vortices are generated in the vicinity of a heater. The thermal boundary layer is formed due to the accumulation of quantized vortices and the transient nucleate boiling is also observed just after the beginning of the formation of the thermal boundary layer. In the later stage, the film boiling is observed. Depending on the temperature and the hydrostatic pressure, audible noise can be heard that is called noisy boiling. Those physical quantities are functions of the heat flux and temperature. Generally, if the heat flux becomes large those quantities increase more rapidly.

Chapter 6

CONCLUSION

Experimental investigation of highly transient thermo-fluid dynamic phenomena in He II is carried out with a superconductive temperature sensor. The following conclusions are obtained through the present investigation.

1. The characteristic time of quantized vortex development t_{ve} in the case of strong heating is obtained by analyzing the deformation of the measured thermal pulse profile. The result is expressed in terms of q_p and a temperature dependent coefficient $c(T_B)$ by the equation,

$$q_p t_{ve}^{\frac{1}{2}} = c(T_B).$$

   This relation is different from the empirical result for very small heat fluxes obtained by Vinen. This new experimental fact may partly question the validity of the Vinen vortex line density equation in the case of strong heating.

2. The variation of the second sound wave height due to the hydrodynamic nonlinearity is found to well agree with the prediction by the equal area rule. The variation of wave length is found to be more susceptible to the nonlinear hydrodynamic feature

than the variation of wave height.

3. Heat applied from a heater is wholly transported in the second sound wave mode when applied heat flux is sufficiently small.

4. In the case of strong heating a second sound wave is deformed by the interaction with quantized vortices. When the heat flux becomes considerably large, a thermal pulse is reduced to a unique very short triangular profile called the limiting profile irrespectively of the heating time, which appears when $q_p > 30W/cm^2$ and $t_H > 200\mu s$. Its half value width is approximately $50 \sim 100\mu s$.

5. A thermal boundary layer is formed due to the accumulation of dense quantized vortices in the vicinity of a heater for large heat flux. The thickness of the layer is found to be $5 \sim 10mm$. The decay of the layer is very slow ($\gg$ several tenth ms) compared with its quick formation, which may imply that the decay of quantized vortices is very slow.

6. The transient heat transport through a thermal boundary layer is found to be governed by the restricted thermal counterflow mechanism by dense quantized vortices which apparently resembles the ordinary thermal diffusion process. Thus boiling may be observed in the thermal boundary layer.

7. The contribution of the second sound wave mode to the transient heat transport decreases as the increase of the heat flux, and the contributions of the other two processes, the restricted thermal counterflow and boiling replace it.

8. The relative contributions of the three heat transport processes are found to be uniquely treated if the parameter $q_p t_H^{\frac{1}{2}}$ is introduced.

9. It is found that Dresner's analytical approach can only be applied in highly transient case for the restricted thermal counterflow portion only if the amount of heat transported by the restricted thermal counterflow is evaluated quantitatively.

Appendix A

Propagation speed of sound in He II

Coefficient of the four homogeneous equations (2.15)-(2.18) in Section 2.4 can be rewritten in the following form.

$$[\mathrm{A}] = \begin{bmatrix} -i\omega\frac{\partial\rho}{\partial P} & -i\omega\frac{\partial\rho}{\partial T} & ik_0\rho_{n,0} & ik_0\rho_{s,0} \\ -i\omega\frac{\partial\rho s}{\partial P} & -i\omega\frac{\partial\rho s}{\partial T} & ik_0\rho_0 s_0 & 0 \\ i\frac{k_0}{\rho_0} & -ik_0 s_0 & 0 & -i\omega \\ ik_0 & 0 & -i\omega\rho_{n,0} & -i\omega\rho_{s,0} \end{bmatrix}. \tag{A.1}$$

Determinant of $[A]$ must vanish in order for there to exist a non-trivial solution of the four homogeneous equations and is calculated as follows,

$$|A| = \left(-i\omega\frac{\partial\rho s}{\partial P}\right)(-1)^{2+1} \begin{vmatrix} -i\omega\frac{\partial\rho}{\partial T} & ik_0\rho_{n,0} & ik_0\rho_{s,0} \\ -ik_0 s_0 & 0 & -i\omega \\ 0 & -i\omega\rho_{n,0} & -i\omega\rho_{s,0} \end{vmatrix}$$

$$
\begin{aligned}
&+\left(-i\omega\frac{\partial\rho s}{\partial T}\right)(-1)^{2+2}\begin{vmatrix} -i\omega\frac{\partial\rho}{\partial P} & ik_0\rho_{n,0} & ik_0\rho_{s,0} \\ i\frac{k_0}{\rho_0} & 0 & -i\omega \\ ik_0 & -i\omega\rho_{n,0} & -i\omega\rho_{s,0}\end{vmatrix} \\
&+(k_0\rho_0 s_0)(-1)^{2+3}\begin{vmatrix} -i\omega\frac{\partial\rho}{\partial P} & -i\omega\frac{\partial\rho}{\partial T} & ik_0\rho_{s,0} \\ i\frac{k_0}{\rho_0} & -ik_0 s_0 & -i\omega \\ ik_0 & 0 & -i\omega\rho_{s,0}\end{vmatrix},
\end{aligned}
\tag{A.2}
$$

$$
\begin{aligned}
= \;& i\omega\frac{\partial\rho s}{\partial P}[(ik_0\rho_{s,0})(ik_0 s_0)(-i\omega\rho_{n,0}) - (-i\omega\frac{\partial\rho}{\partial T})(-i\omega)(-i\omega\rho_{n,0}) \\
- \;& (ik_0\rho_{n,0})(ik_0 s_0)(-i\omega\rho_{s,0})] \\
- \;& i\omega\frac{\partial\rho s}{\partial T}[(ik_0\rho_{s,0})(i\frac{k_0}{\rho_0})(-i\omega\rho_{n,0}) + (ik_0\rho_{n,0})(-i\omega)(ik_0) \\
- \;& (-i\omega\frac{\partial\rho}{\partial T})(-i\omega)(-i\omega\rho_{n,0}) - (ik_0\rho_{n,0})(i\frac{k_0}{\rho_0})(-i\omega\rho_{s,0})] \\
- \;& ik_0\rho_0 s_0[(-i\omega\frac{\partial\rho}{\partial T})(-i\omega)(ik_0) + (-i\omega\frac{\partial\rho}{\partial P})(-ik_0 s_0)(-i\omega\rho_{s,0}) \\
- \;& (-i\omega\frac{\partial\rho}{\partial T})(i\frac{k_0}{\rho_0})(-i\omega\rho_{s,0}) - (ik_0\rho_{s,0})(-ik_0 s_0)(ik_0)],
\end{aligned}
\tag{A.3}
$$

$$
\begin{aligned}
= \;& i\omega\frac{\partial\rho s}{\partial P}[ik_0^2\omega s_0\rho_{n,0}\rho_{s,0} - i\omega^3\rho_{n,0}\frac{\partial\rho}{\partial T} - i\omega k_0^2 s_0\rho_{n,0}\rho_{s,0}] \\
- \;& i\omega\frac{\partial\rho s}{\partial T}[i\omega\frac{k_0^2}{\rho_0}\rho_{n,0}\rho_{s,0} + i\omega k_0^2\rho_{n,0} - i\omega^3\rho_{n,0}\frac{\partial\rho}{\partial P} - i\omega\frac{k_0^2}{\rho_0}\rho_{n,0}\rho_{s,0}]
\end{aligned}
$$

$$
\begin{aligned}
- \; & ik_0\rho_0 s_0[-i\omega^2 k_0 \frac{\partial \rho}{\partial T} + i\omega^2 k_0 s_0 \frac{\partial \rho}{\partial P}\rho_{s,0} i\omega^2 \frac{k_0}{\rho_0}\frac{\partial \rho}{\partial T}\rho_{s,0} \\
- \; & ik_0^3 s_0 \rho_{s,0}], \qquad \text{(A.4)}
\end{aligned}
$$

$$
\begin{aligned}
= \; & \omega^2 \frac{\partial \rho s}{\partial P} k_0^2 s_0 \rho_{n,0}\rho_{s,0} + \omega^4 \frac{\partial \rho s}{\partial T}\rho_{n,0} \\
+ \; & \omega^2 \frac{\partial \rho s}{\partial P} k_0^2 s_0 \rho_{n,0}\rho_{s,0} + \omega^2 \frac{\partial \rho s}{\partial T}\frac{k_0^2}{\rho_0}\rho_{n,0}\rho_{s,0} \\
+ \; & \omega^2 \frac{\partial \rho s}{\partial T} k_0^2 \rho_{n,0} - \omega^4 \frac{\partial \rho s}{\partial T}\frac{\partial \rho}{\partial P}\rho_{n,0} \\
- \; & \omega^2 \frac{\partial \rho s}{\partial T}\frac{k_0^2}{\rho_0}\rho_{n,0}\rho_{s,0} - k_0^2 \rho_0 s_0 \omega^2 \frac{\partial \rho}{\partial T} \\
+ \; & k_0^2 \rho_0 s_0^2 \omega^2 \frac{\partial \rho}{\partial P}\rho_{s,0} + k_0^2 s_0 \omega^2 \frac{\partial \rho}{\partial P}\rho_{s,0} \\
- \; & k_0^4 \rho_0 s_0^2 \rho_{s,0}. \qquad \text{(A.5)}
\end{aligned}
$$

Then $|A|$ can be simplified as the following form,

$$
\begin{aligned}
|A| \; = \; & \omega^4 \frac{\partial \rho s}{\partial T}\rho_{n,0} - \omega^4 \frac{\partial \rho s}{\partial T}\frac{\partial \rho}{\partial P}\rho_{n,0} + \omega^2 \frac{\partial \rho s}{\partial T} k_0^2 \rho_{n,0} \\
- \; & -k_0^2 \rho_0 s_0 \omega^2 \frac{\partial \rho}{\partial T} + k_0^2 \rho_0 s_0^2 \omega^2 \frac{\partial \rho}{\partial P}\rho_{s,0} + k_0^2 s_0 \omega^2 \frac{\partial \rho}{\partial P}\rho_{s,0} \\
- \; & k_0^4 \rho_0 s_0^2 \rho_{s,0}. \qquad \text{(A.6)}
\end{aligned}
$$

Again it must vanish in order for there to exist a nontrivial solution,

$$
|A| = 0 \qquad \text{(A.7)}
$$

If both side of Eq.(A.7) is divided by k_0^4, we get following equation.

$$
\frac{\omega^4}{k^4}\frac{\partial \rho s}{\partial P}\frac{\partial \rho}{\partial T}\rho_n + \frac{\omega^4}{k^4}\frac{\partial \rho s}{\partial T}\frac{\partial \rho}{\partial P}\rho_n \frac{\omega^2}{k^2}\frac{\partial \rho s}{\partial T}\rho_n - \frac{\omega^2}{k^2}\rho s \frac{\partial \rho}{\partial T}
$$

$$
\begin{aligned}
&+ \frac{\omega^2}{k^2}\rho_0 s^2 \frac{\partial \rho}{\partial P}\rho_s + \frac{\omega^2}{k^2} s\rho_s \frac{\partial \rho}{\partial T} - s^2 \rho\rho_s \\
&= 0.
\end{aligned} \tag{A.8}
$$

Here, the subscript 0 is abbreviated. According to chain rule, we have

$$
\frac{\partial \rho s}{\partial P} = \rho\left(\frac{\partial s}{\partial P}\right)_\rho + s\left(\frac{\partial \rho}{\partial P}\right)_s. \tag{A.9}
$$

Here, the following equations are introduced.

$$
\begin{aligned}
u^2 &= \frac{\omega^2}{k_0^2}, \quad u_1^2 = \left(\frac{\partial P}{\partial \rho}\right)_s, \quad u_2^2 = \frac{\rho_s s^2 T}{\rho_n C_V}, \\
C_V &= T\left(\frac{\partial s}{\partial T}\right)_\rho, \quad C_P = T\left(\frac{\partial s}{\partial T}\right)_P.
\end{aligned} \tag{A.10}
$$

And according to thermodynamic identities

$$
\left[\left(\frac{\partial s}{\partial T}\right)_P\left(\frac{\partial \rho}{\partial P}\right)_T - \left(\frac{\partial s}{\partial P}\right)_T\left(\frac{\partial \rho}{\partial T}\right)_P\right] = \left(\frac{\partial s}{\partial T}\right)_P\left(\frac{\partial P}{\partial \rho}\right)_\rho^{-1} = \left(\frac{\partial s}{\partial T}\right)_\rho\left(\frac{\partial \rho}{\partial P}\right)_T. \tag{A.11}
$$

Using those Eq.s (A.10) and(A.9) , Eq.(A.8) can be written into the following form.

$$
\begin{aligned}
&u^4\rho_n\left(\left[\left(\frac{\partial s}{\partial P}\right)_\rho\left(\frac{\partial \rho}{\partial T}\right) - \left(\frac{\partial s}{\partial T}\right)_\rho\left(\frac{\partial \rho}{\partial P}\right)\right] + s\left[\left(\frac{\partial \rho}{\partial P}\right)_s\left(\frac{\partial \rho}{\partial T}\right) - \left(\frac{\partial \rho}{\partial T}\right)_s\left(\frac{\partial \rho}{\partial P}\right)\right]\right) \\
&- u^2\rho_n\left(-\rho\left(\frac{\partial s}{\partial T}\right)_\rho - s\left(\frac{\partial \rho}{\partial T}\right)_s + \frac{\rho}{\rho_n}s\frac{\partial \rho}{\partial T} - \frac{\rho}{\rho_n}s^2\frac{\partial \rho}{\partial P}\rho_s - \frac{\rho_s}{\rho_n}s\frac{\partial \rho}{\partial T}\right) \\
&- \rho_n\rho\frac{\rho_s}{\rho_n}s^2 = 0.
\end{aligned} \tag{A.12}
$$

Using the fundamental identity of two-fluid equation

$$
\rho = \rho_n + \rho_s, \tag{A.13}
$$

We have

$$\begin{aligned} -\frac{\rho}{\rho_n} s \frac{\partial \rho}{\partial T} + \frac{\rho_s}{\rho_n} s \frac{\partial \rho}{\partial T} &= \frac{s}{\rho_n} \frac{\partial \rho}{\partial T} (-\rho + \rho_s) \\ &= -s \frac{\partial \rho}{\partial T}. \end{aligned} \tag{A.14}$$

Substituting Eq.s (A.11) and (A.13) into Eq. (A.12) and dividing both side of the equation by ρ, the equation can be simplified as follows.

$$u^4 \left(\frac{\partial s}{\partial T}\right)_\rho \left(\frac{\partial \rho}{\partial P}\right)_T - u^2 \left[\left(\frac{\partial s}{\partial T}\right)_\rho + \frac{s^2}{\rho_n} \rho_s \left(\frac{\partial \rho}{\partial P}\right)\right] + \frac{\rho_s}{\rho_n} s^2 = 0. \tag{A.15}$$

Then we get the following equation

$$u^4 - u^2 \left[\left(\frac{\partial P}{\partial \rho}\right)_s + \frac{\rho_s}{\rho_n} s^2 \left(\frac{\partial s}{\partial T}\right)_\rho^{-1}\right] + \left(\frac{\partial s}{\partial T}\right)_P^{-1} \left(\frac{\partial P}{\partial \rho}\right)_s \frac{\rho_s}{\rho_n} s^2 = 0. \tag{A.16}$$

Again using the thermodynamic Eq.s (A.10) , Eq.(A.16) can be written in the form,

$$u^4 - (u_1^2 + u_2^2) u^2 + \frac{C_V}{C_P} u_1^2 u_2^2 = 0. \tag{A.17}$$

Finally the dispersion law Eq. (2.19) in Section 2.4 relating ω and k_0 is obtained.

$$\left(1 - \frac{u^2}{u_1^2}\right)\left(1 - \frac{u^2}{u_2^2}\right) = 1 - \frac{C_V}{C_P}.$$

Bibliography

[1] Landau, L. D. and Lifshitz, E. M. *Fluid Mechanics* Pergamon Press, Oxford, UK (1959)

[2] Gorter, C. J. and Mellink, J. H. *Physica* (1949) **15** 285-305

[3] Vinen, W. F. *Proc. Roy. Soc. A* (1957) **240** 114-127

[4] Vinen, W. F. *Proc. Roy. Soc. A* (1957) **240** 128-143

[5] Vinen, W. F. *Proc. Roy. Soc. A* (1957) **242** 493-515

[6] Schwarz, K. W. *Phys. Rev. B* (1988) **38** 2398-2417

[7] Liepmann, H. W. and Laguna, G. A. *Ann. Rev. Fluid Mech.* (1984) **16** 139-177

[8] Nemirovskii, S. K. *Sov. Phys. JETP* (1986) **64** 803-810

[9] Stamm, G., Olszok, Th., Schwerdtner, M. v., and Schmidt, D. W. *Cryogenics* (1992) **32** 598-600

[10] Kitabatake, S. and Sawada, Y. *J. Phys. Soc. Japan Letters* (1978) **45** 345-346

[11] Turner, T. N *Phys. Fluids* (1983) **26** 3227-3241

[12] Tisza, L. *Nature* (1938) **38** 913

[13] Feynman, R. P. *Progress in Low Temperature Physics* Amsterdam: North-Holland Pub. Co. (1955) Vol. I

[14] Peshkov, V. P. *J. Phys. USSR* (1944) **8** 381

[15] Puttermann, S. J. *Superfluid Hydrodynamics* North Holland Publishing Company Amsterdam London America Elsevier Publishing Company (1974)

[16] Donnelly, R. J. *Experimental Superfluidity* The University Chicago @press (1967)

[17] Nemirovskii, S. K. and Tsoi, A. N. *Cryogenics* (1989) **29** 985-994

[18] Fiszdon, W., Schwerdtner, M. v., Stamm, G. and Poppe, W. *J. Fluid Mech.* (1990) **212** 663-684

[19] Borner, H., Schmeling, T. and Schmidt, D. W. *J. Low Temp. Phys.* (1983) **50** 405-426

[20] Schwerdtner, M. V., Poppe, W. and Schmidt, D. W. *J. Low Temp. Phys.* (1983) **50** 405-426

[21] Murakami, M. and Iwashita, K. *comp. & fluids* (1991) **19** 443-451

[22] Nemirovskii, S. K. *private communication*

[23] A. N. Tsoi and M. O. Lutset *Inzhenerno-Fizicheskii N1* (1986) **51** 5-9

[24] Nemirovskii, S. K. *Sov. Phys. Usp.* (1990) **33** 429-452

[25] Dresner, L. *Adv. Cryo. Eng.* (1984) **29** 323-333

[26] Katsuki, Y., Murakami, M., Iida, T. and Shimazaki, T. *Adv. Cryo. Eng.* (1984) **29** 323-333

[27] Kanari, T. *private communication*

[28] Iida, T., Murakami, M. and Shimazaki, T. *J. Cryo. Soc. Japan* (1995) **30** 85-92

[29] Dessler, A. J. and Fairbank, W. M. *Phys. Rev.* (1956) **104** 6-10

ACKNOWLEDGMENT

The author would like to express his deep appreciation to Prof. M. Murakami, Institute of Engineering Mechanics, University of Tsukuba for his great support and continuous encouragement. The author would like to thank the member of the Murakami laboratory at University of Tsukuba for their helpful assistance.

The author also would like to express his deep gratitude to Prof. Y. Kobayashi, Prof. K. Matsuuchi, Prof. H. Nariai and Prof. Y. Yoshizawa, Institute of Engineering Mechanics, University of Tsukuba for their judgment of this dissertation.

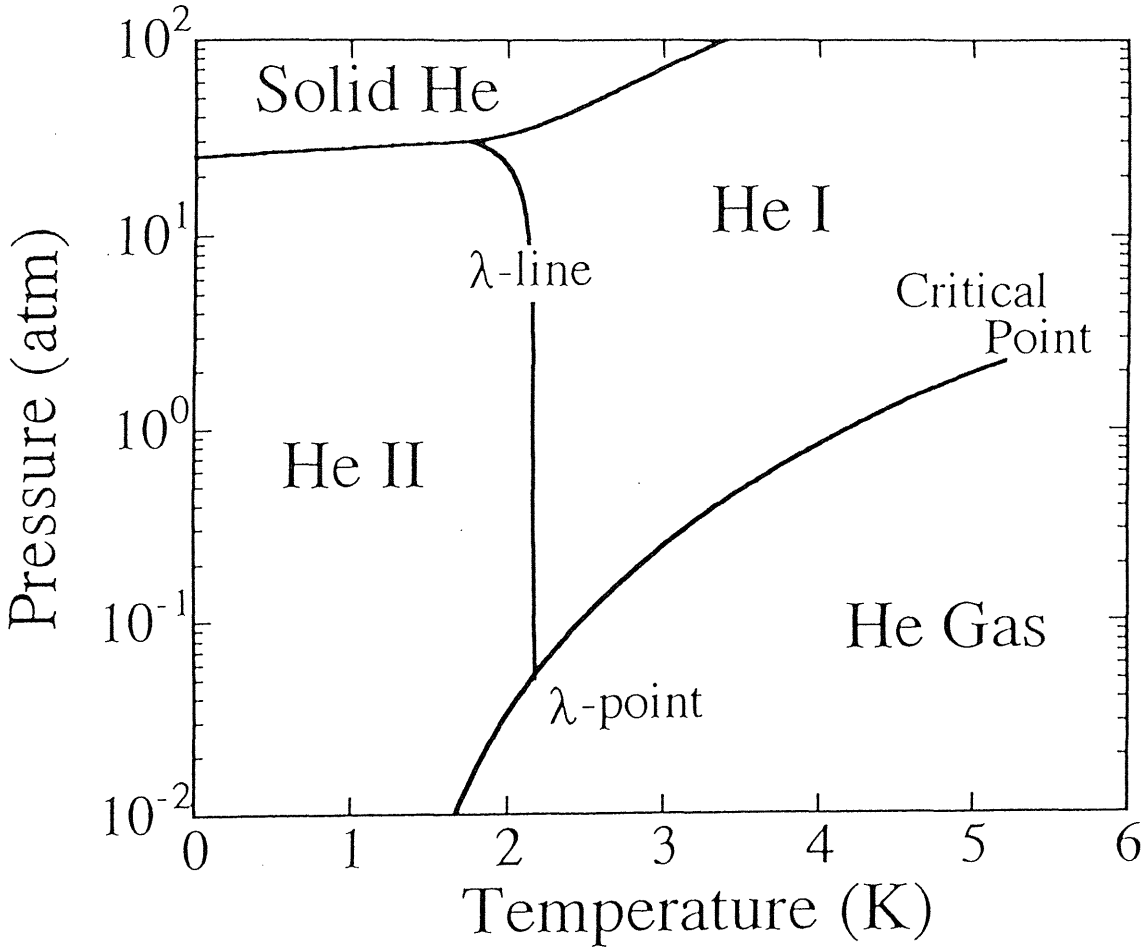

Figure 2.1 Phase diagram of ^{4}He.

	Superfluid component	Normal fluid component
Density	ρ_s	ρ_n
Viscosity	0	η_n
Entropy	0	s
Bose-Einstein statics	ground state	excited state

Figure 2.2 Two-fluid model.

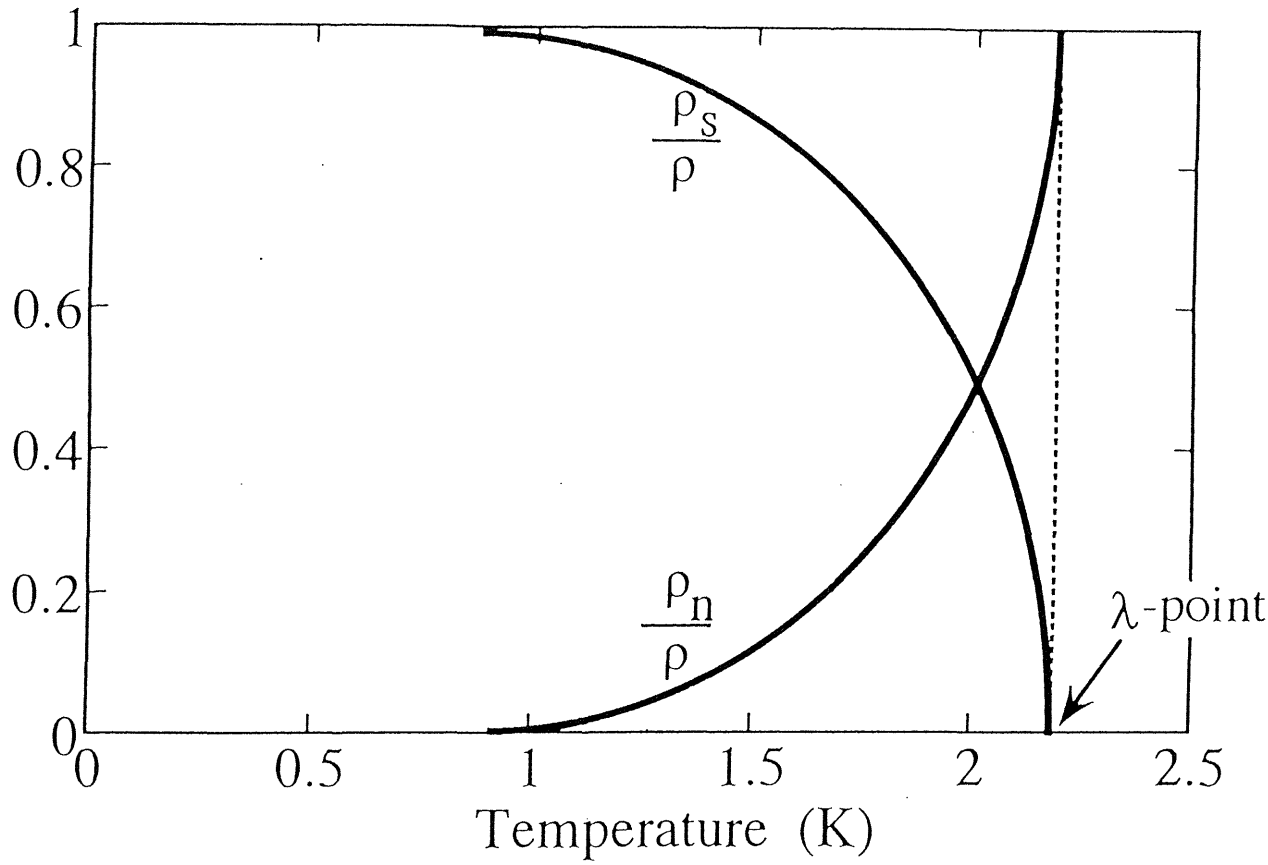

Figure 2.3 The ratio of the normal fluid density and superfluid density to the total density as a function of temperature.

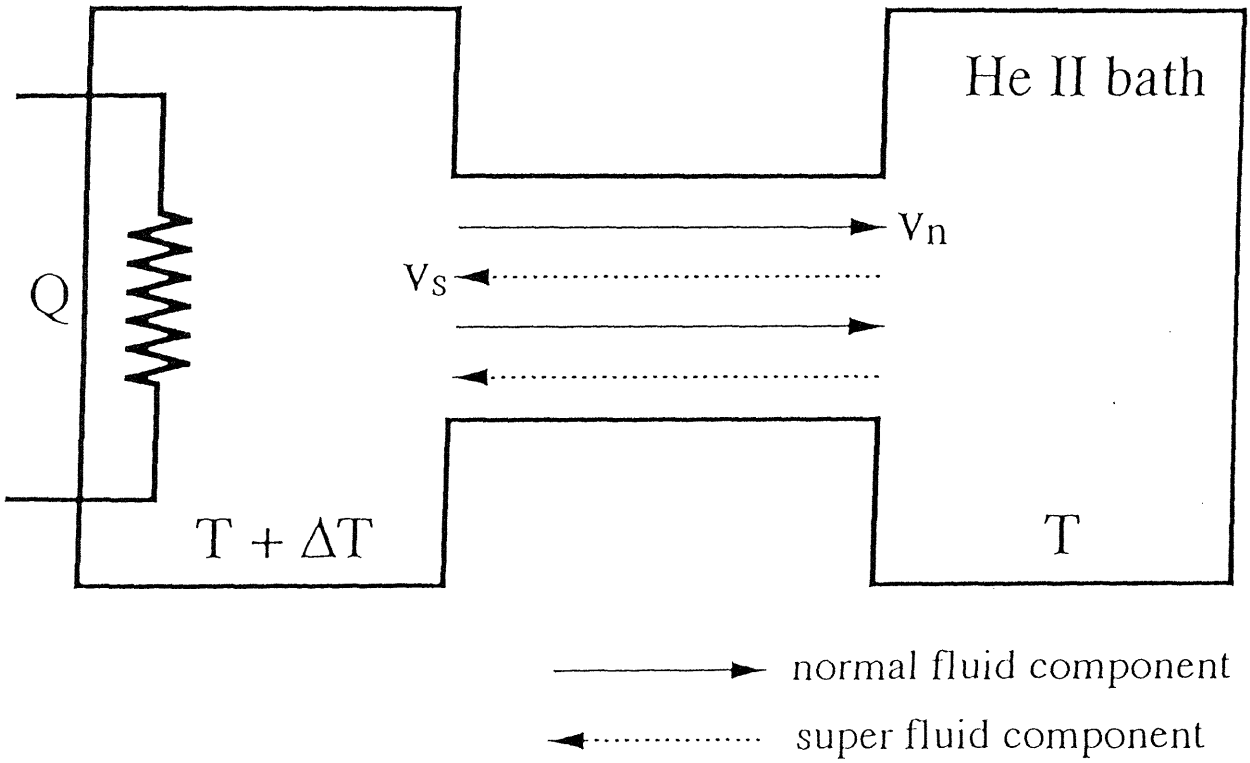

Figure 2.4 Model of thermal counterflow.

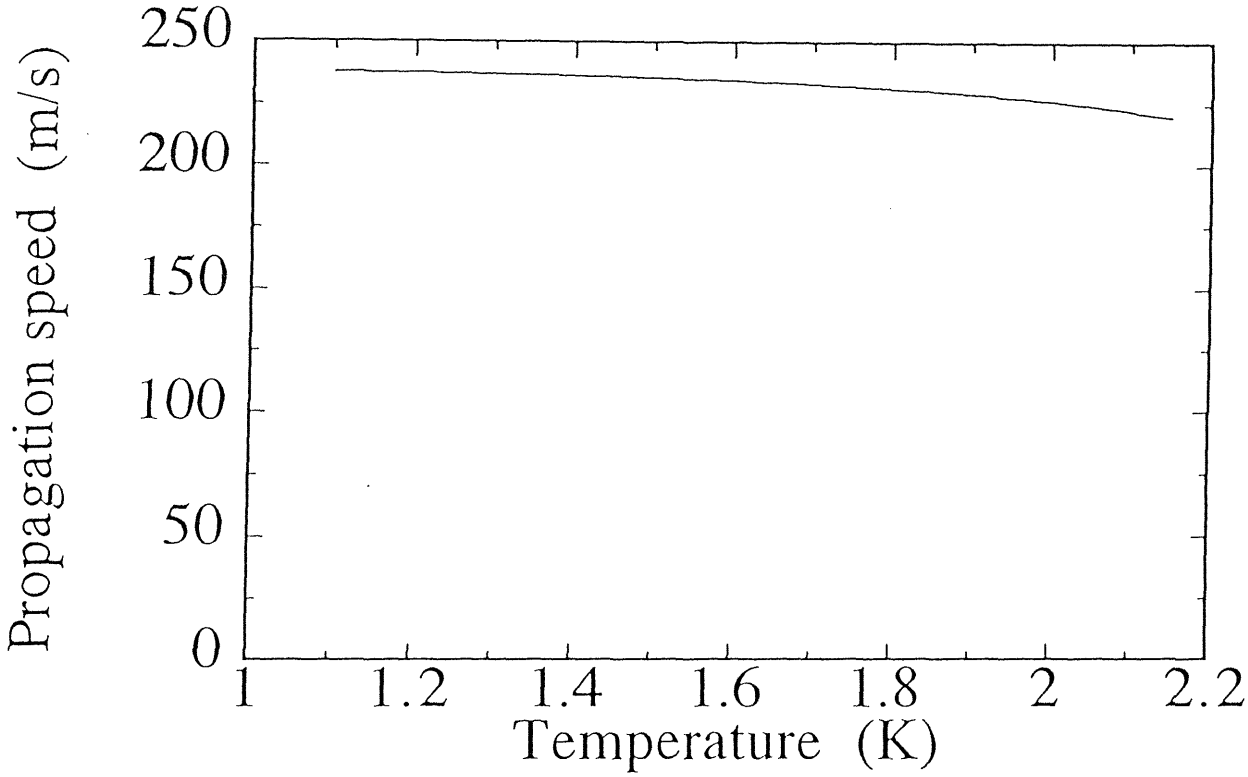

Figure 2.5 Propagation speed of the first sound wave as a function of temperature.

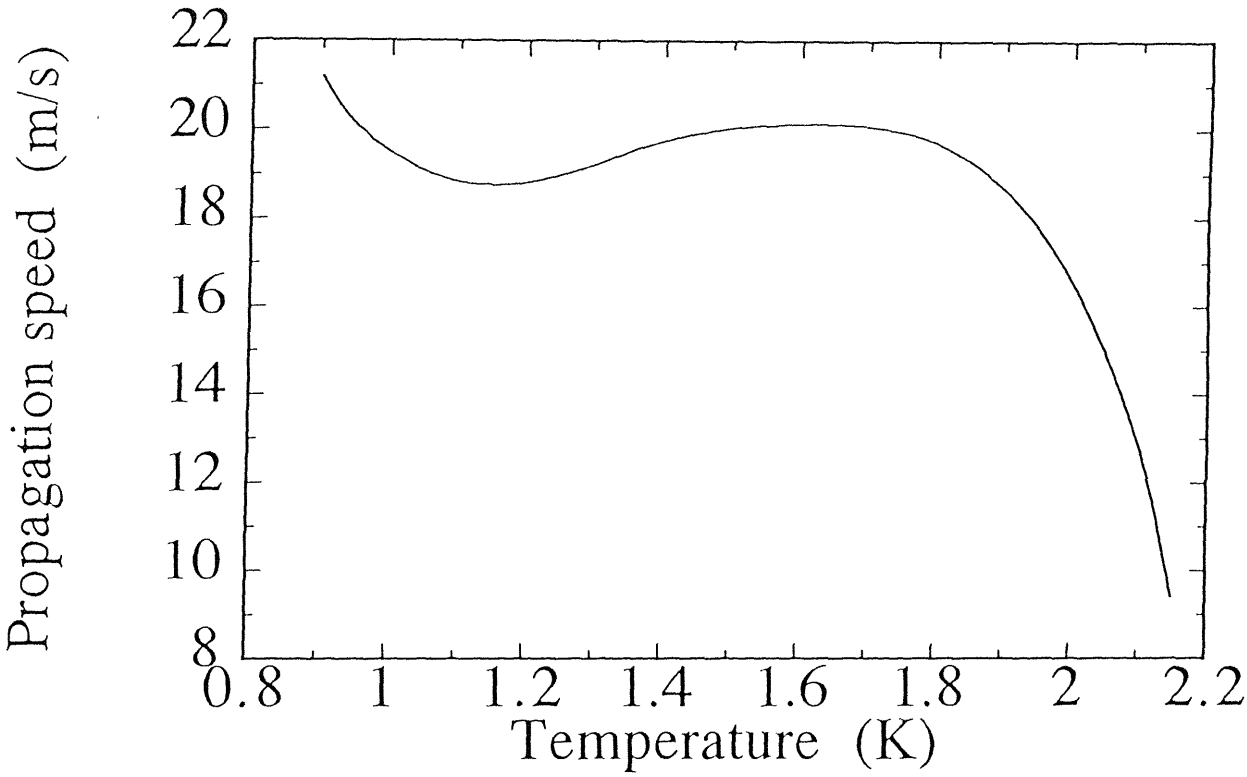

Figure 2.6 Propagation speed of the second sound wave as a function of temperature.

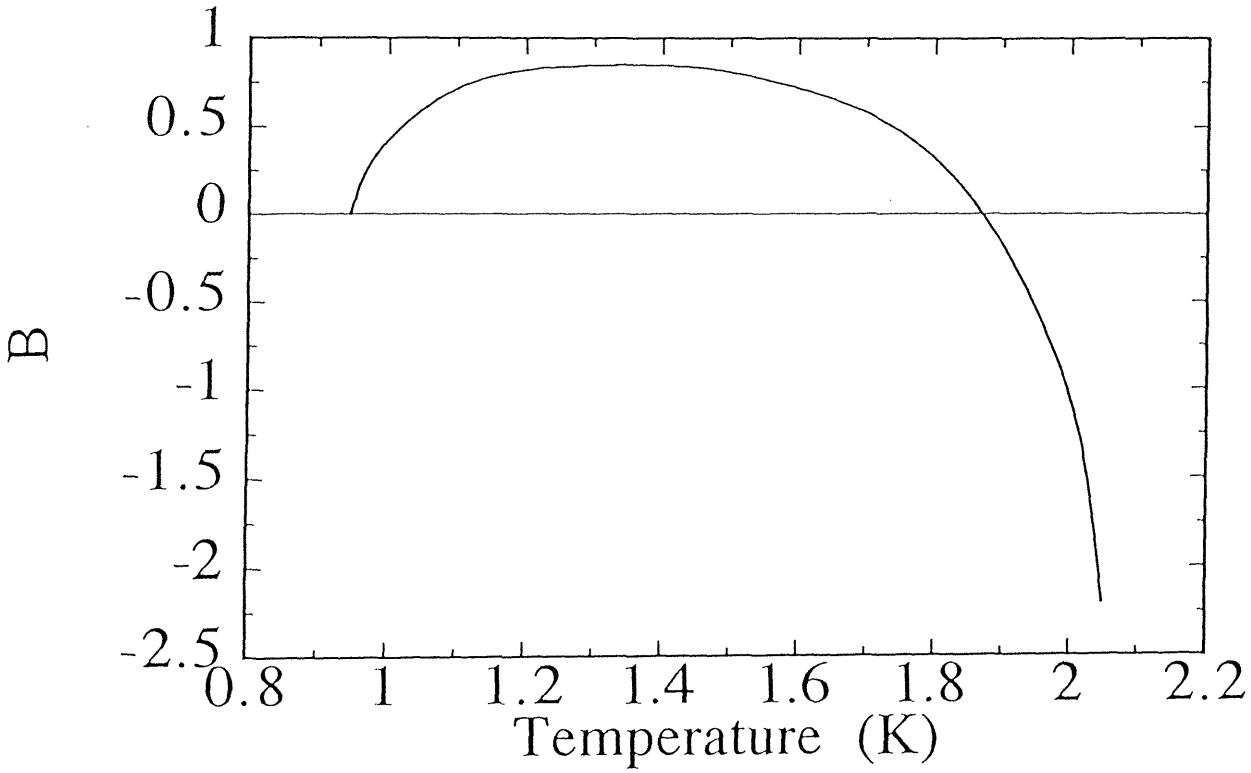

Figure 2.7 Temperature dependence of steeping coefficient B

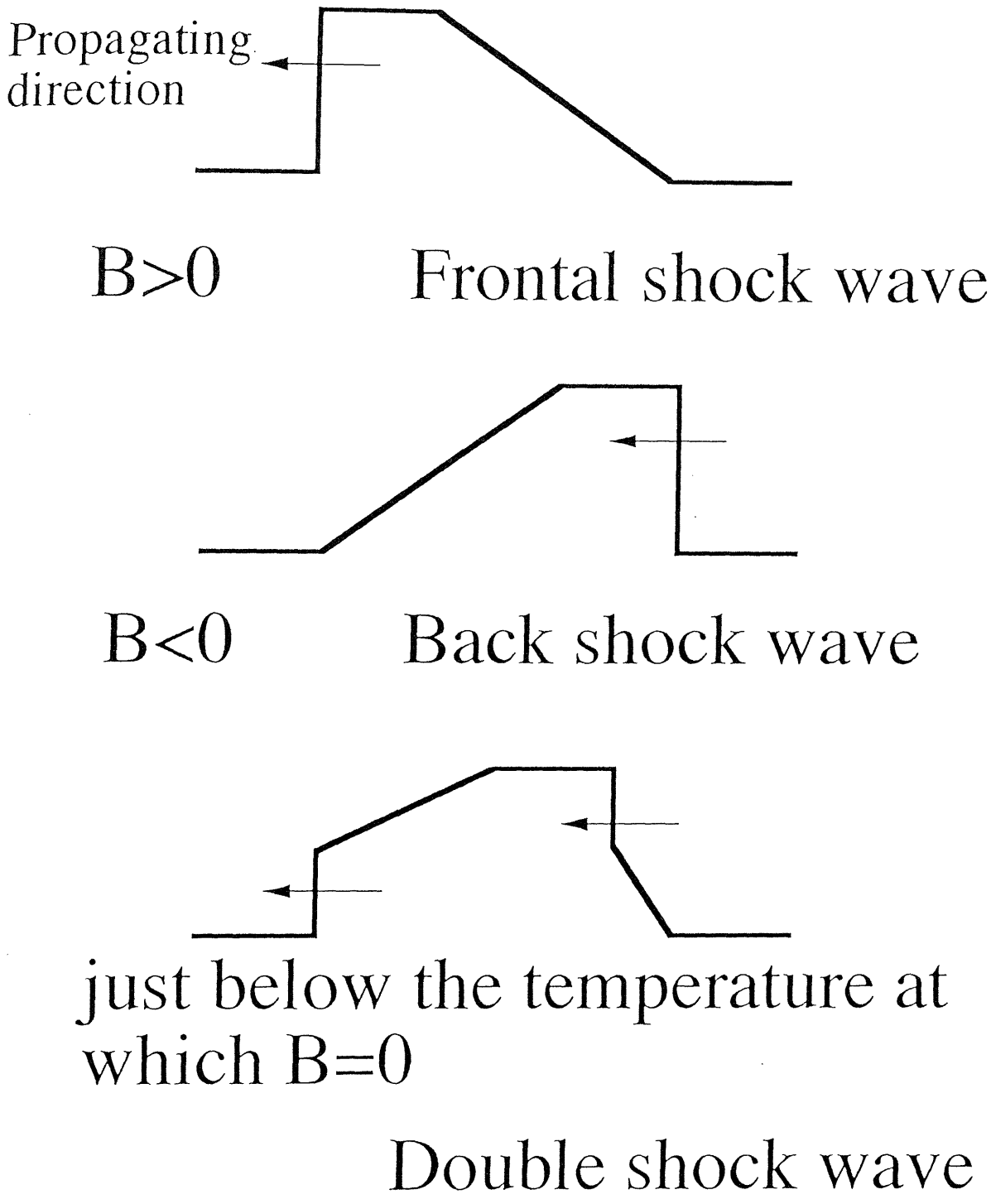

Figure 2.8 Three kinds of typical thermal shock wave forms generated by trapezoidal heat pulse.

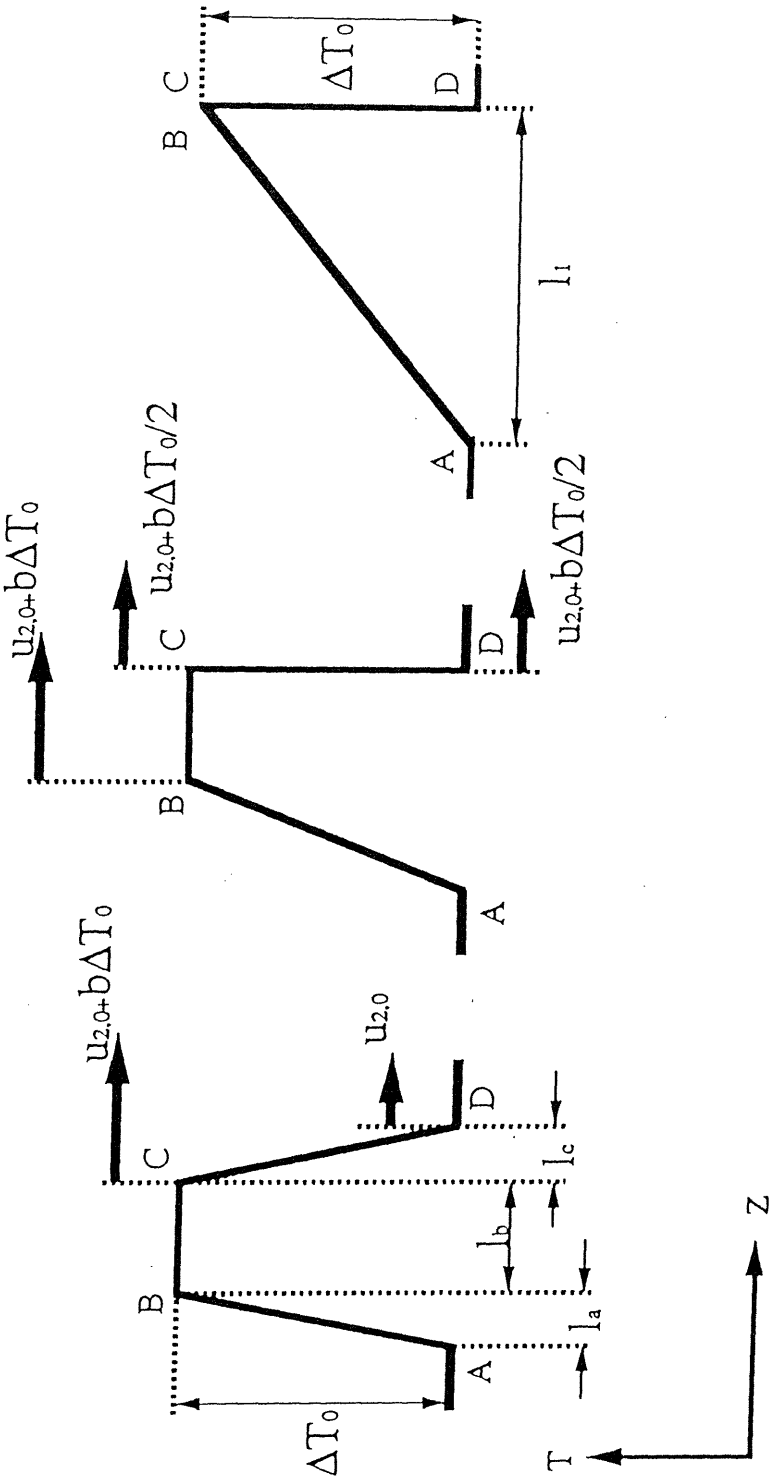

Figure 2.9 Schematic drawing of a nonlinear wave from variation through propagation. Initial trapezoidal profile becomes triangular. This figure shows the spatial temperature distribution associate with a wave. Propagation speed of points on a wave profile are also indicated.

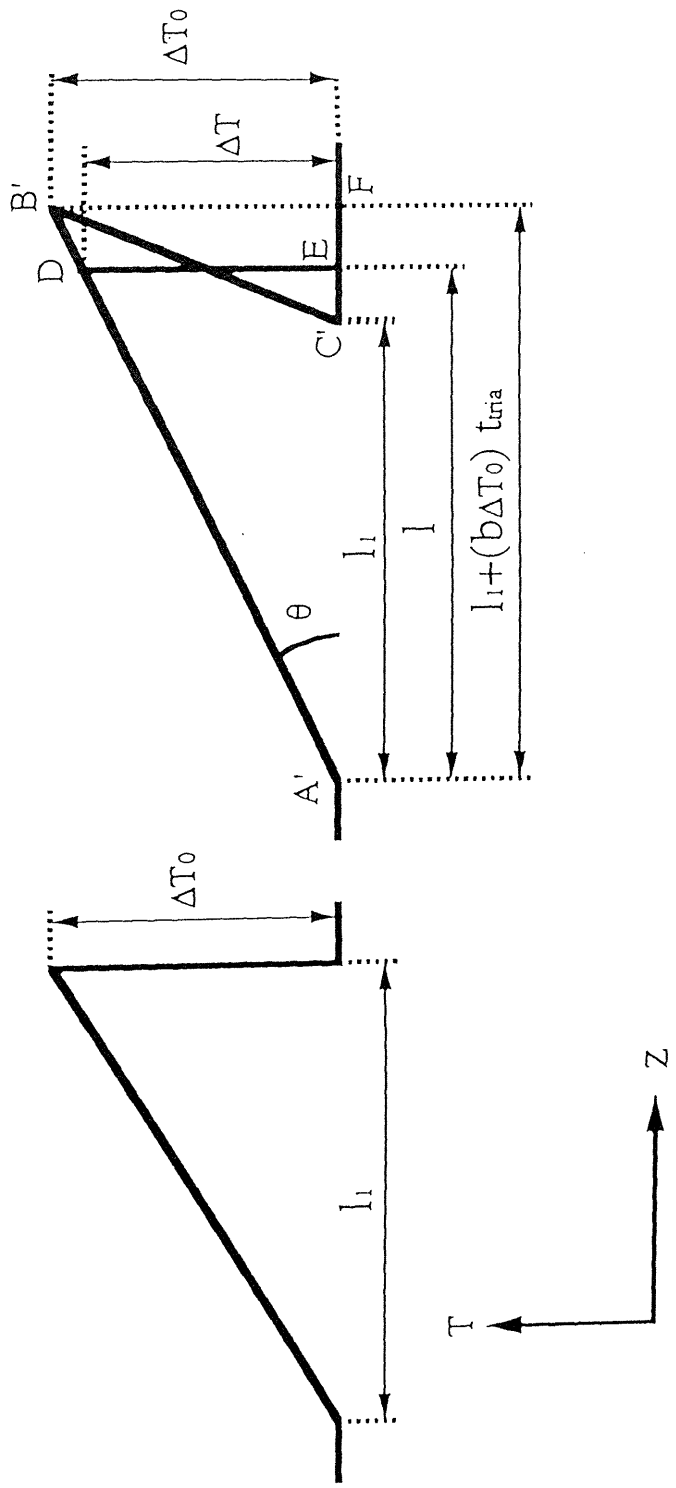

Figure 2.10 Schematic drawing of a nonlinear wave from variation after the formation of a triangular profile.

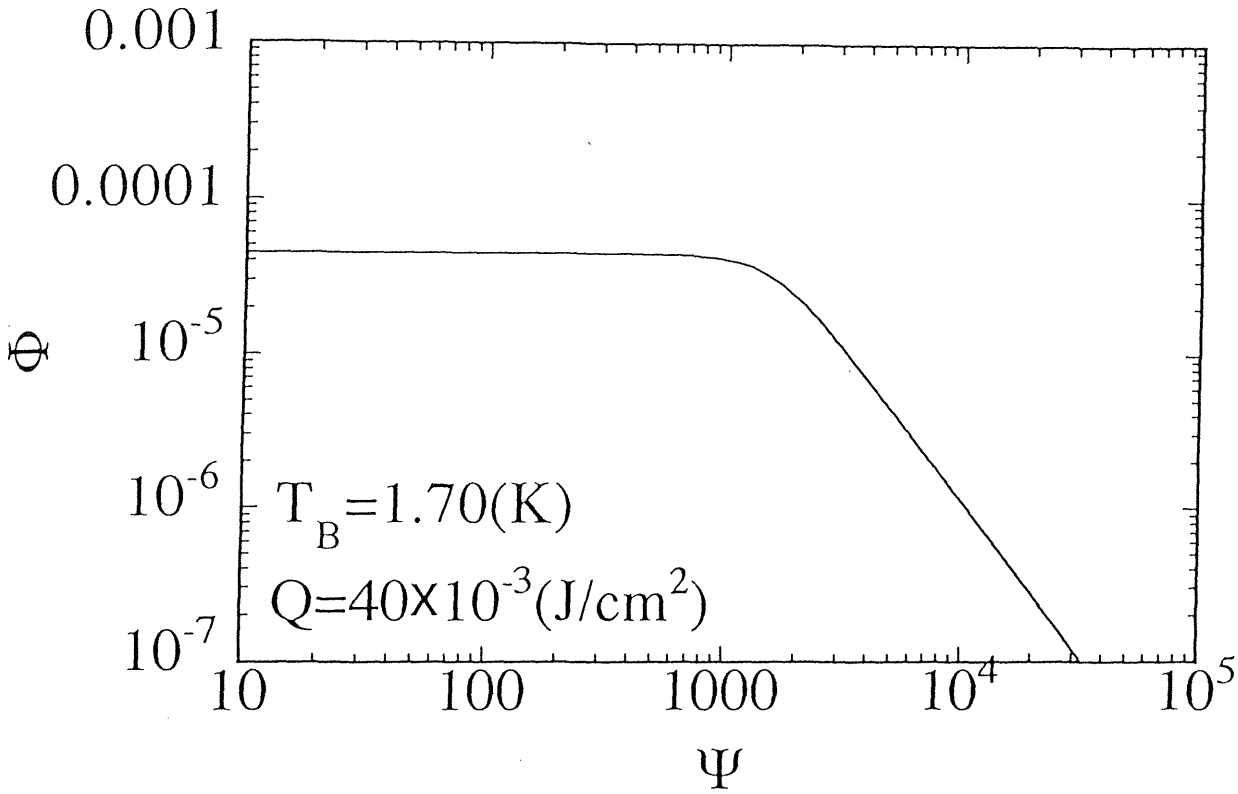

Figure 2.11 Example of the solution of Eq. (2.68) for the conditions of $T_B = 1.70K$ and $Q = 40 \times 10^{-3} J/cm^2$.

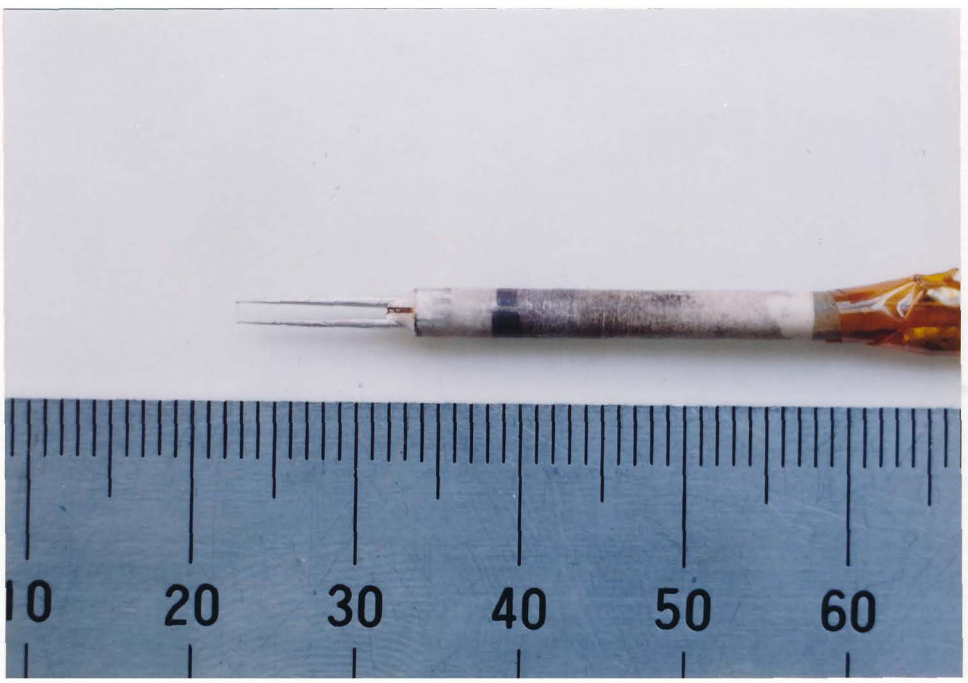

Figure 3.1 Picture of a superconductive temperature sensor.

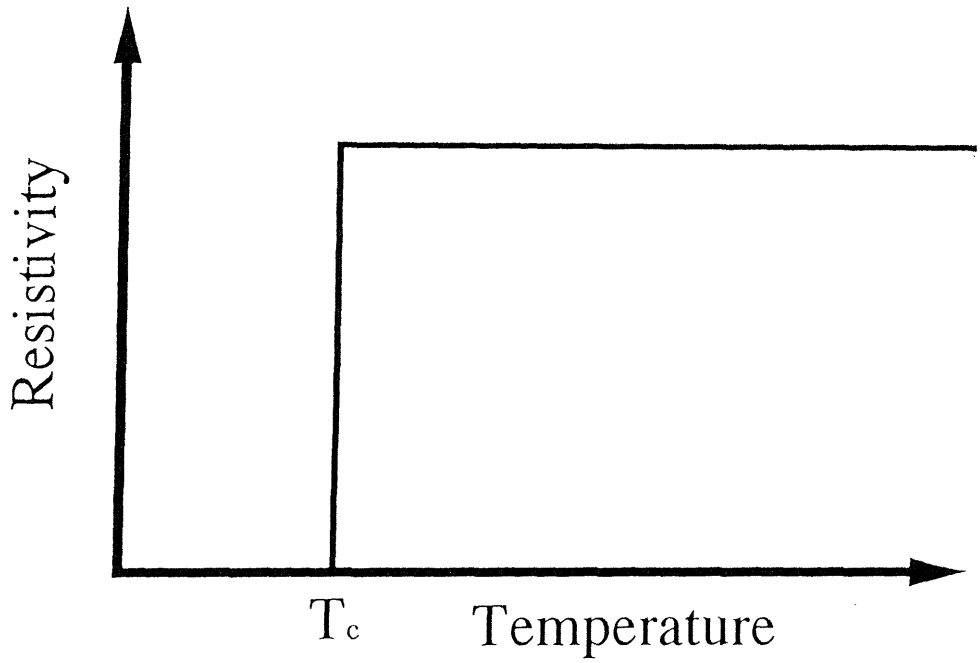

Figure 3.2 Ideal resistivity variation with temperature of type I superconductor. T_c is the critical temperature

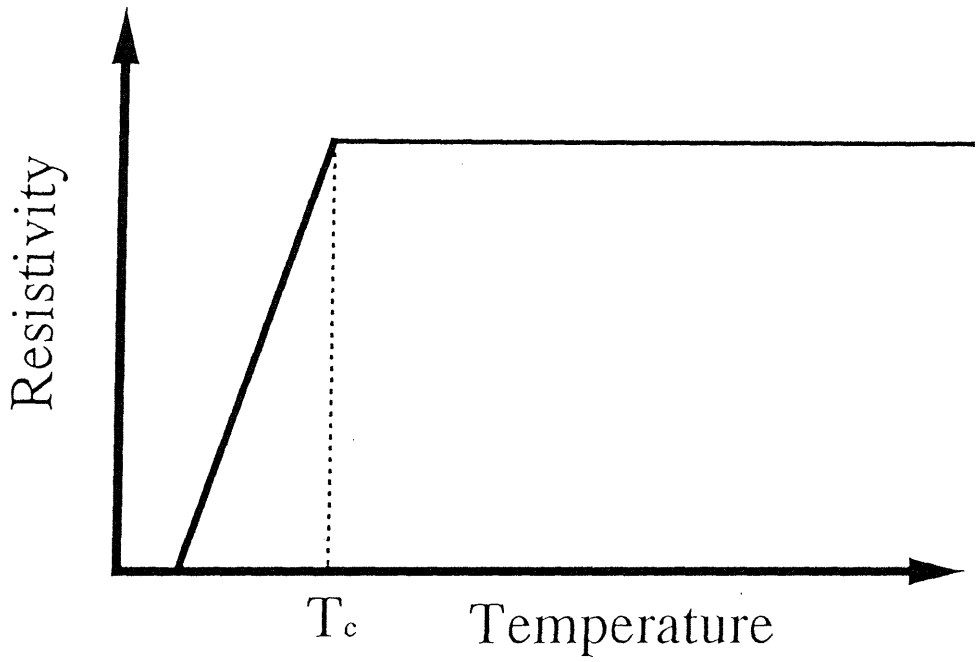

Figure 3.3 Ideal resistivity variation with temperature of type II superconductor. T_c is the critical temperature

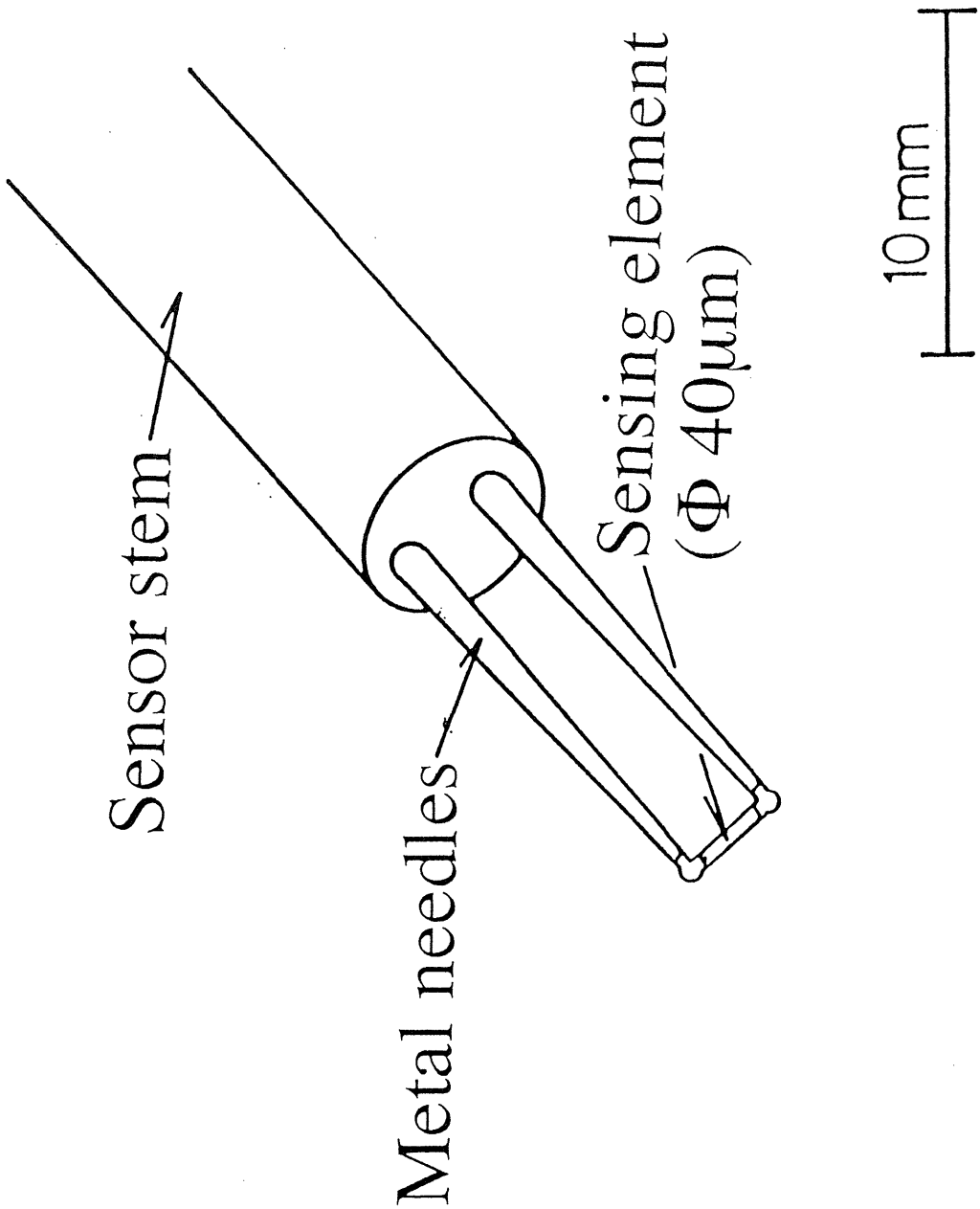

Figure 3.4 Schematic drawing of a superconductive temperature sensor.

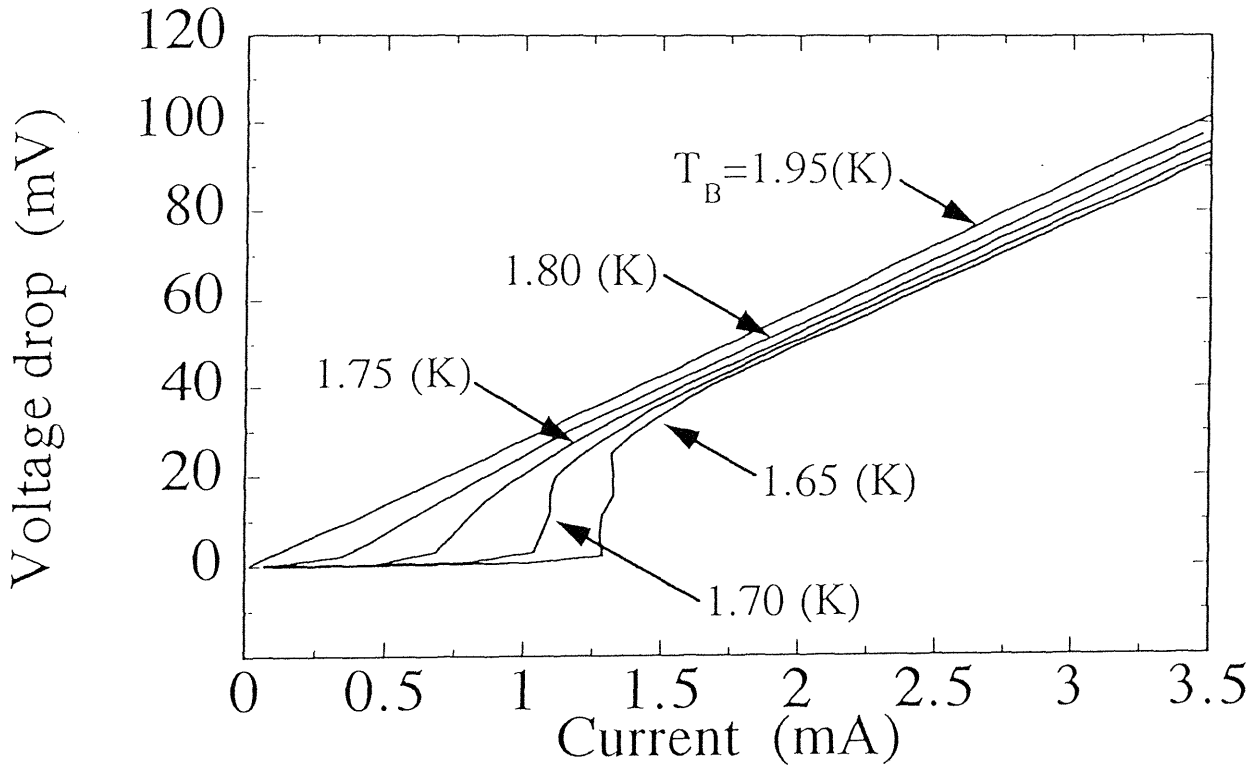

Figure 3.5 Typical voltage – current characteristics of a superconductive temperature sensor. Temperature is taken as a parameter.

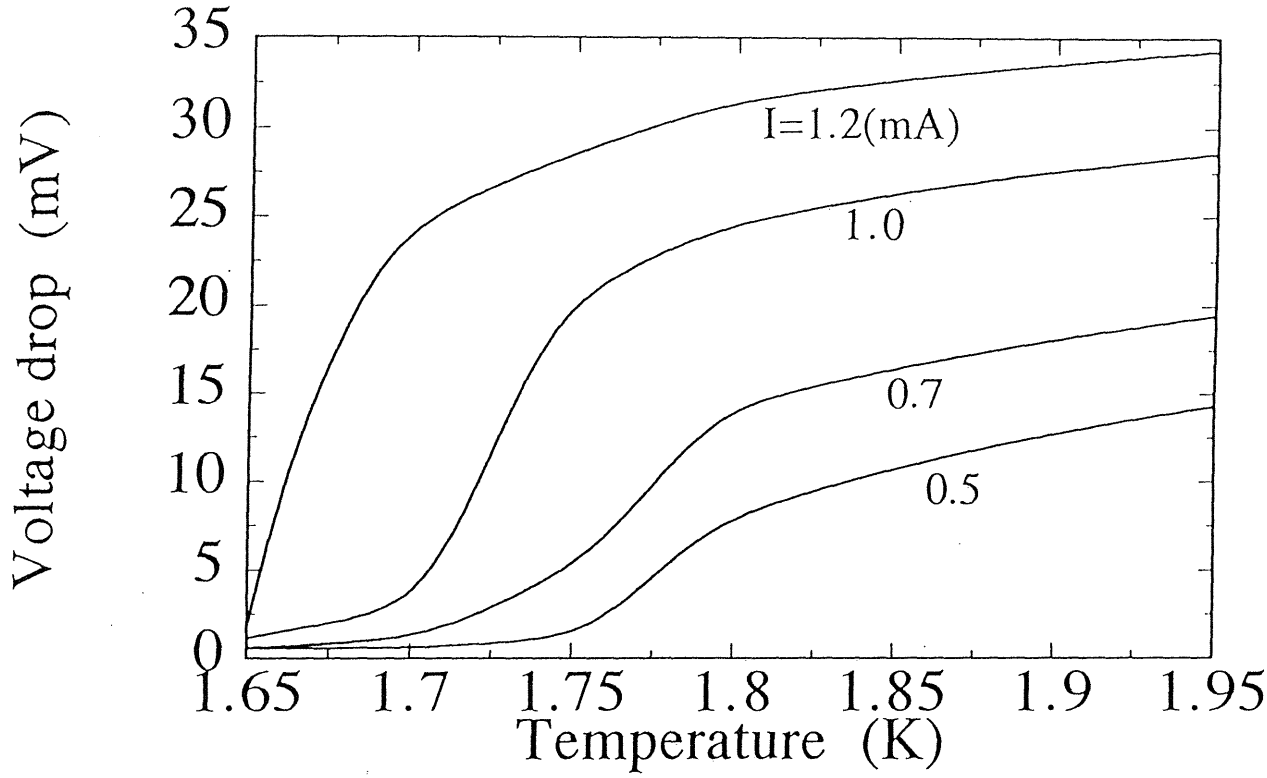

Figure 3.6 Typical voltage – temperature characteristics of a superconductive temperature sensor. I is the bias current to a sensor.

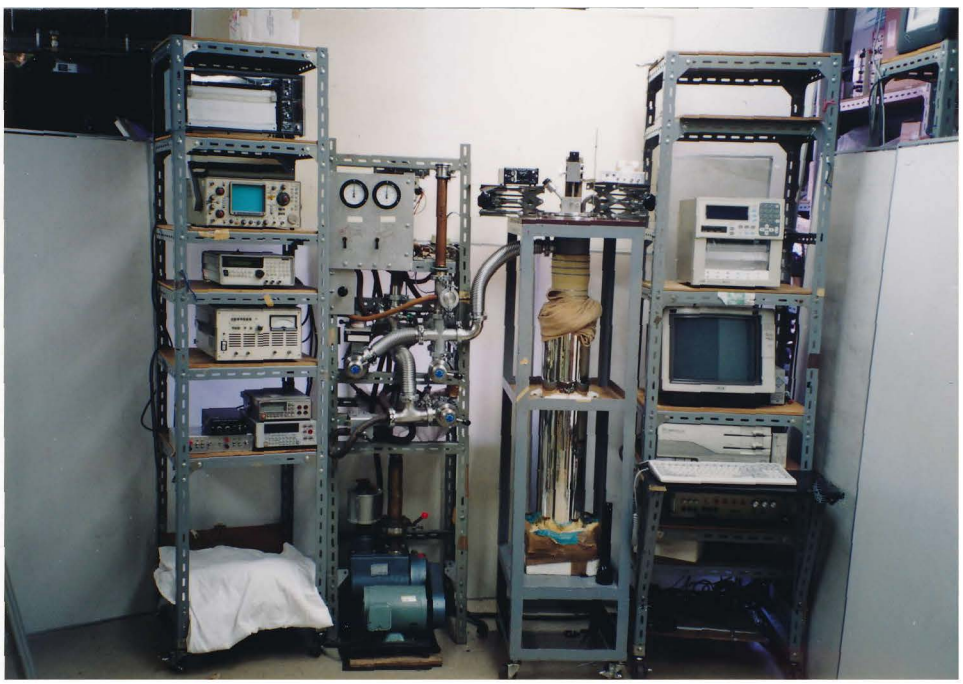

Figure 4.1 General view of the whole experimental set up.

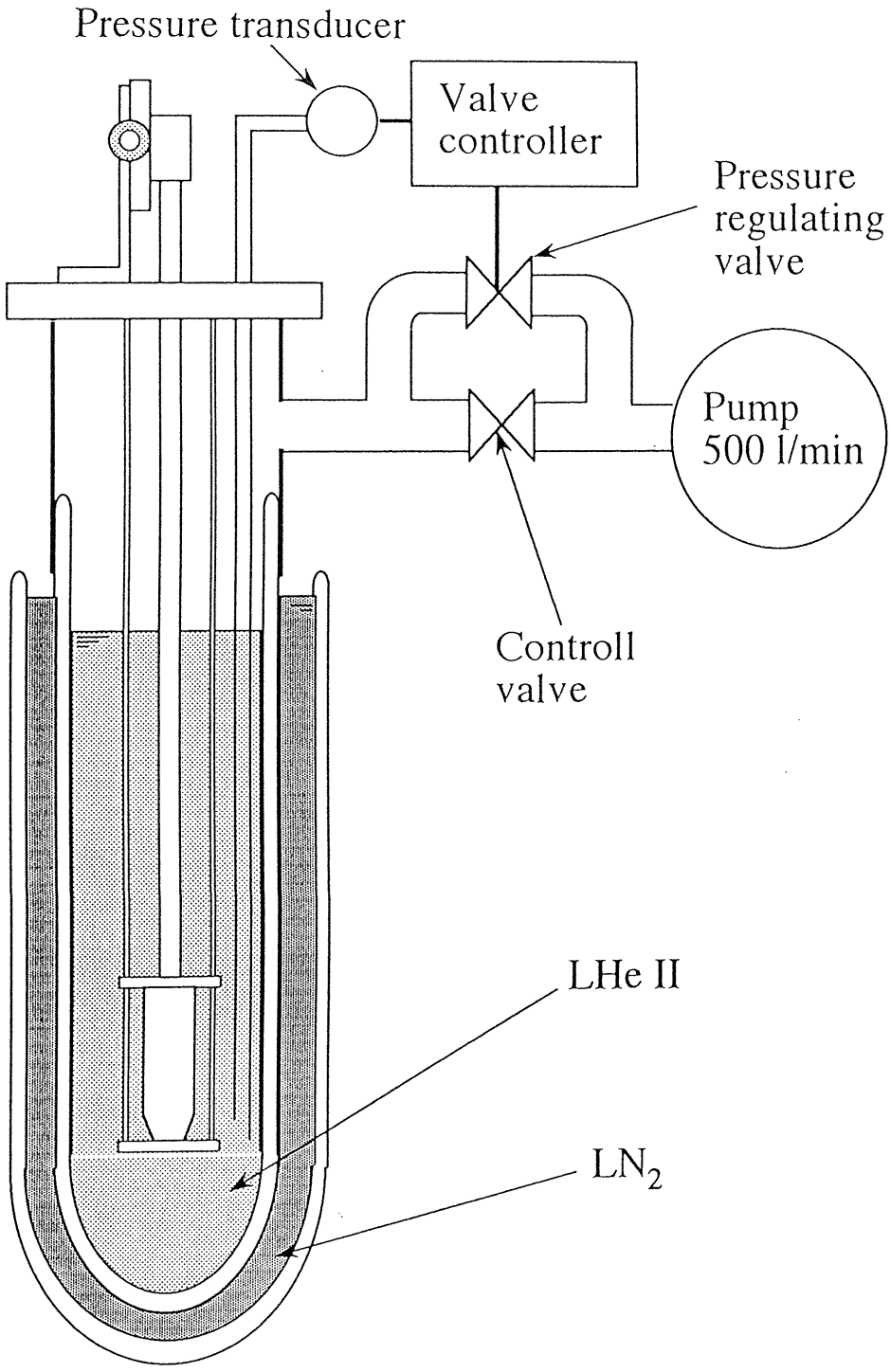

Figure 4.2 Schematic illustration of the He II dewar and the evacuation system.

Figure 4.3 Picture of the cryogenic flange inserted into the He II dewar.

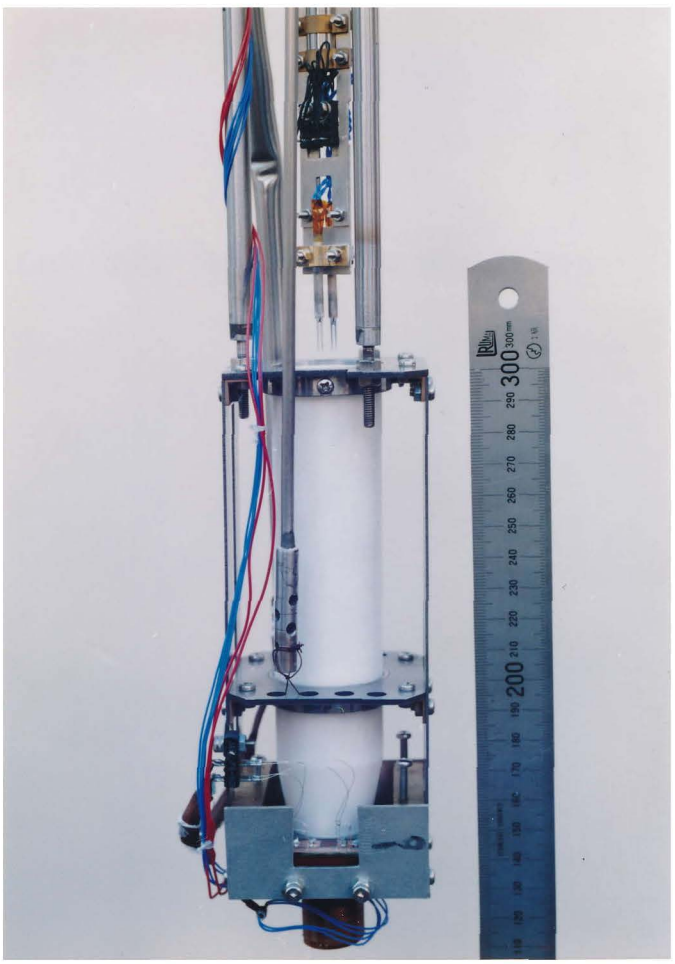

Figure 4.4 Picture of the main assembly of the experimental apparatus immersed in He II. Two superconductive temperature sensors are mounted on the movable temperature sensor mount in this picture.

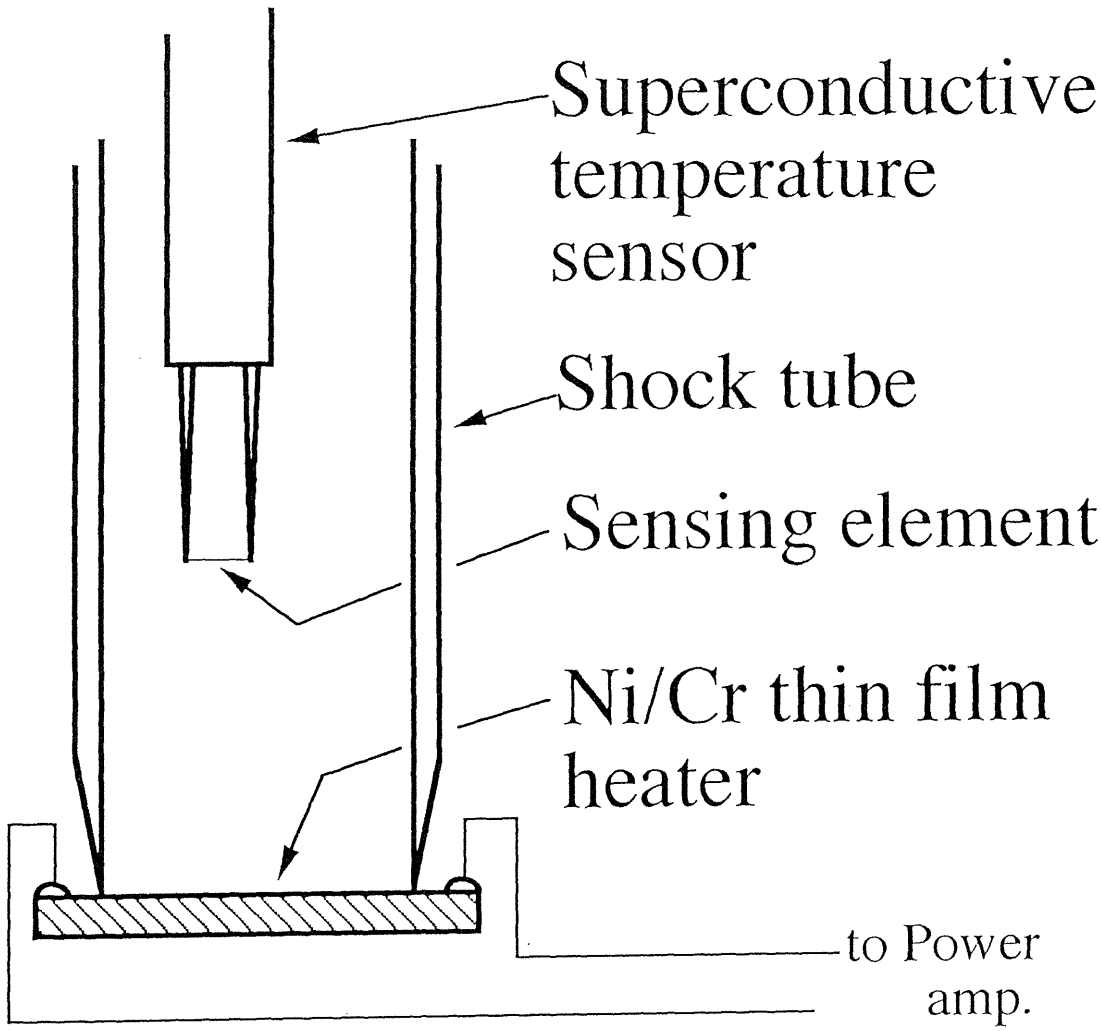

Figure 4.5 Schematic drawing of the main assembly of the experimental apparatus. It consists of three main parts, a planar Ni/Cr thin film heater, a cylindrical thermal shock tube and a superconductive temperature sensor.

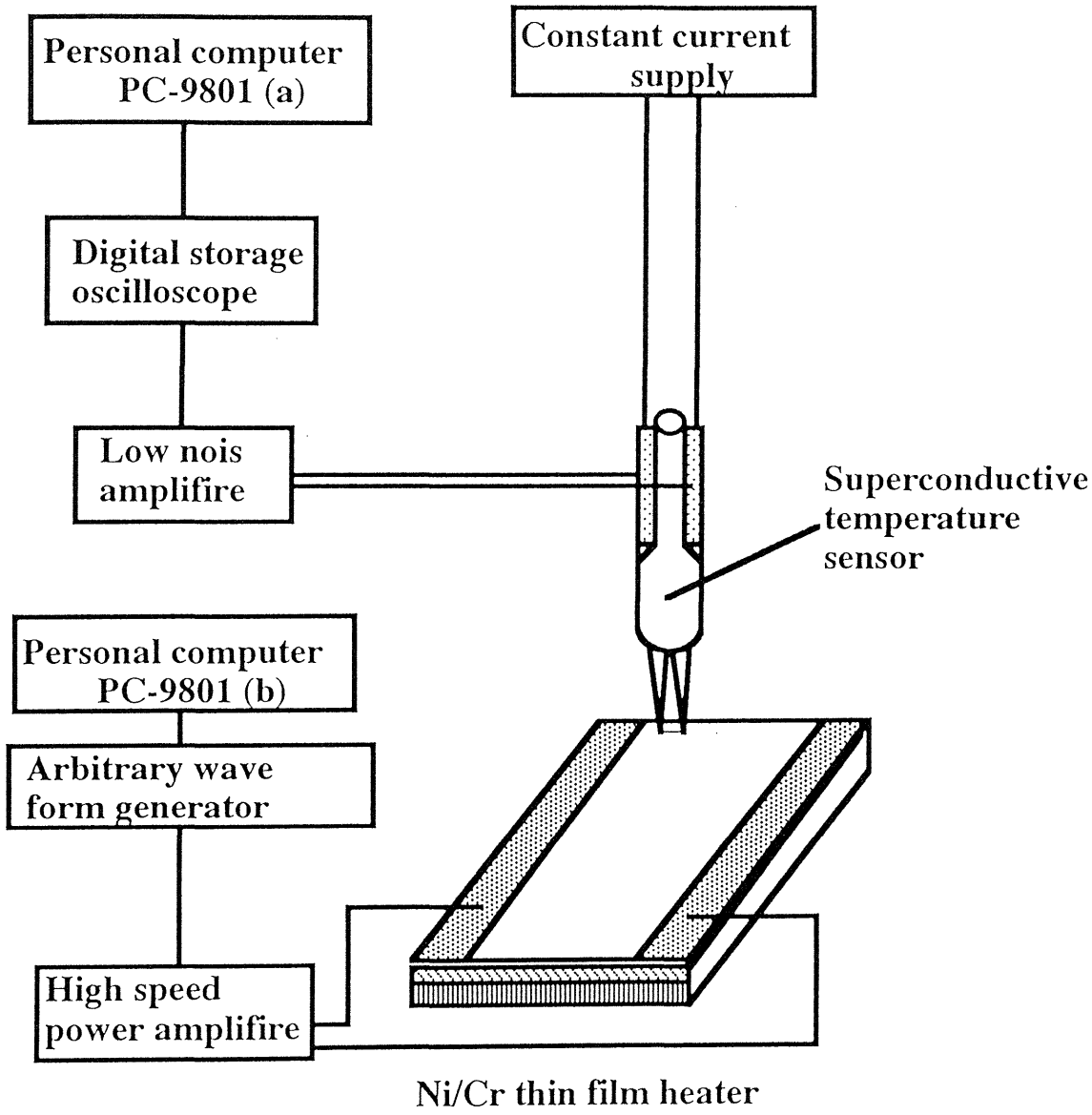

Figure 4.6 Block diagram of the whole experimental data acquisition system.

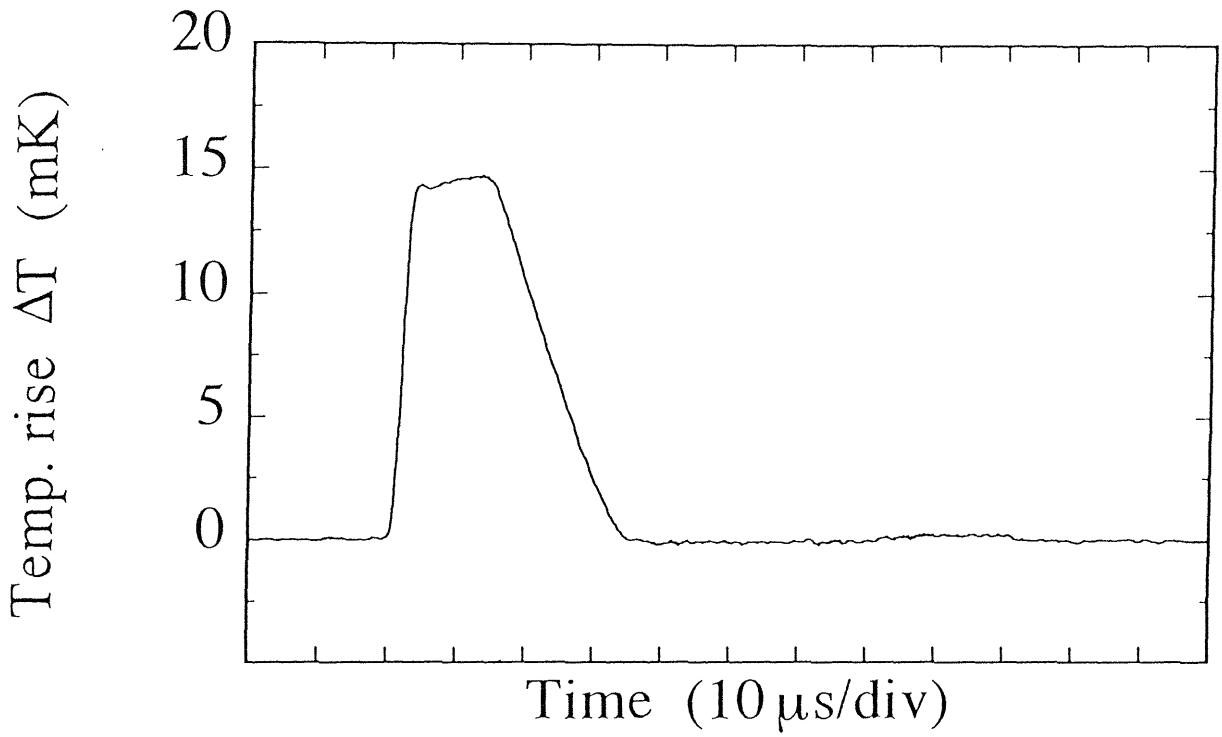

Figure 5.1 Measured frontal shock wave profile with a superconductive temperature sensor. This is the reproduction of the wave observed with a digital oscilloscope. $T_B = 1.70K$, $t_H = 30\mu s$, $q_p = 9W/cm^2$ and $z = 10mm$.

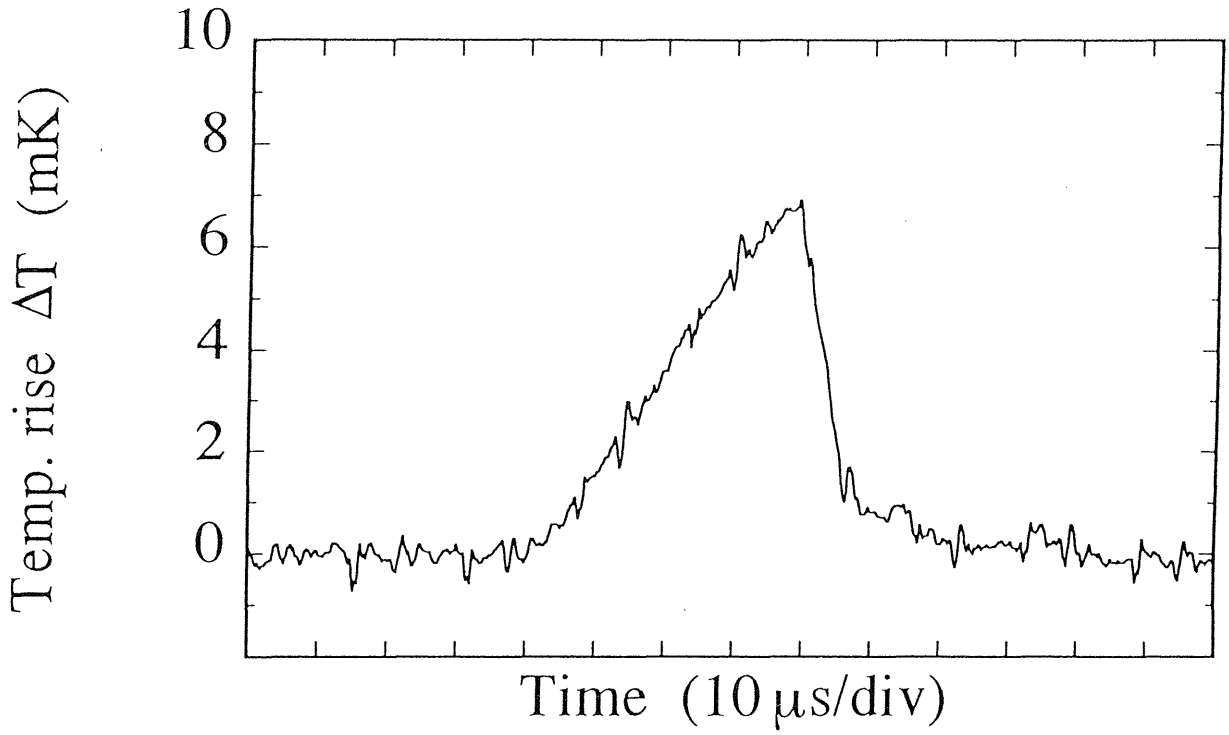

Figure 5.2 Measured back shock wave profile. $T_B = 2.05K$, $t_H = 30\mu s$, $q_p = 9W/cm^2$ and $z = 5mm$.

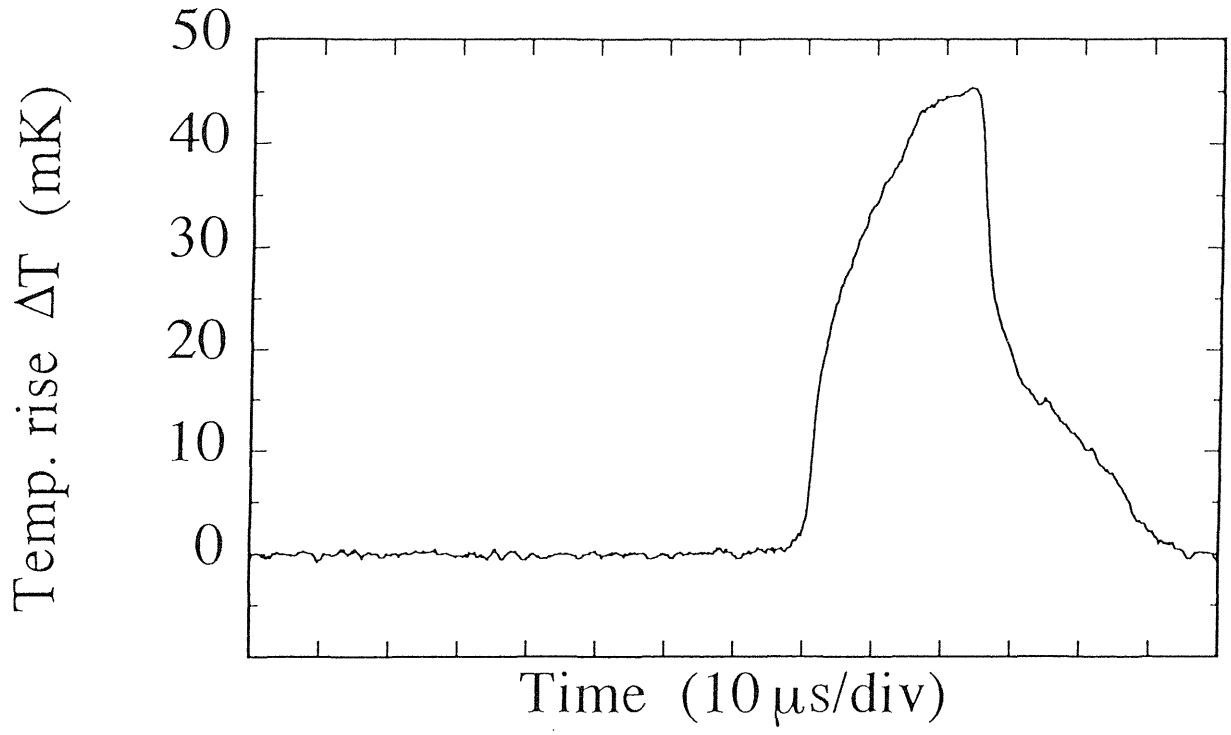

Figure 5.3 Measured double shock wave profile. $T_B = 1.86K$, $t_H = 30\mu s$, $q_p = 57W/cm^2$ and $z = 10mm$.

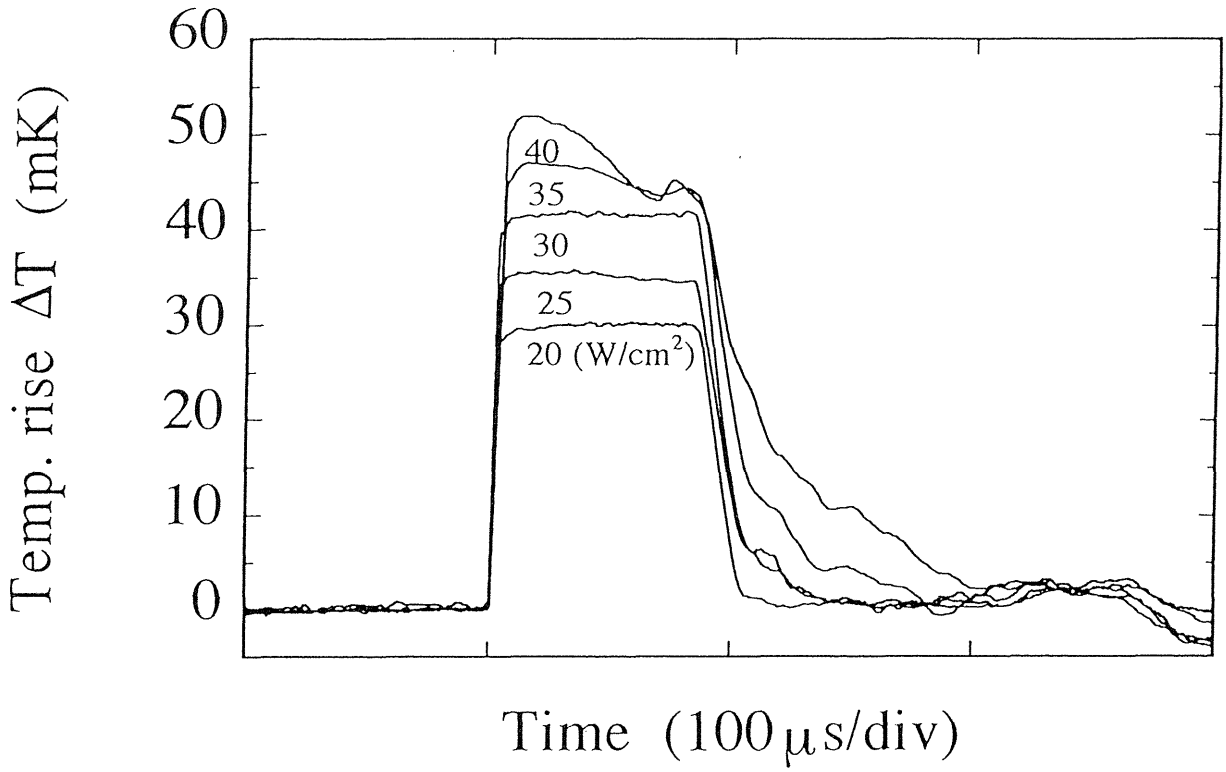

Figure 5.4 Multiple thermal shock wave profile generated by trapezoidal heat pulses of a number of values of the heat flux. The heat flux q_p are indicated beneath the each profile. All the profiles are superposed by synchronized at the wave front. $T_B = 1.69K$, $t_H = 100\mu s$, and $z = 5mm$.

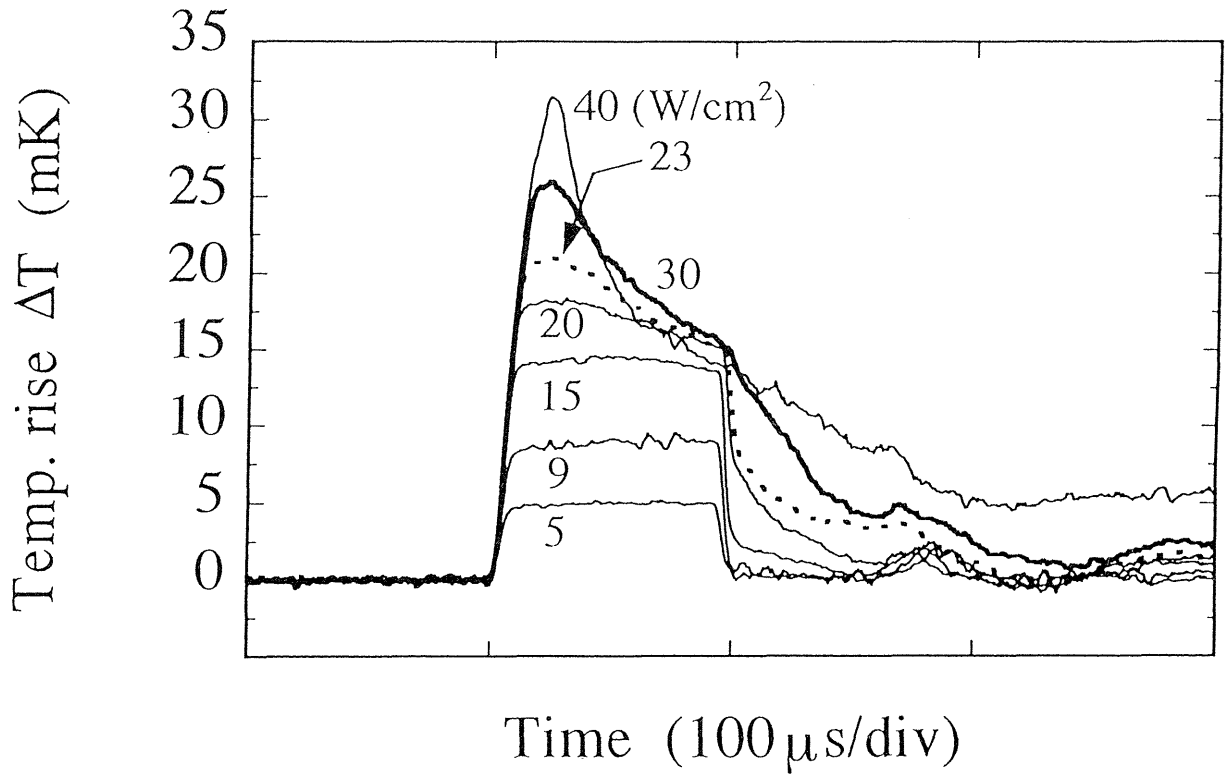

Figure 5.5 Multiple thermal shock wave profile generated by trapezoidal heat pulses of a number of values of the heat flux. $T_B = 1.90K$, $t_H = 100\mu s$, and $z = 10mm$.

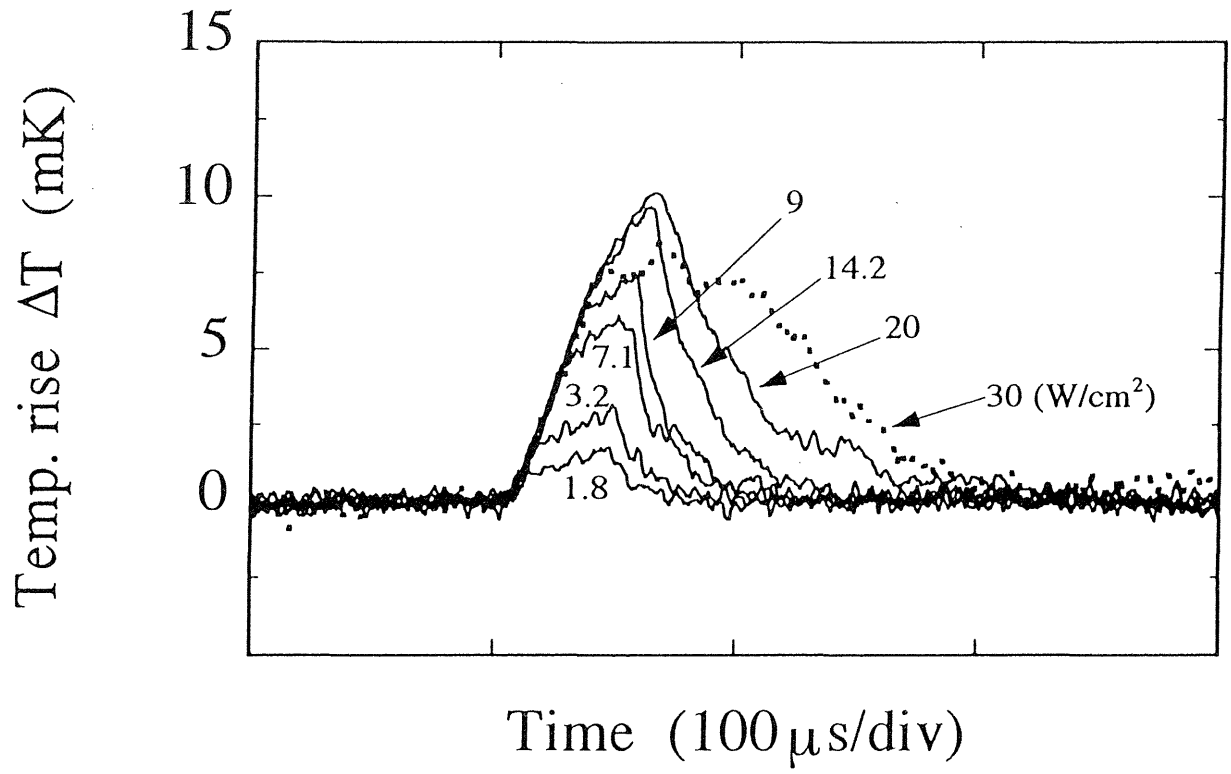

Figure 5.6 Multiple thermal shock wave profile generated by trapezoidal heat pulses of a number of values. $T_B = 2.10K$, $t_H = 50\mu s$, and $z = 2mm$.

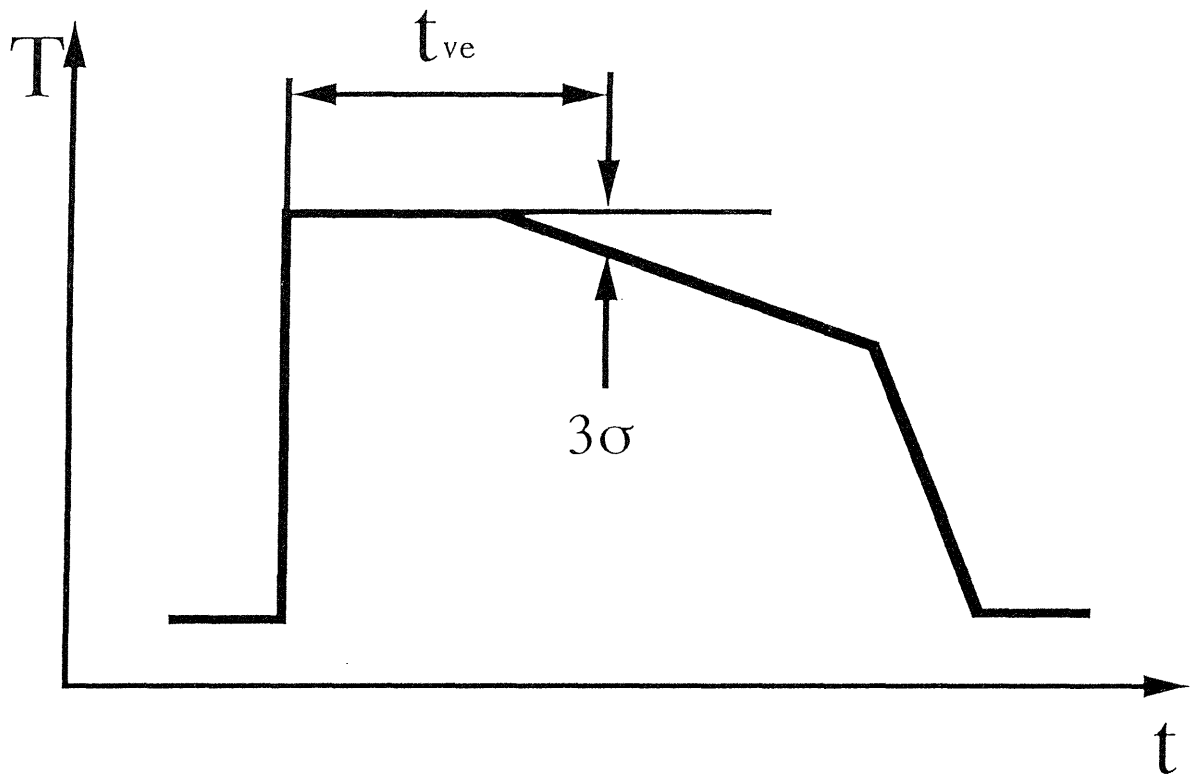

Figure 5.7 Schematical drawing of the definition of the characteristic time of quantized vortex development t_{ve}. σ is the standard deviation of the data fluctuation.

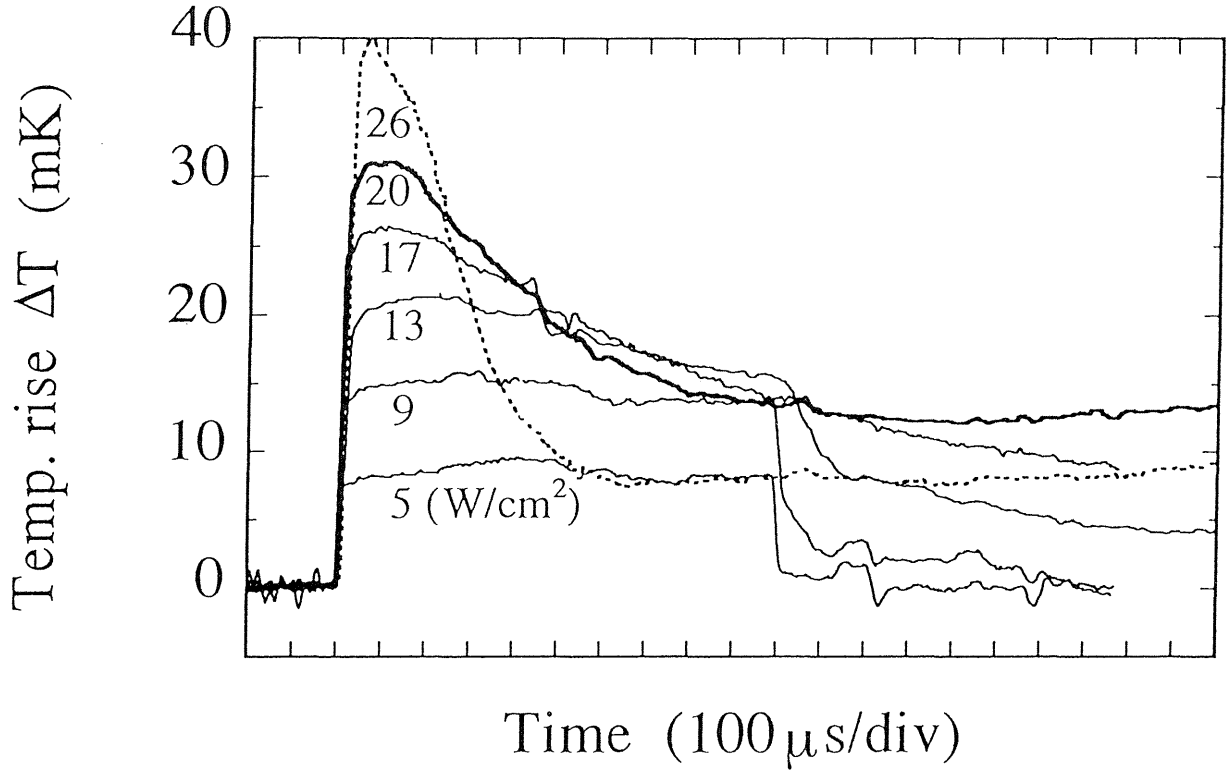

Figure 5.8 Superposed measured wave profiles generated by various heat fluxes as indicated in the figure. $T_B = 1.70K$, $t_H = 1000\mu s$ and $z = 10mm$.

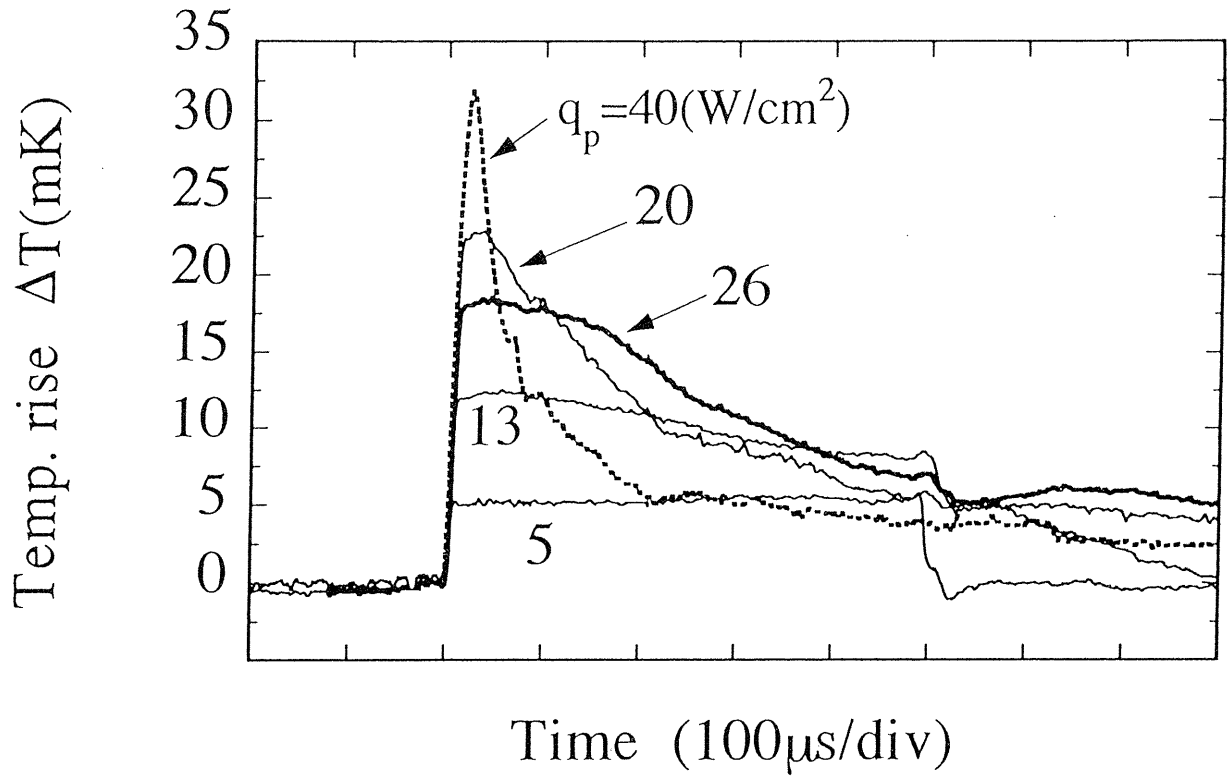

Figure 5.9 Superposed measured wave profiles. $T_B = 1.90K$, $t_H = 500\mu s$ and $z = 10mm$. q_p is varied from 5 to $40W/cm^2$.

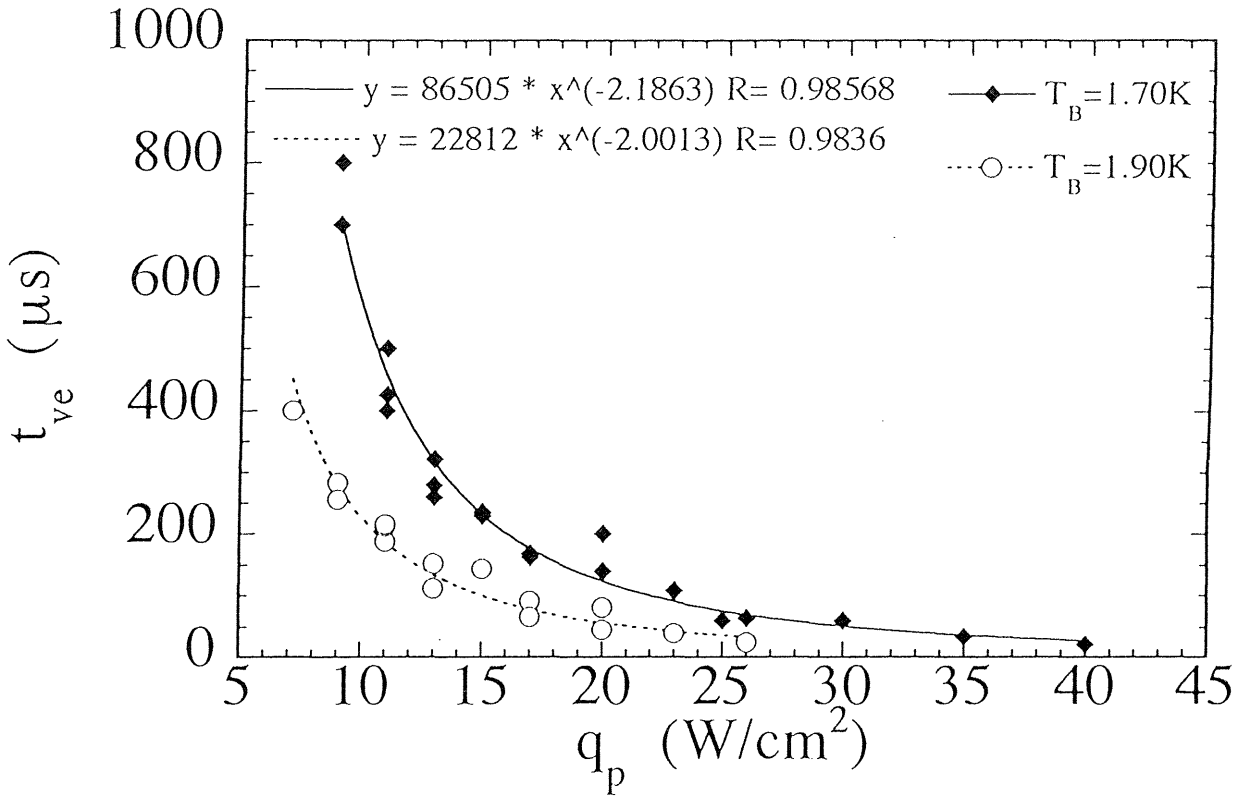

Figure 5.10 Variation of t_{ve} as a function of the applied heat flux q_p for two different temperature of 1.70 and 1.90K. Symbols represent the experimental data. Solid and broken lines represent the results of logarithmic regression. The equations of the regression are also shown.

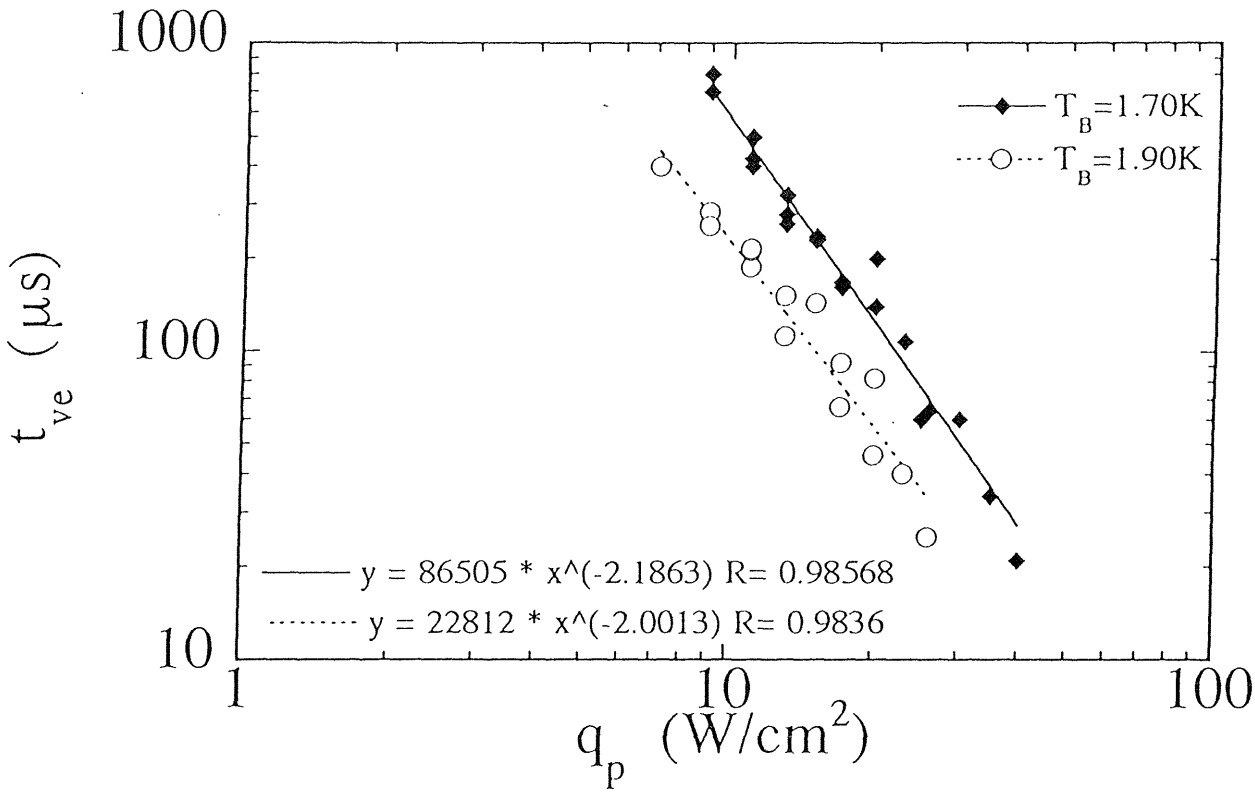

Figure 5.11 Double logarithmic plot of the data and the regression results in Fig. 5.10.

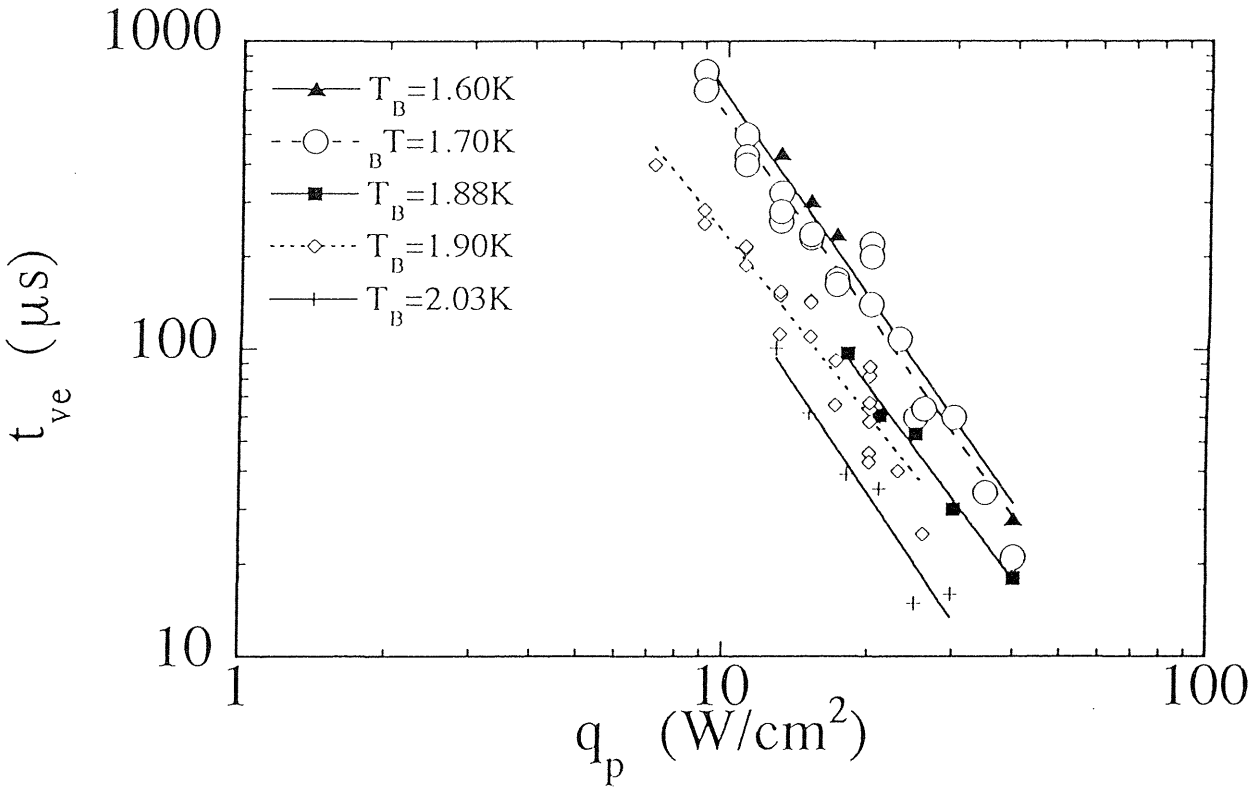

Figure 5.12 Variation of t_{ve} as a function of applied heat flux for various temperature between 1.60 and 2.03K. The lines are the linear regression results. Inclination of the all lines are approximately -2.

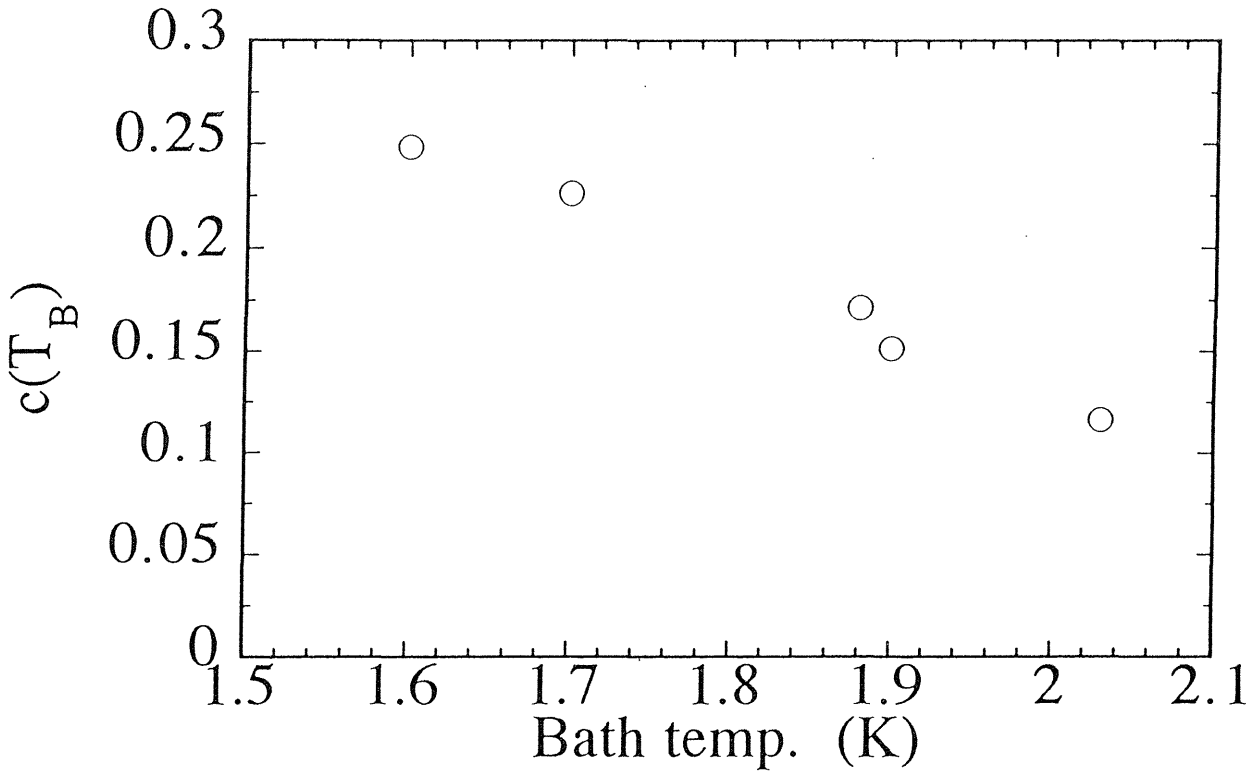

Figure 5.13 Measured variation of coefficient $c(T_B)$ with the temperature.

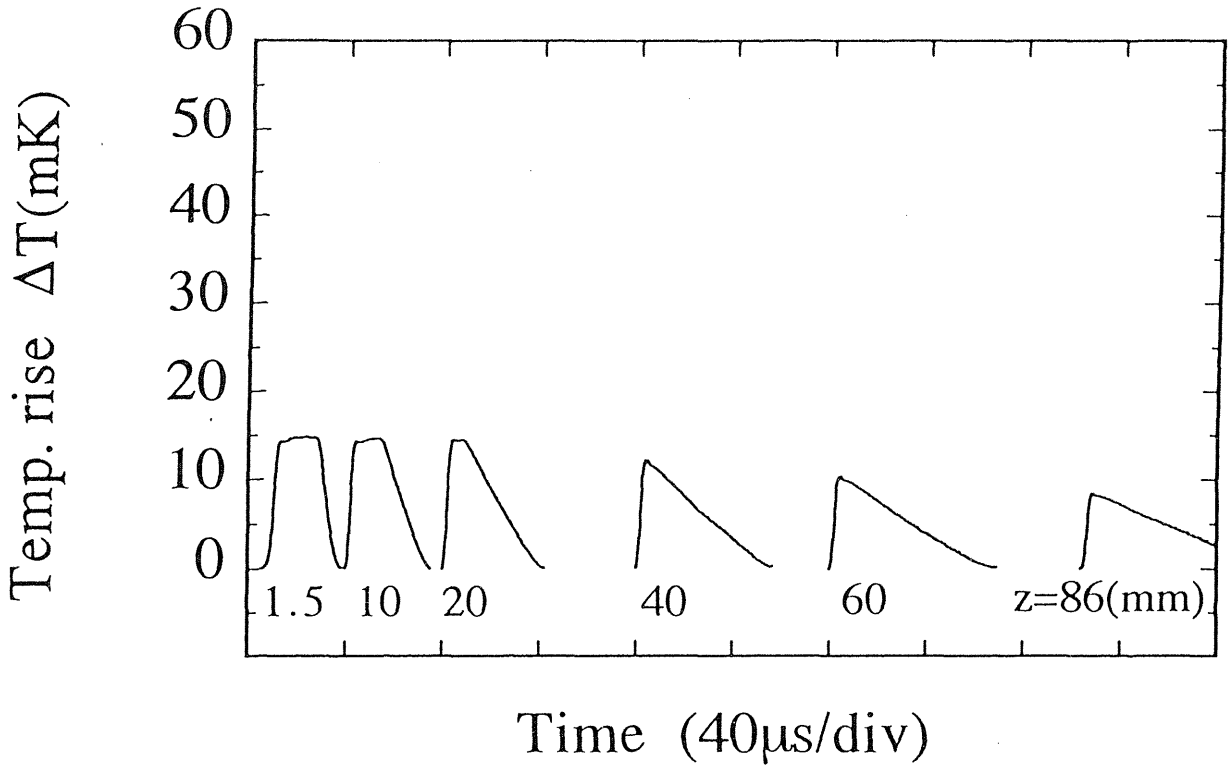

Figure 5.14 Wave form variation of a frontal shock wave during propagation. Each profile is measured with a temperature sensor fixed at a distance z, indicated beneath the form and is drawn at the corresponding location which is calculated by supposing that the full scale of the abscissa corresponds to $z = 100mm$. $T_B = 1.69K$, $t_H = 30\mu s$ and $q_p = 9W/cm^2$.

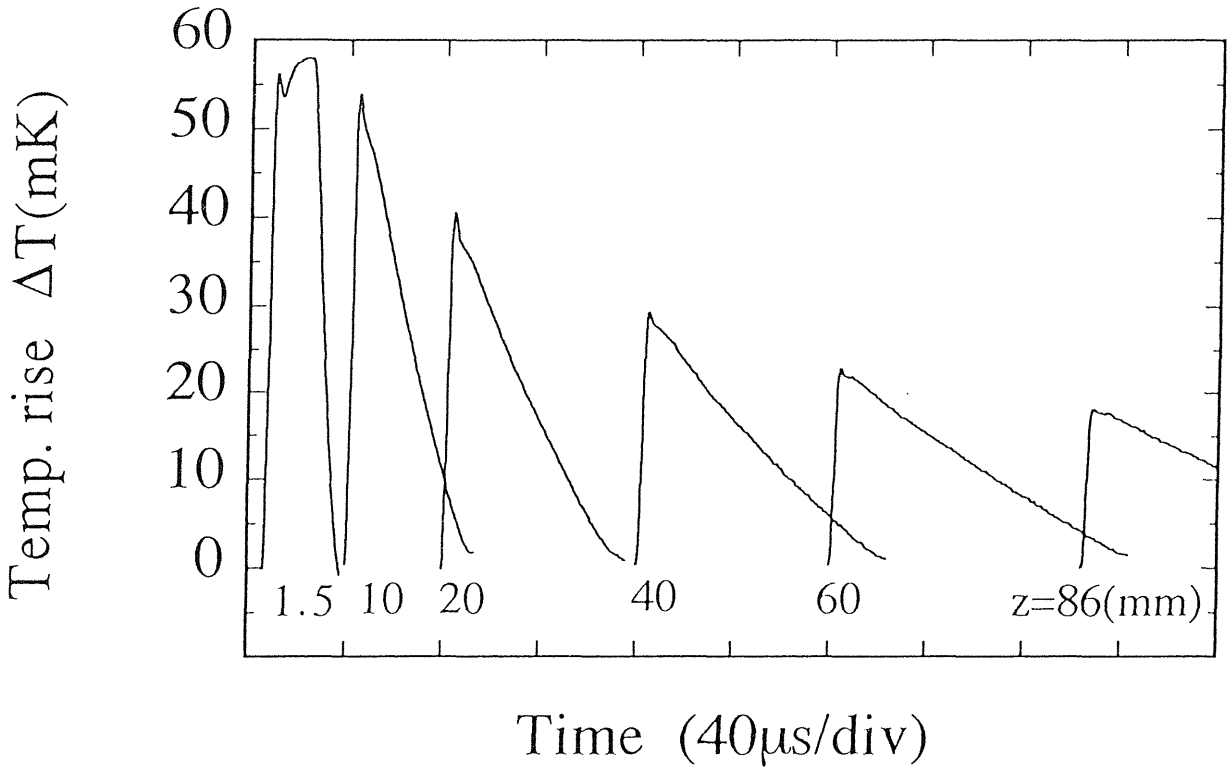

Figure 5.15 Typical wave form variation of a frontal shock wave during propagation. $T_B = 1.69K$, $t_H = 30\mu s$ and $q_p = 40W/cm^2$.

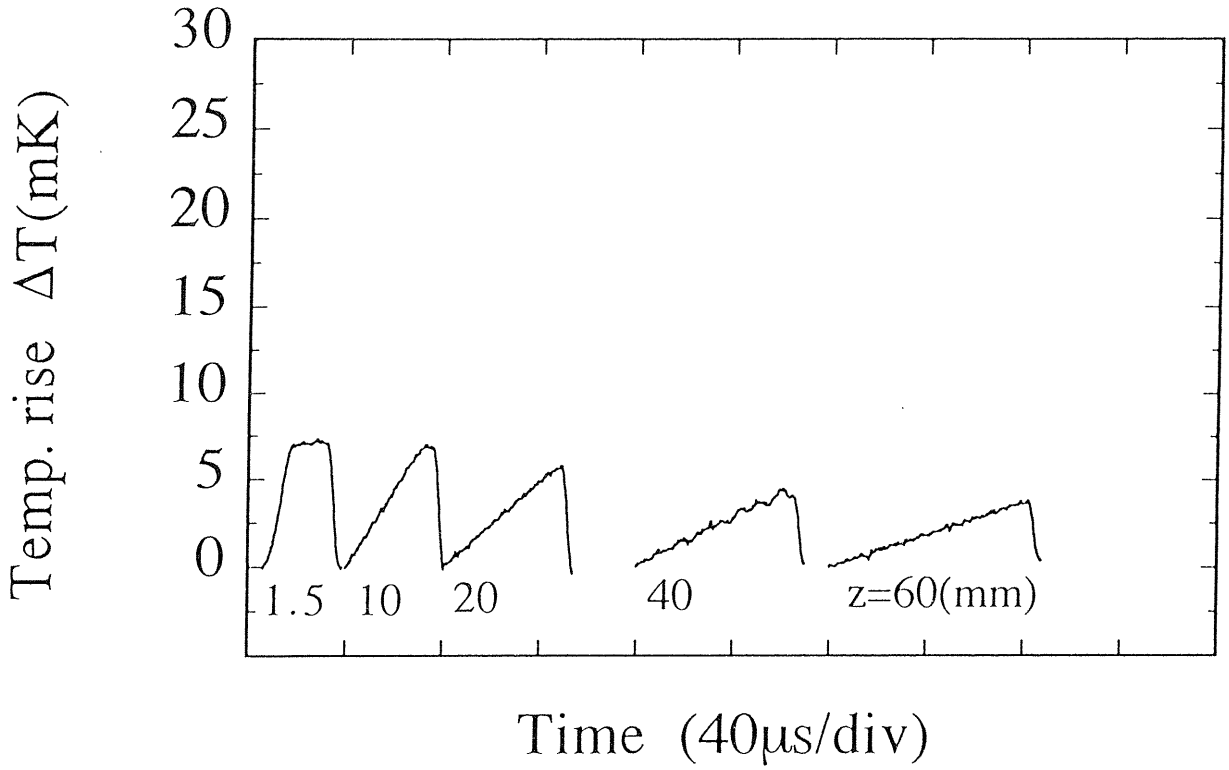

Figure 5.16 Typical wave form variation of a back shock wave during propagation. $T_B = 2.05K$, $t_H = 30\mu s$ and $q_p = 9W/cm^2$.

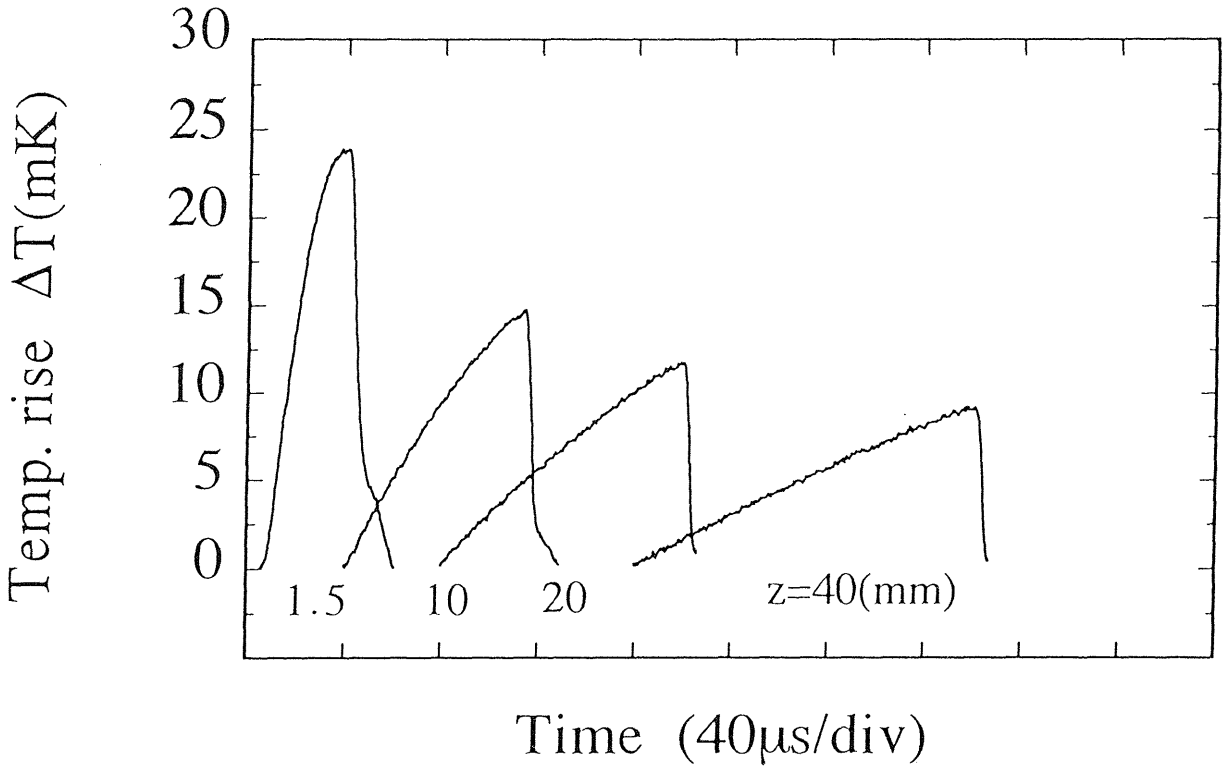

Figure 5.17 Typical wave form variation of a back shock wave during propagation. $T_B = 2.05K$, $t_H = 30\mu s$ and $q_p = 40W/cm^2$.

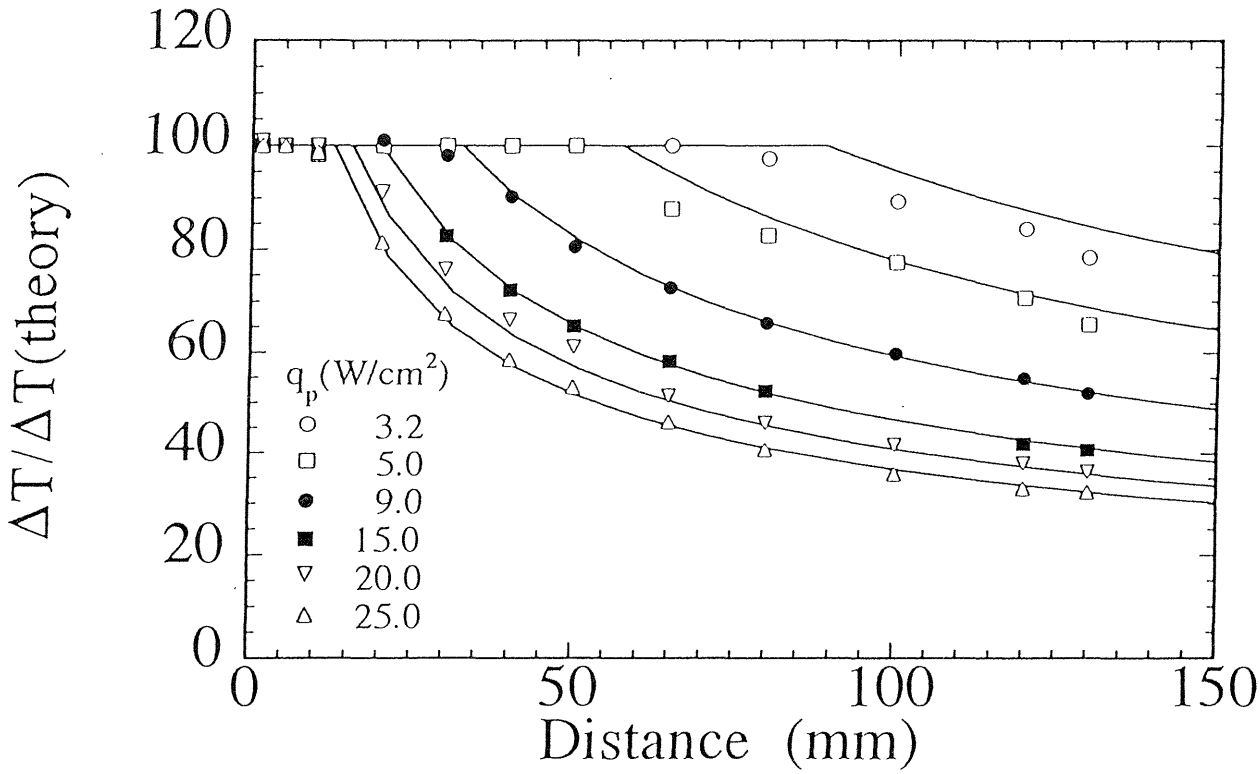

Figure 5.18 Wave height variation of a frontal shock wave during propagation. Wave height is normalized by the theoretical height at $z = 0mm$. Experimental data are represented by symbols and the theoretical predictions given by the equal area rule are indicated by solid lines. $T_B = 1.70K$ and $t_H = 30\mu s$.

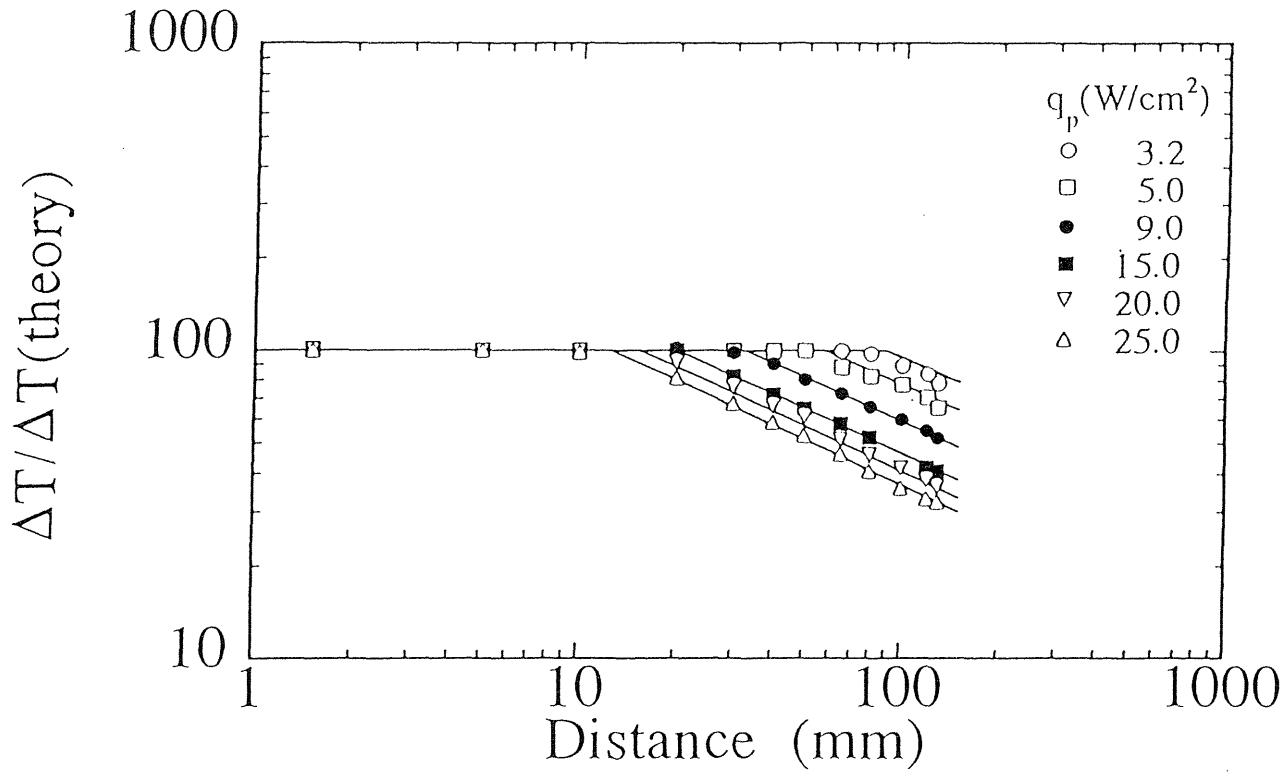

Figure 5.19 Double logarithmic plot of Fig. 5.18.

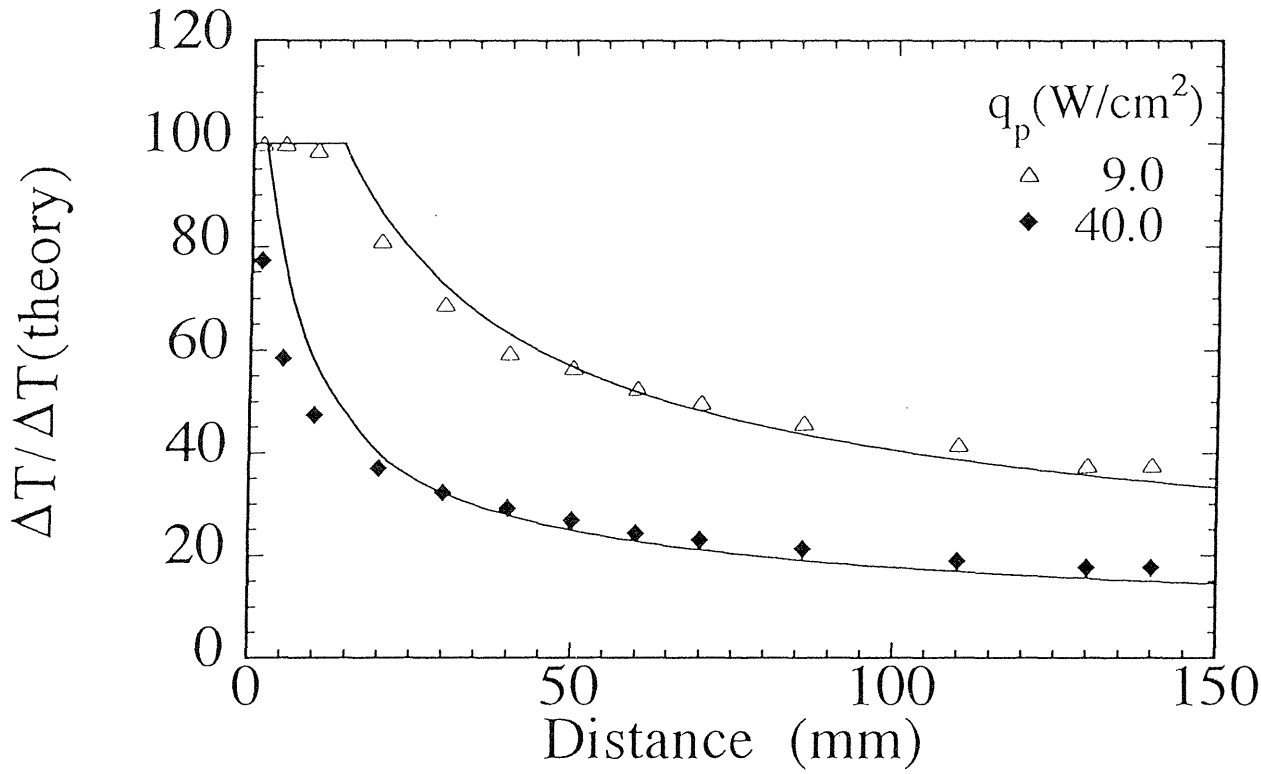

Figure 5.20 Wave height variation of a back shock wave during propagation. Wave height is normalized by the theoretical height at $z = 0mm$. Experimental data are represented by symbols and the theoretical predictions given by the equal area rule are indicated by solid lines. $T_B = 2.05K$ and $t_{II} = 30\mu s$.

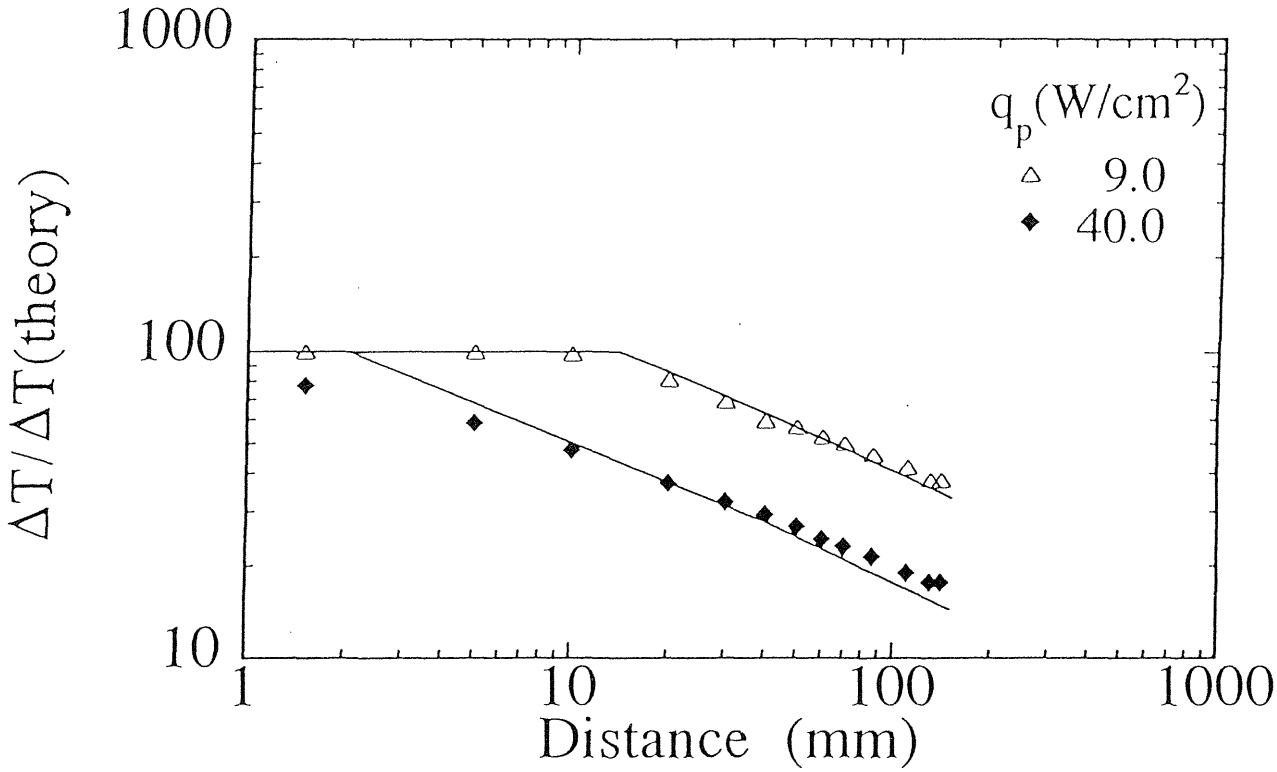

Figure 5.21 Double logarithmic plot of Fig. 5.20.

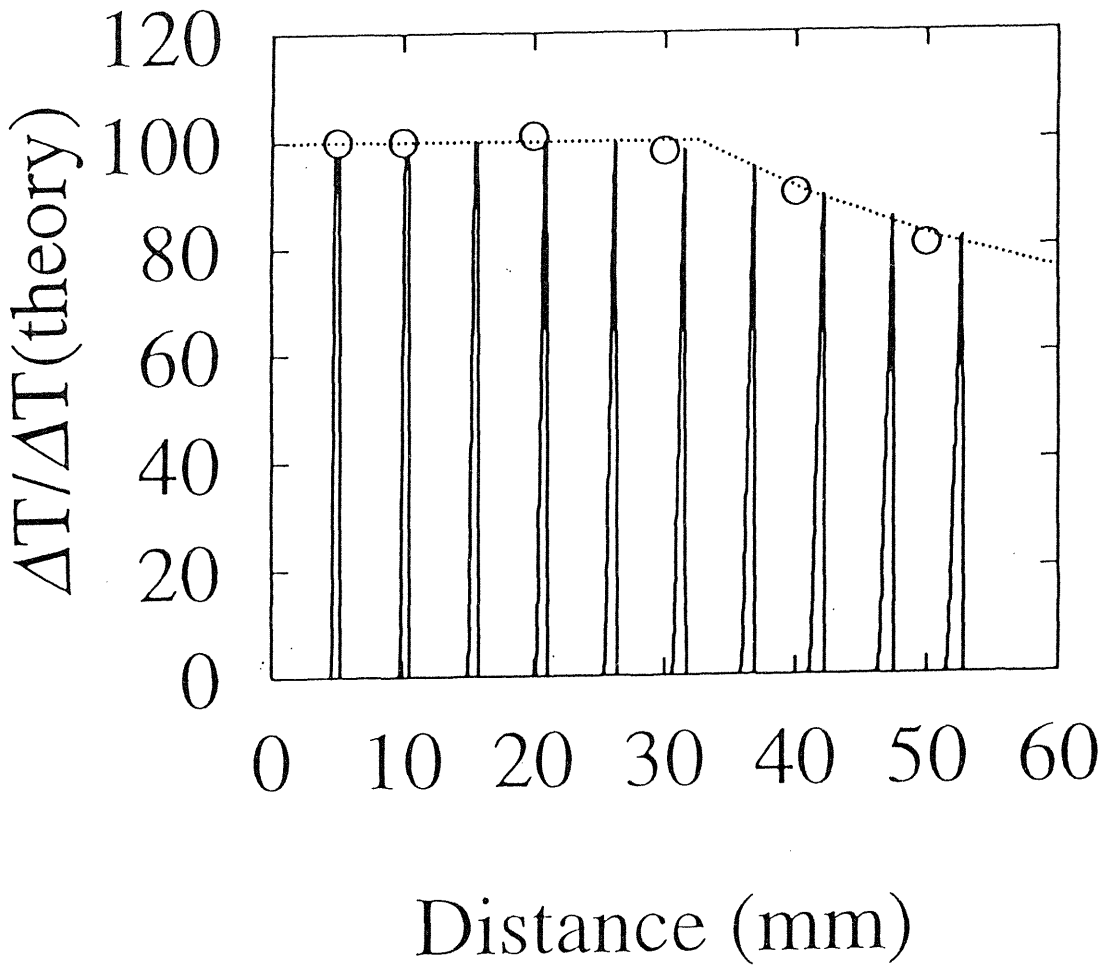

Figure 5.22 Comparison among the experimental data, the numerical result[24] and the analytical solution on the basis of the equal area rule in the case of the influence of quantized vortex lines is negligible. The open circle represents the experimental data. The wave profile obtained by solving the two-fluid equations are drawn by solid line. The broken line represents the theoretical prediction obtained on the basis of the equal area rule, respectively. $T_B = 1.70K$, $t_H = 30\mu s$ and $q_p = 9W/cm^2$.

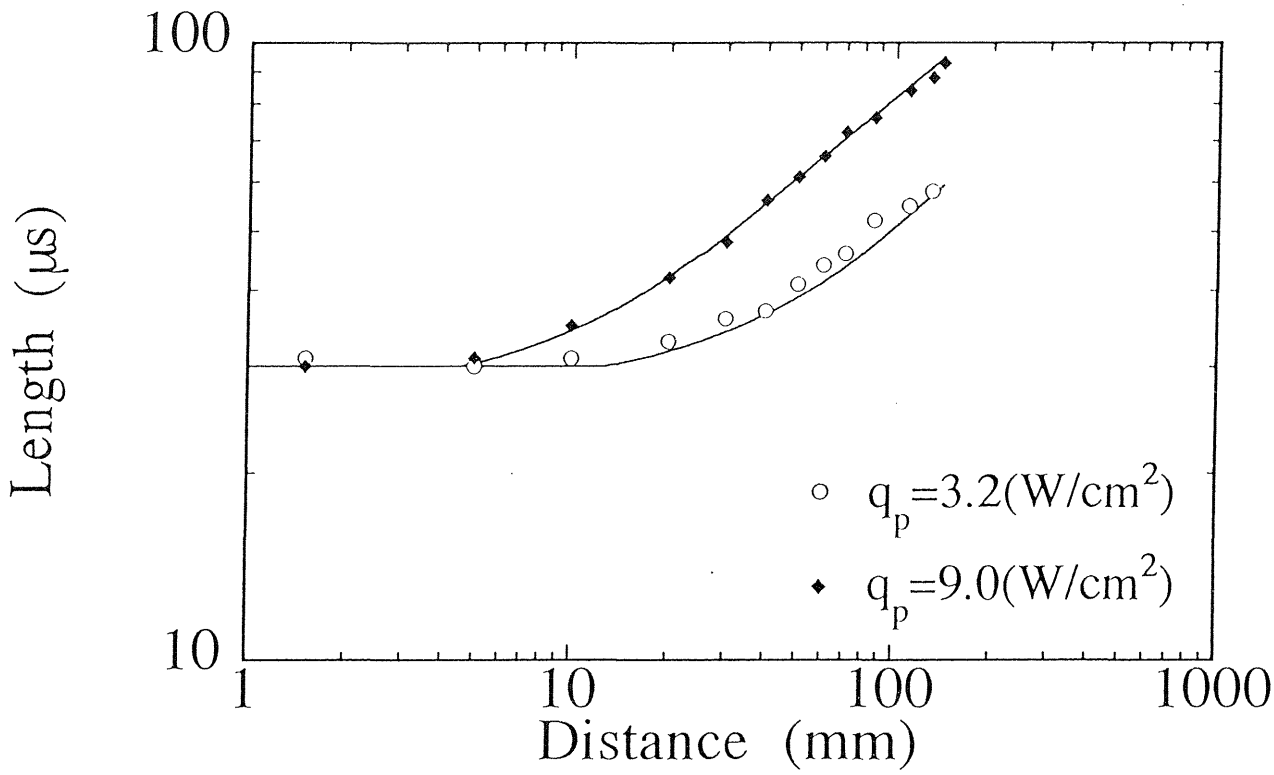

Figure 5.23 Variation of the length of a frontal shock wave during propagation. Experimental data for two heat flux $q_p = 3.2$ and $9.0 W/cm^2$ are plotted. The solid lines represent the theoretical predictions. The length of the wave observed with a digital oscilloscope has the dimension of time. Initial length of the wave t_H is $30 \mu s$. $T_B = 1.70 K$.

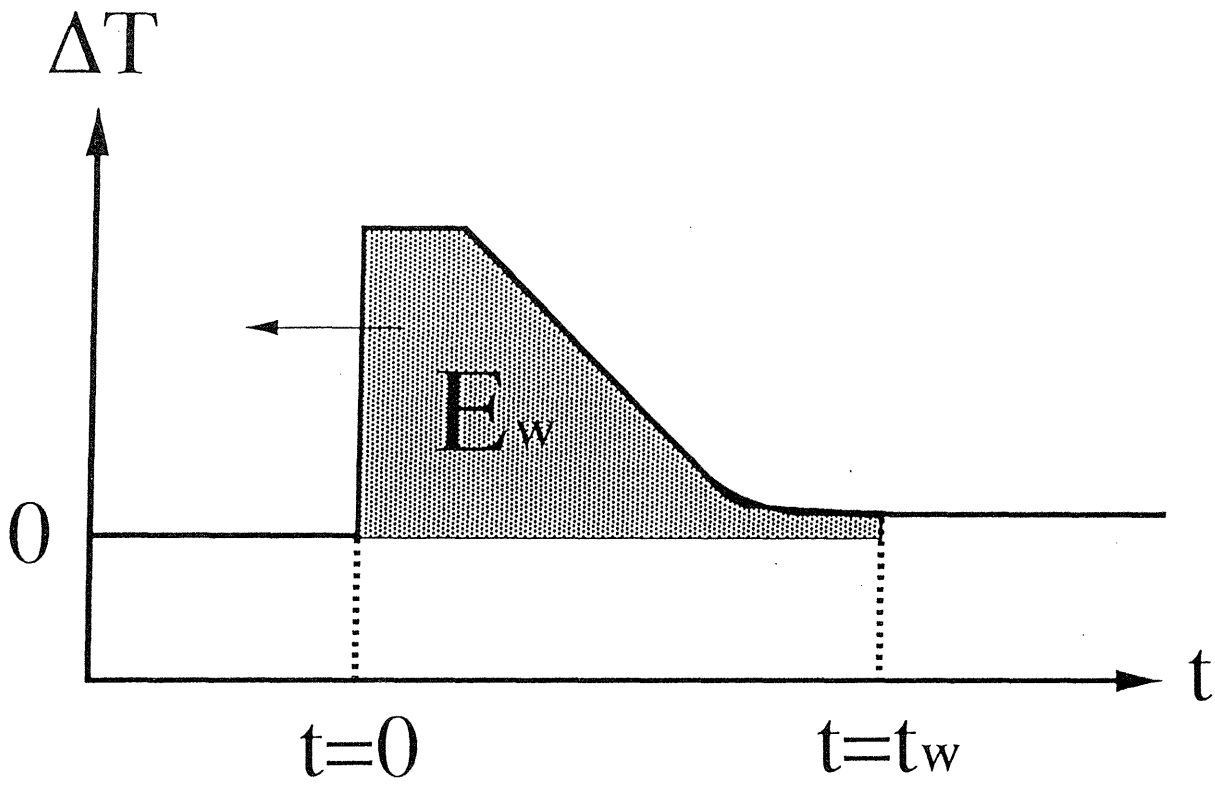

Figure 5.24 Definition of the amount of heat transported by a second sound wave mode through unit area E_w . The integration is carried out from wave front ($t = 0$) to the twice half value with of the profile ($t = t_w$).

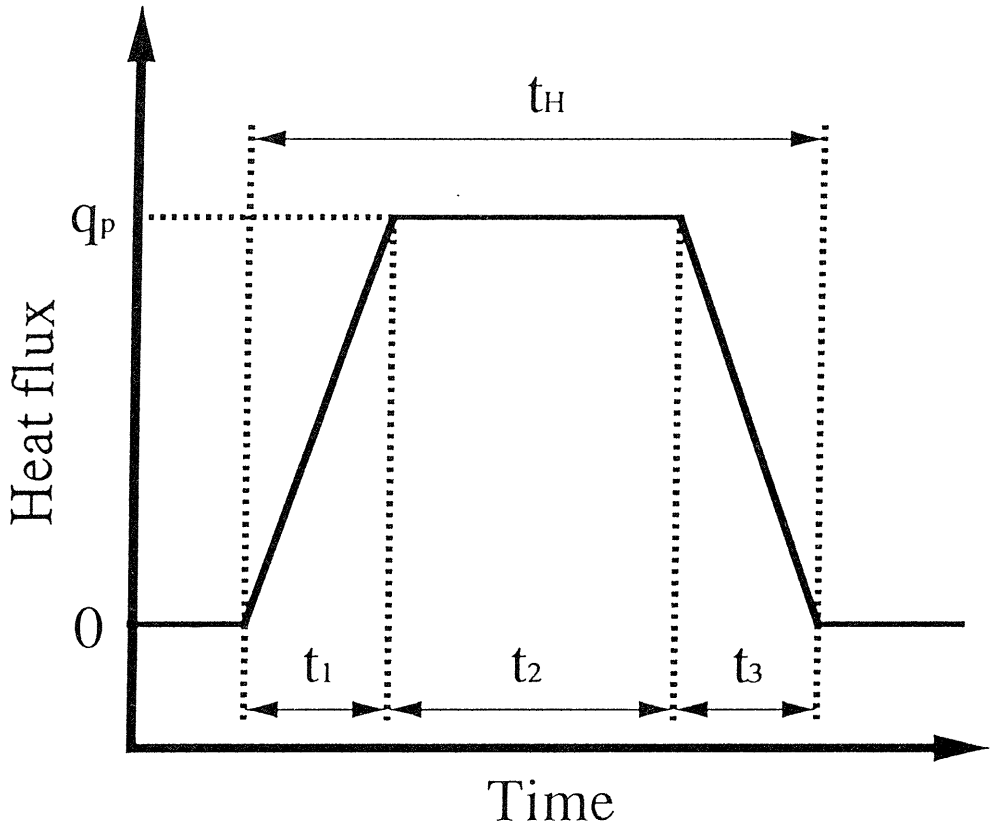

Figure 5.25 Schematical drawing of the trapezoidal heat pulse form fed from a heater.

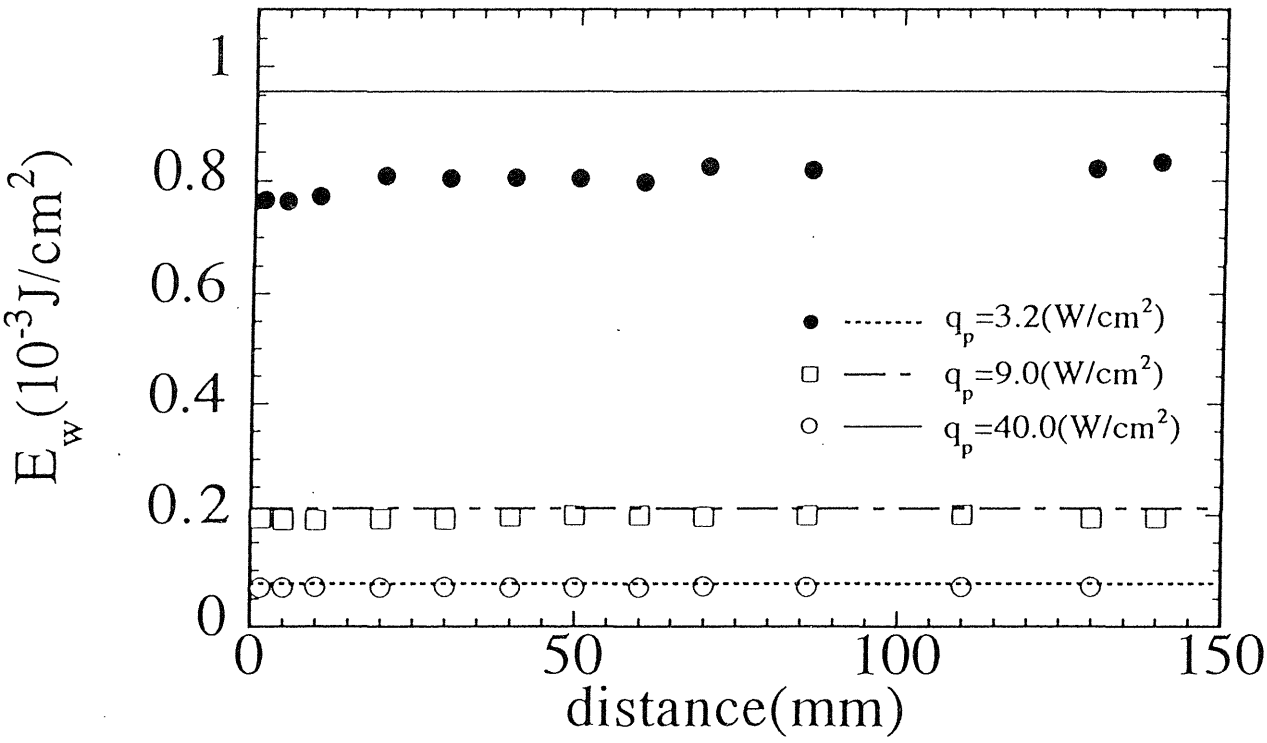

Figure 5.26 Variation of the amount of heat transported by a thermal shock wave through propagation. Symbols and lines represent the experimental data and the total amount of heat fed from a heater, respectively. $T_B = 1.70K$, $t_H = 30\mu s$.

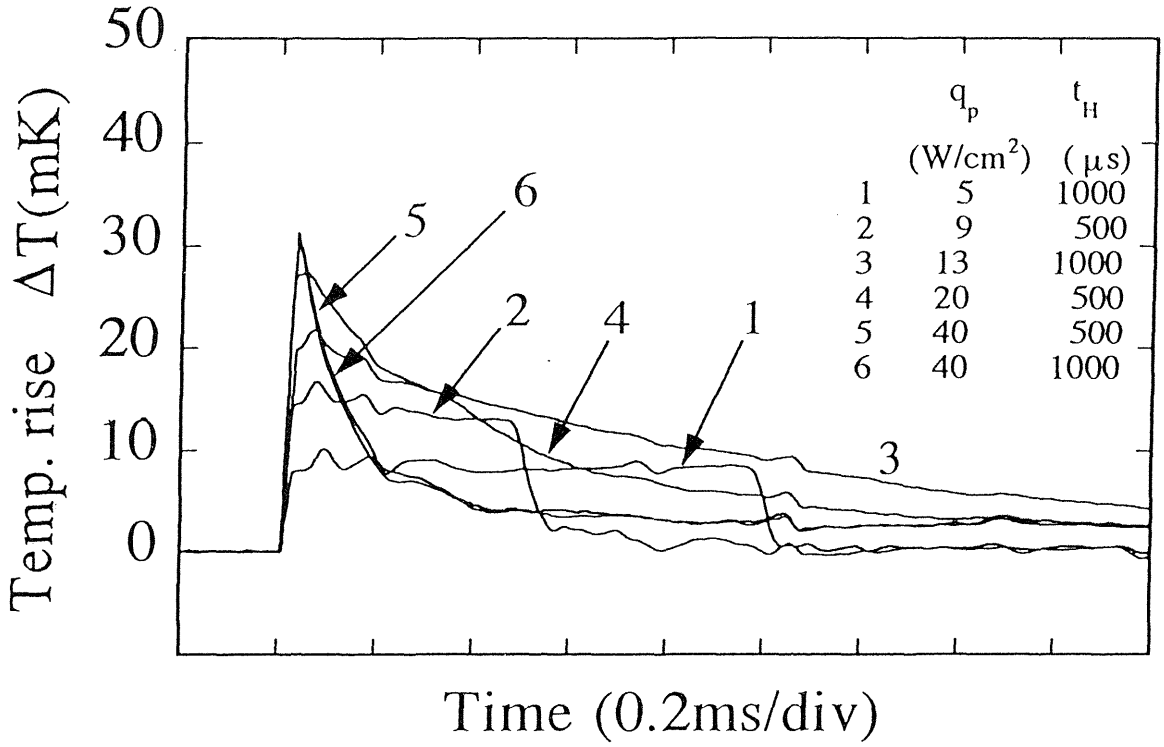

Figure 5.27 Superposed wave profiles generated under various initial heating conditions of q_p and t_H as indicated in the figure. $T_B = 1.70K$ $z = 30mm$.

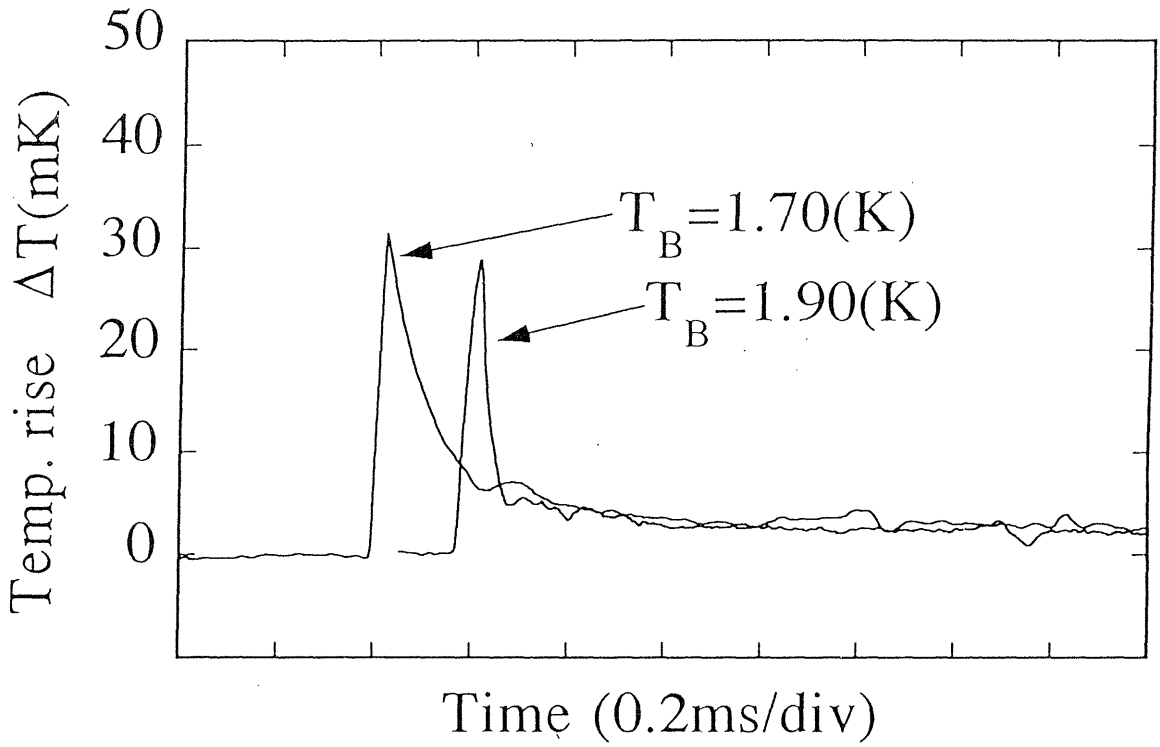

Figure 5.28 Examples of limiting profile at $T_B = 1.70K$ and $1.90K$. Both onset time of heating are synchronized in the figure. $t_H = 1000\mu s$ and $q_p = 40W/cm^2$ in both cases. $z = 30mm$.

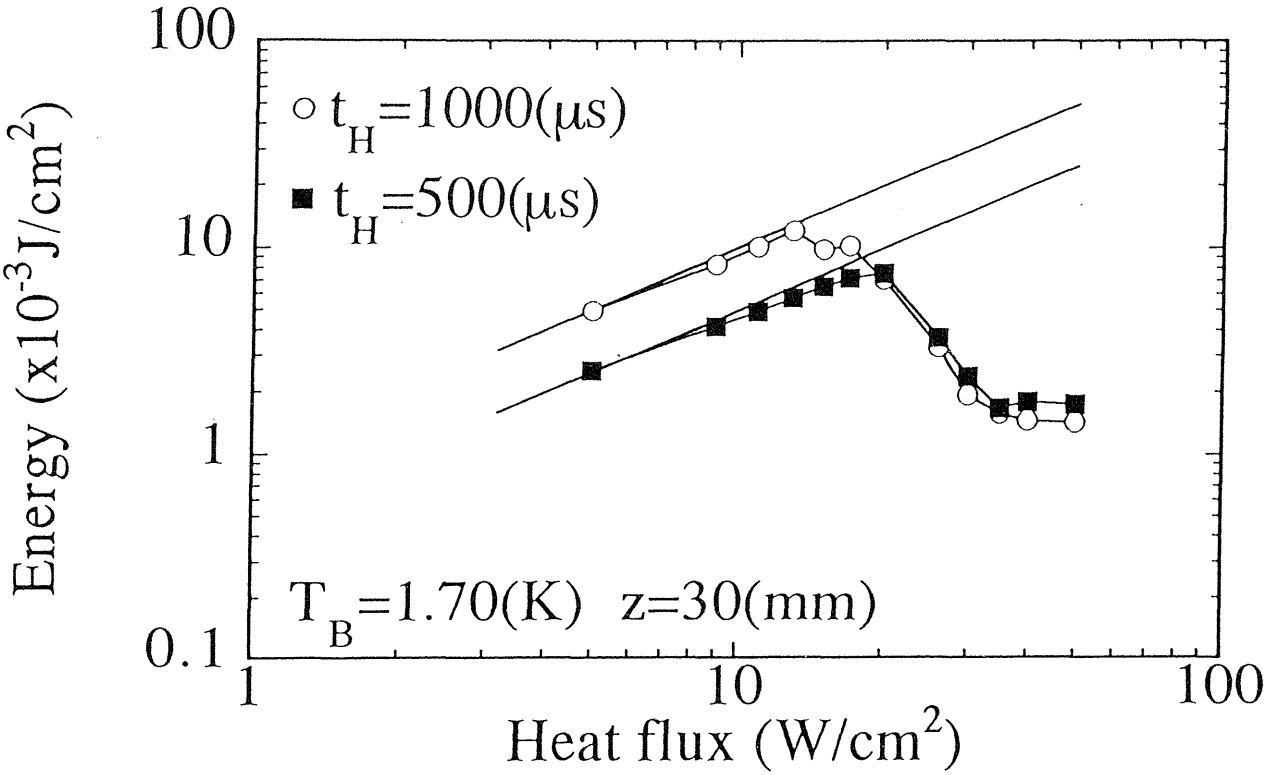

Figure 5.29 Amount of heat per unit area transported in the second sound wave mode. Experimental data obtained for two different heating time are plotted. Solid lines represent the total amount of heat fed from a heater. $T_B = 1.70K$ and $z = 30mm$.

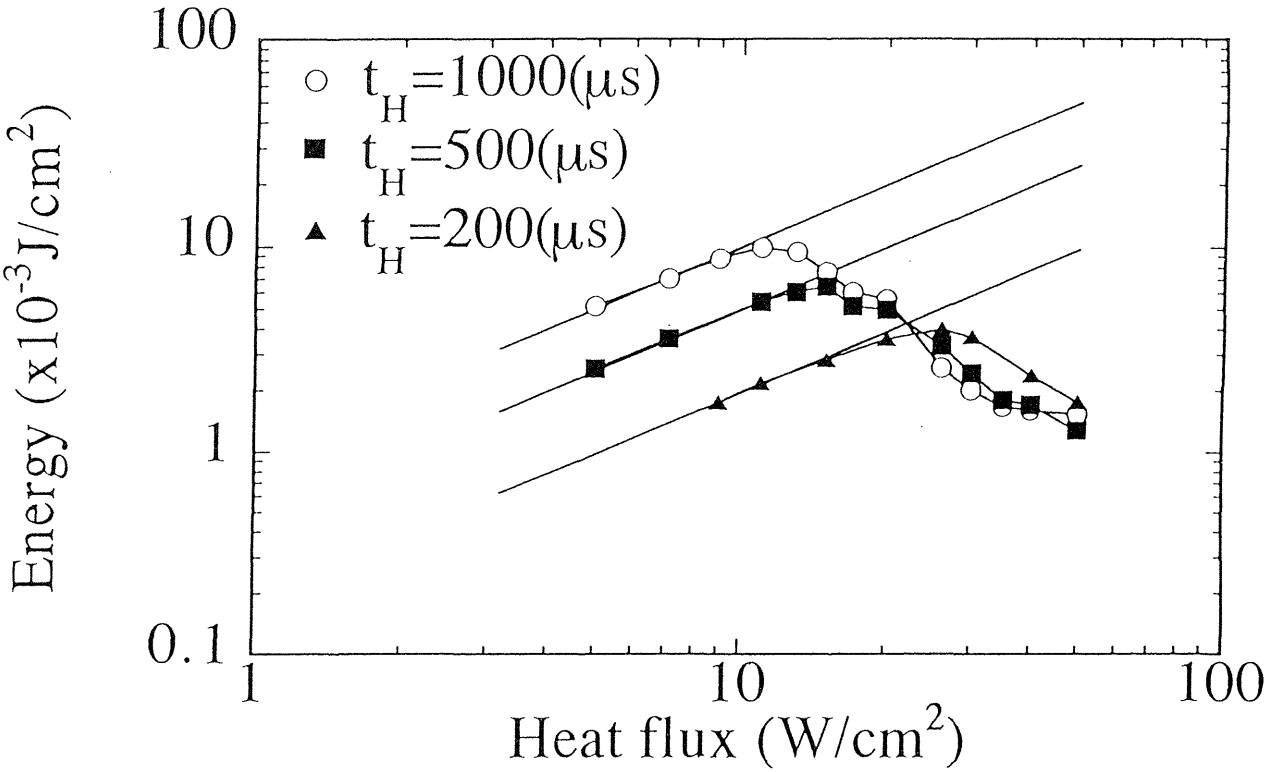

Figure 5.30 Amount of heat per unit area transported in the second sound wave mode. Experimental data obtained for three different heating time are plotted. Solid lines represent the total amount of heat fed from a heater. $T_B = 1.95K$ and $z = 30mm$.

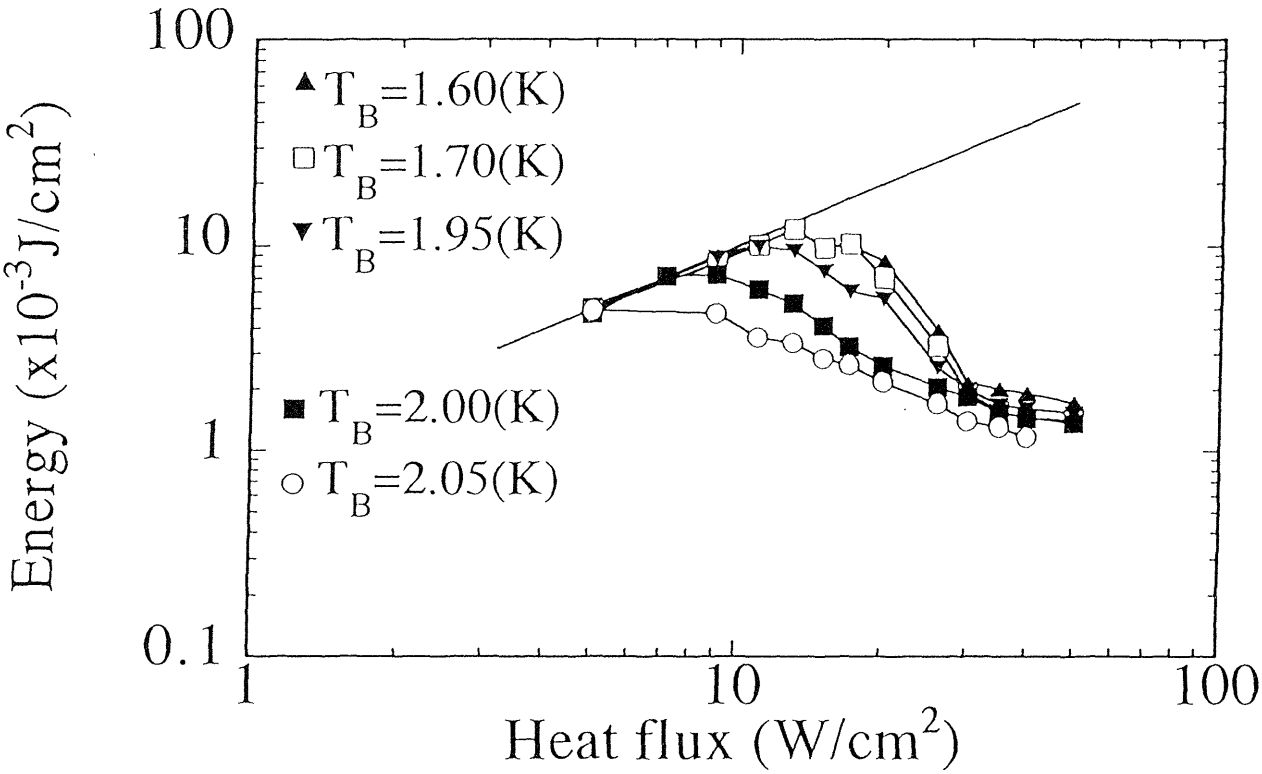

Figure 5.31 Temperature dependence of the amount of heat per unit area transported in the second sound wave mode. Temperature is varied between 1.60 and 2.05K. Heating time is fixed at $t_H = 1000\mu s$. $z = 30mm$.

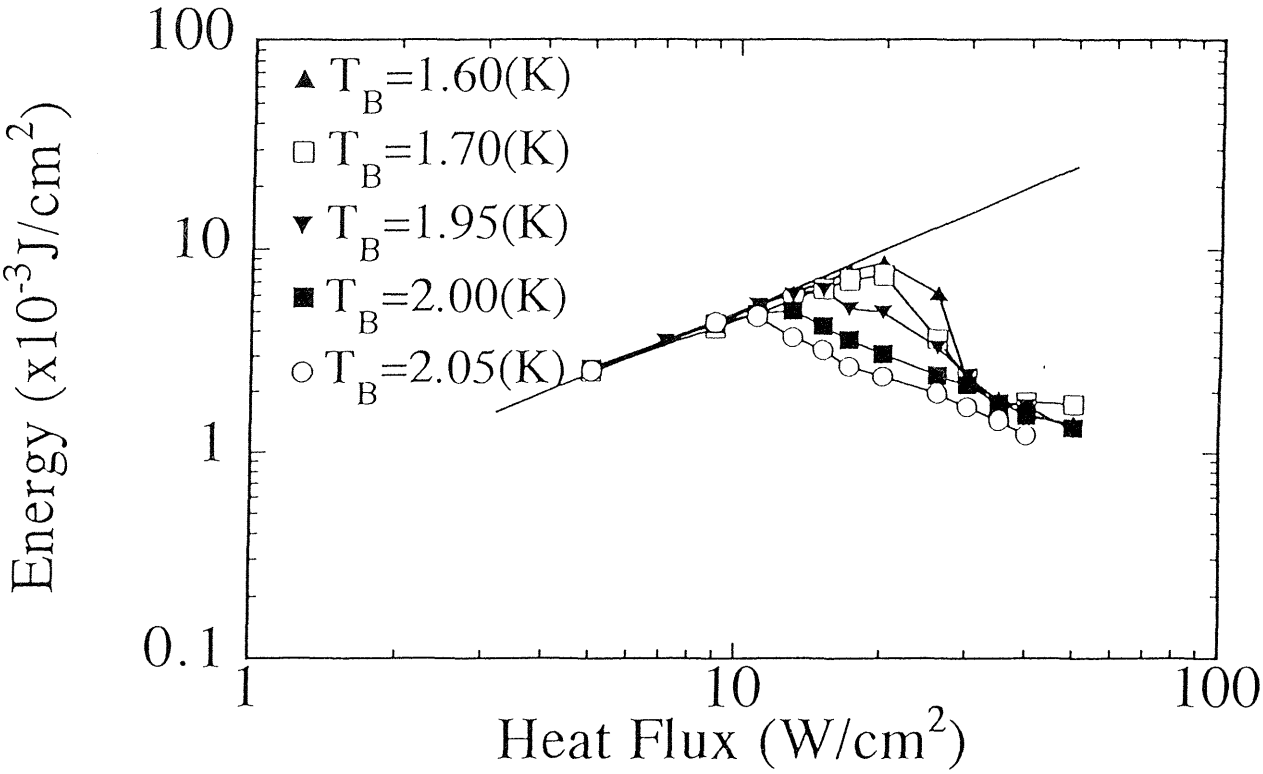

Figure 5.32 Temperature dependence of the amount of heat per unit area transported in the second sound wave mode. Temperature is varied between 1.60 and 2.05K. Heating time is fixed at $t_H = 500\mu s$. $z = 30mm$.

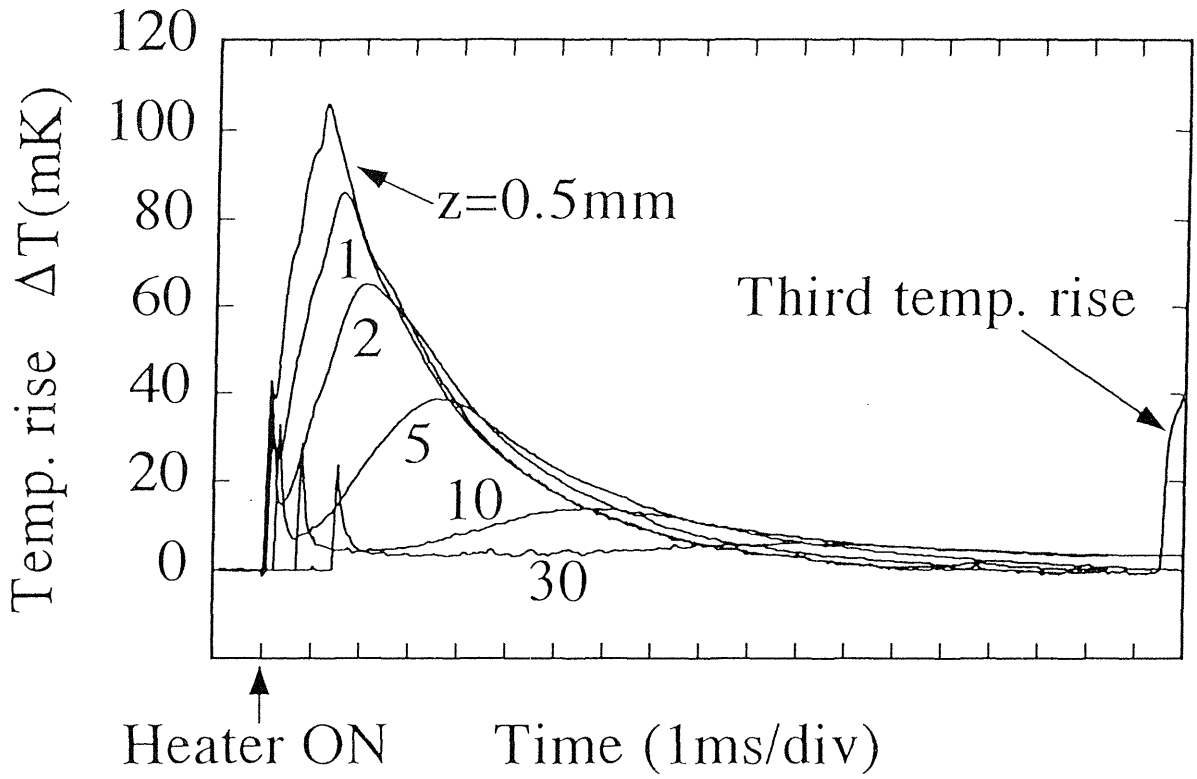

Figure 5.33 Superposed transient temperature traces measured at various location of a temperature sensor. The sensor location ranges from $z = 0.5$ to $30mm$. The onset of heating is marked by "Heater ON" on the abscissa. $T_B = 1.70K$, $t_H = 1000\mu s$ and $q_p = 40W/cm^2$. The third temperature rise which is the signal of the onset of the boiling near the heater is detected with the sensor fixed at $z = 0.5mm$.

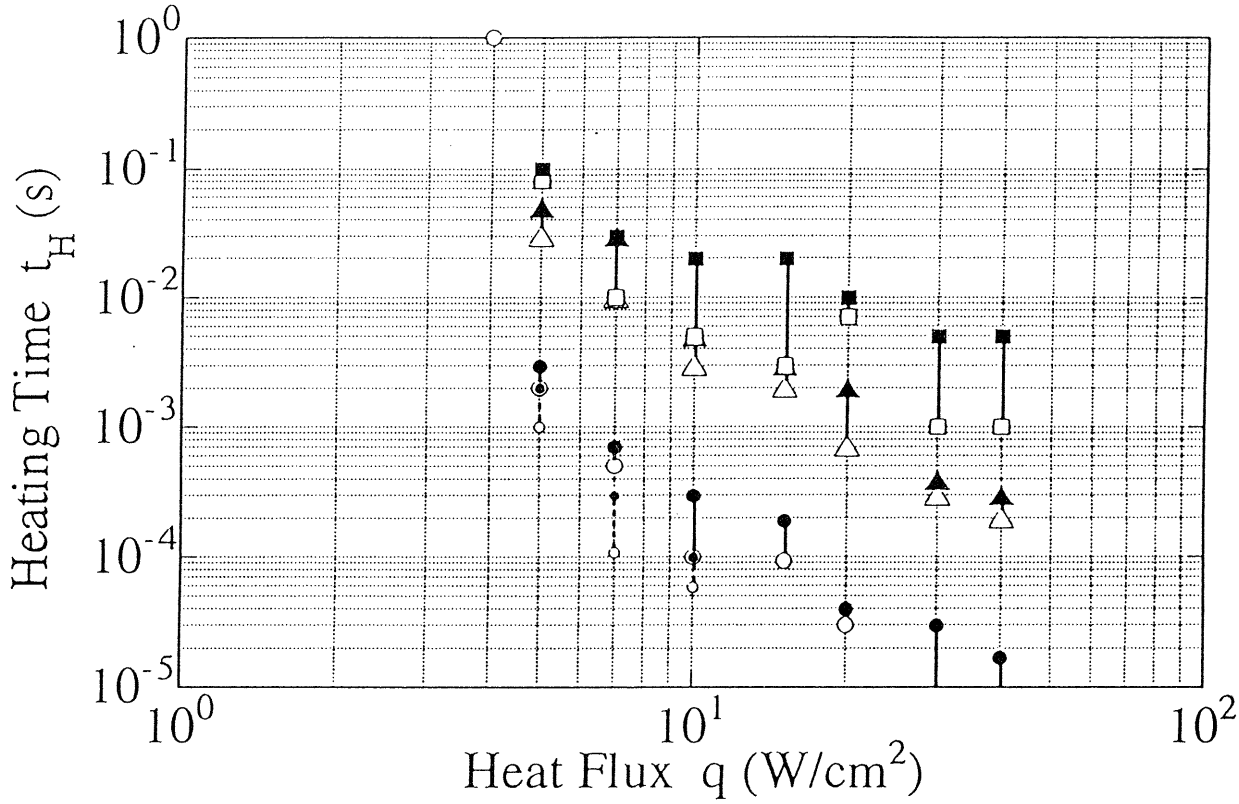

Figure 5.34 Onset time of the spotwise transient nucleate boiling (○—●), the film boiling (△—▲) and the noisy film boiling (□—■) at $T_B = 1.80K$ The laud acoustic noise caused during noisy boiling. The occurrence of it also depends on the temperature and the hydrostatic pressure. (This figure is cited from [26])

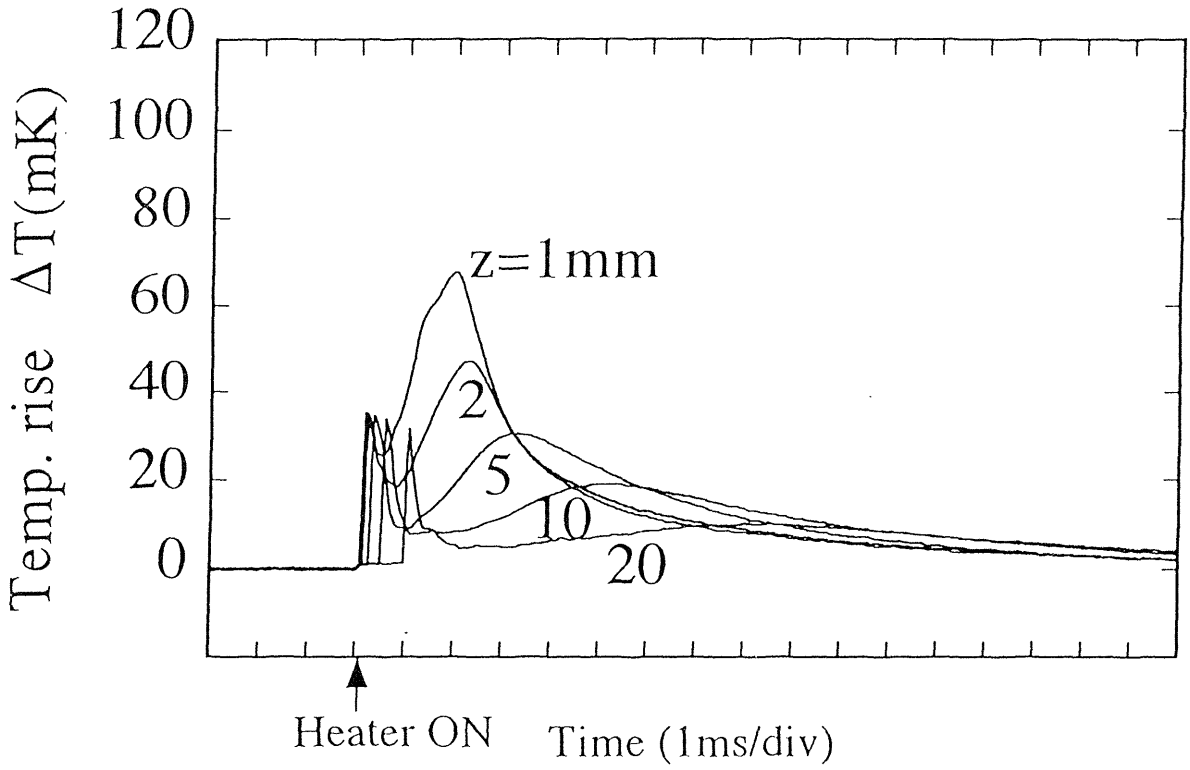

Figure 5.35 Superposed transient temperature traces measured at various location of a temperature sensor. $T_B = 1.70K$, $t_H = 1000\mu s$ and $q_p = 26W/cm^2$.

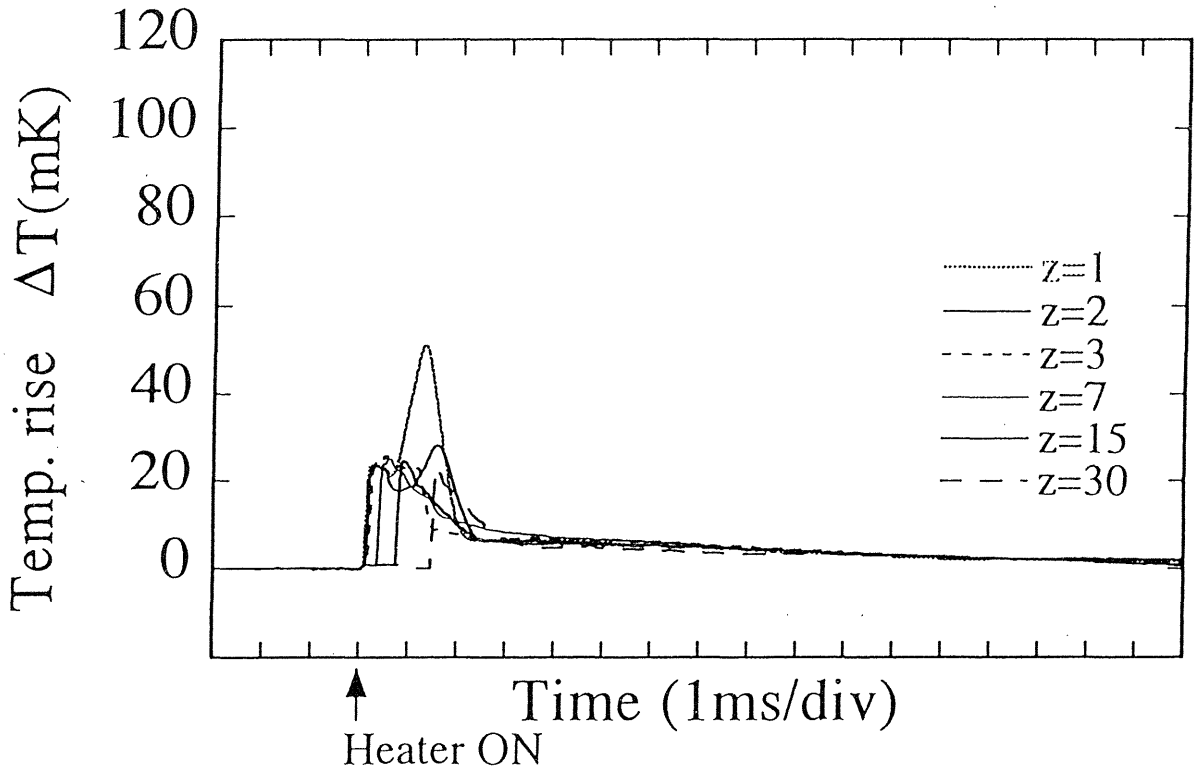

Figure 5.36 Superposed transient temperature traces measured at various location of a temperature sensor. The secondary temperature is only observed at $z = 1$ and $2mm$. $T_B = 1.70K$, $t_H = 1000\mu s$ and $q_p = 15W/cm^2$.

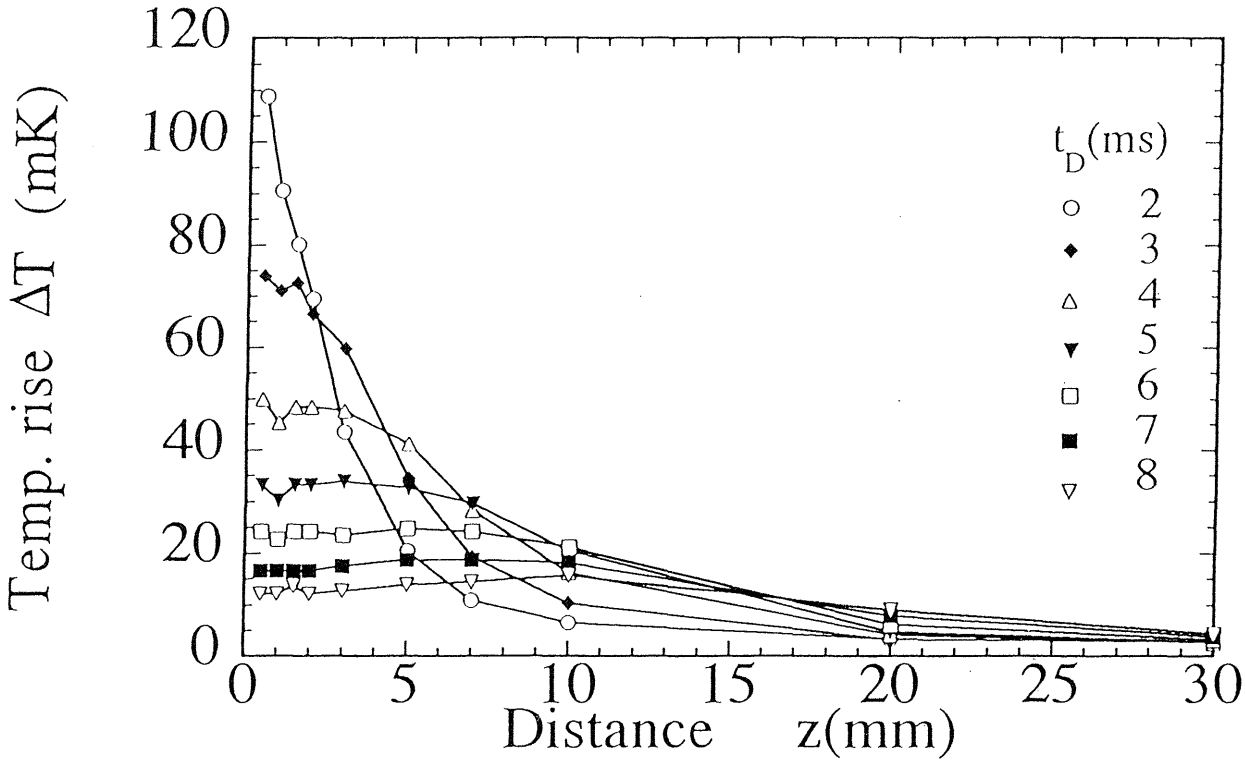

Figure 5.37 Time variation of temperature distribution near heater including a thermal boundary layer, taking t_D as a parameter. $t_D = 0$ corresponds to the onset of heating. $T_B = 1.70K$, $t_H = 1000\mu s$ and $q_p = 40W/cm^2$.

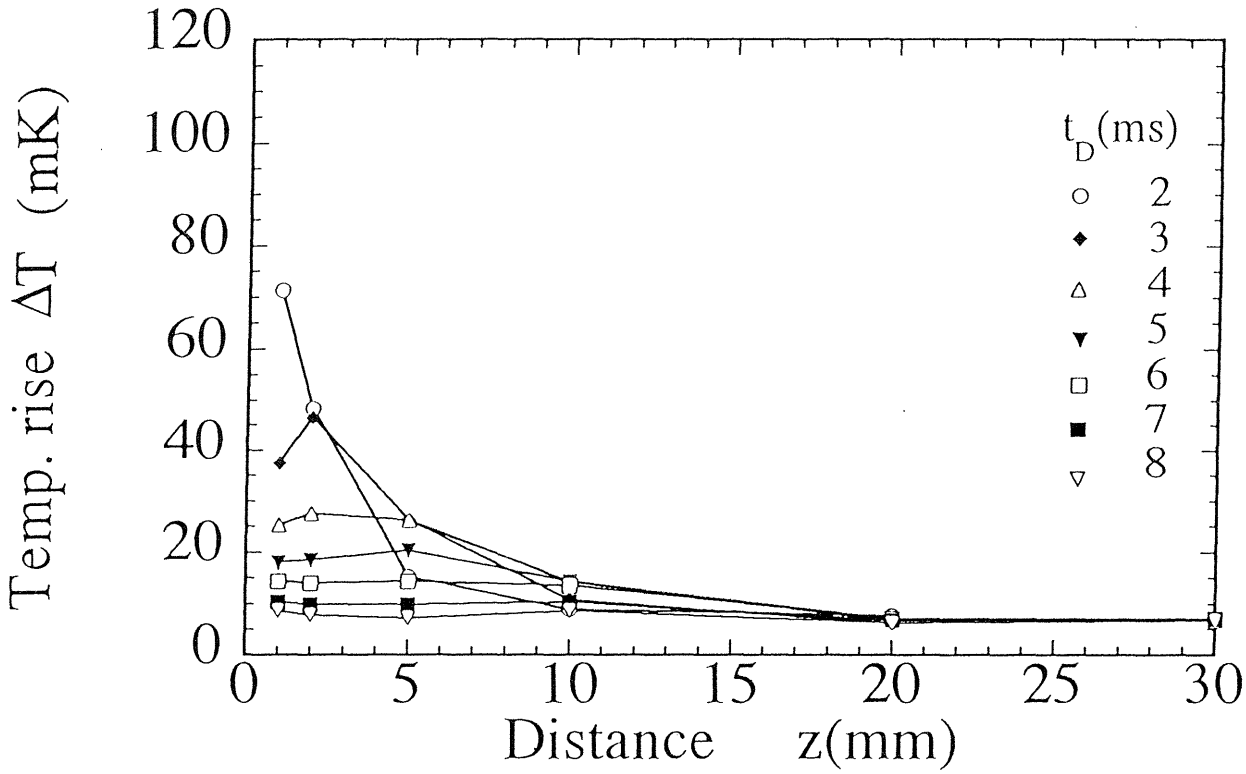

Figure 5.38 Time variation of temperature distribution near heater including a thermal boundary layer, taking t_D as a parameter. $T_B = 1.70K$, $t_H = 1000\mu s$ and $q_p = 20W/cm^2$.

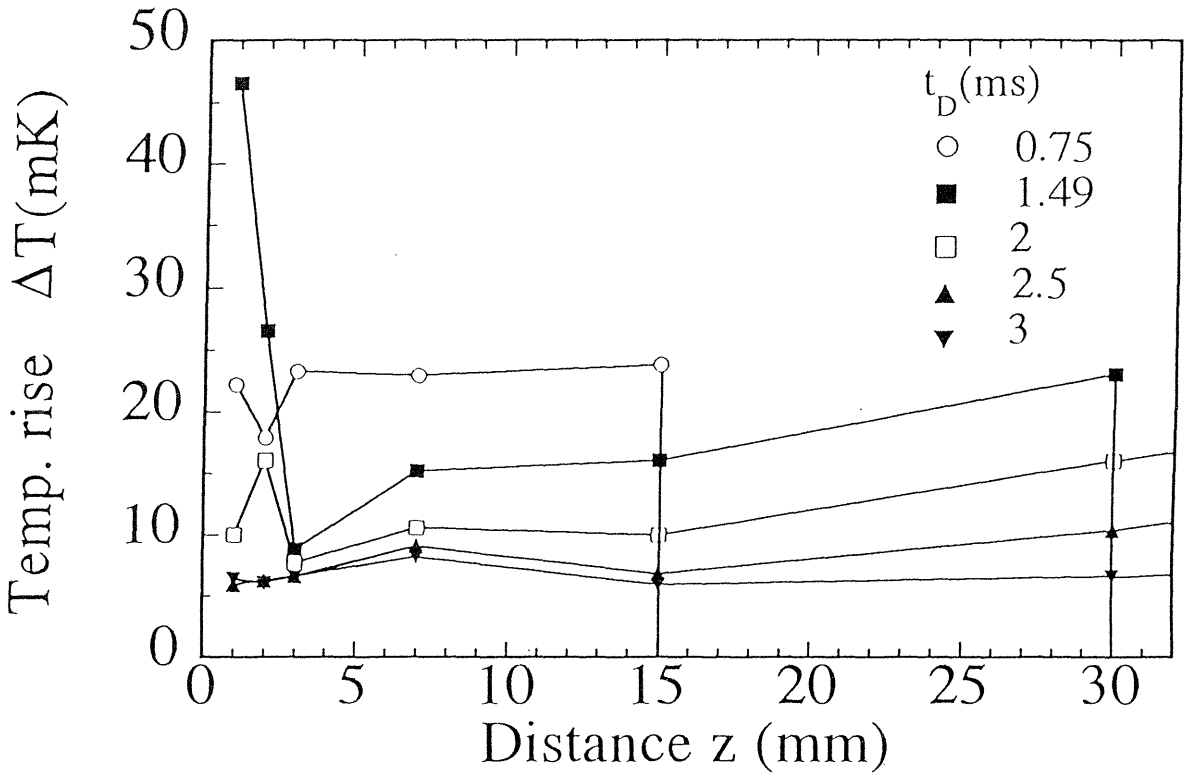

Figure 5.39 Time variation of temperature distribution near heater taking t_D as a parameter. Since the applied heat flux is not sufficiently large to generate dense quantized vortices, major part of the input heat is transported by a second sound wave in this case. $T_B = 1.70K$, $t_H = 1000\mu s$ and $q_p = 15W/cm^2$.

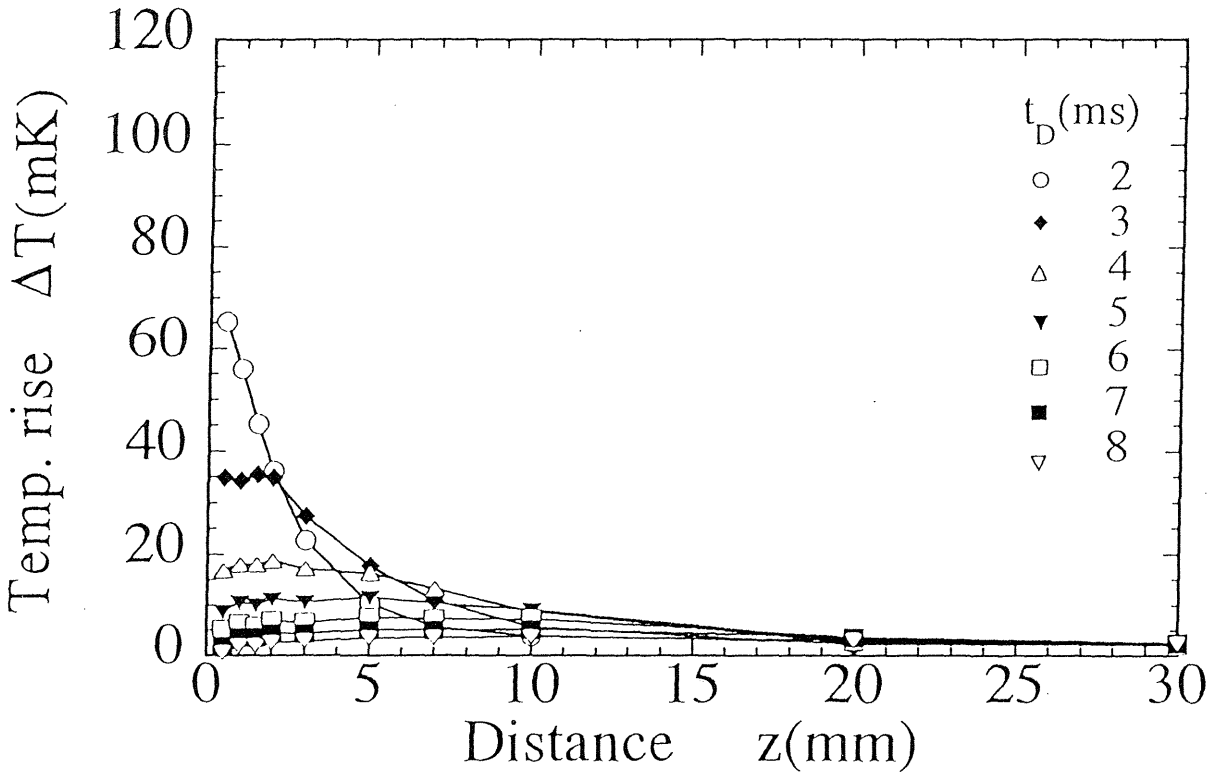

Figure 5.40 Time variation of temperature distribution near heater including a thermal boundary layer, taking t_D as a parameter. It is qualitatively the same for $T_B = 1.70K$, but quantitatively is not quite same. $T_B = 1.90K$,

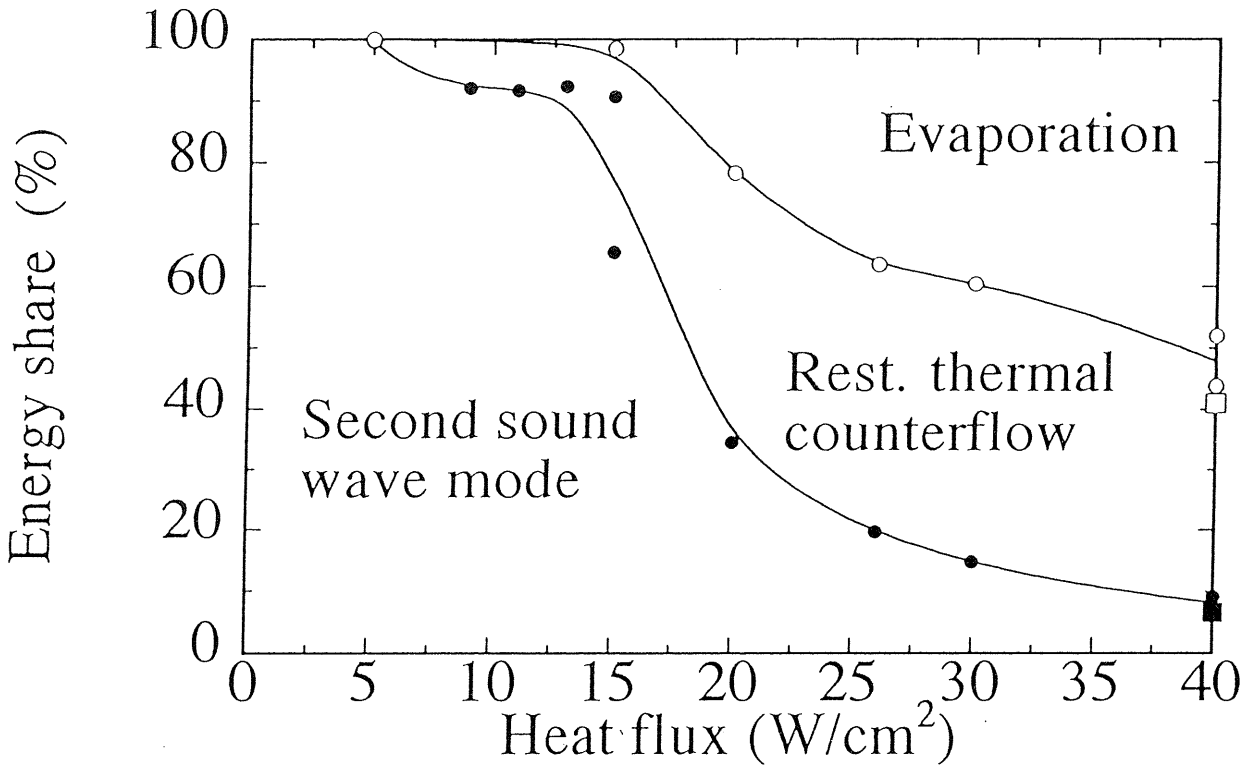

Figure 5.41 Ratio of amount of heat transported by each process. Filled symbols indicate the boundary between the second sound wave mode and that of the restricted thermal counterflow. Open symbols indicate the boundary between of the restricted thermal counterflow and that of evaporation. $T_B = 1.70K$, $t_H = 1000\mu s$. A set of points obtained at $T_B = 1.90K$ (denoted by squares) is also included for comparison.

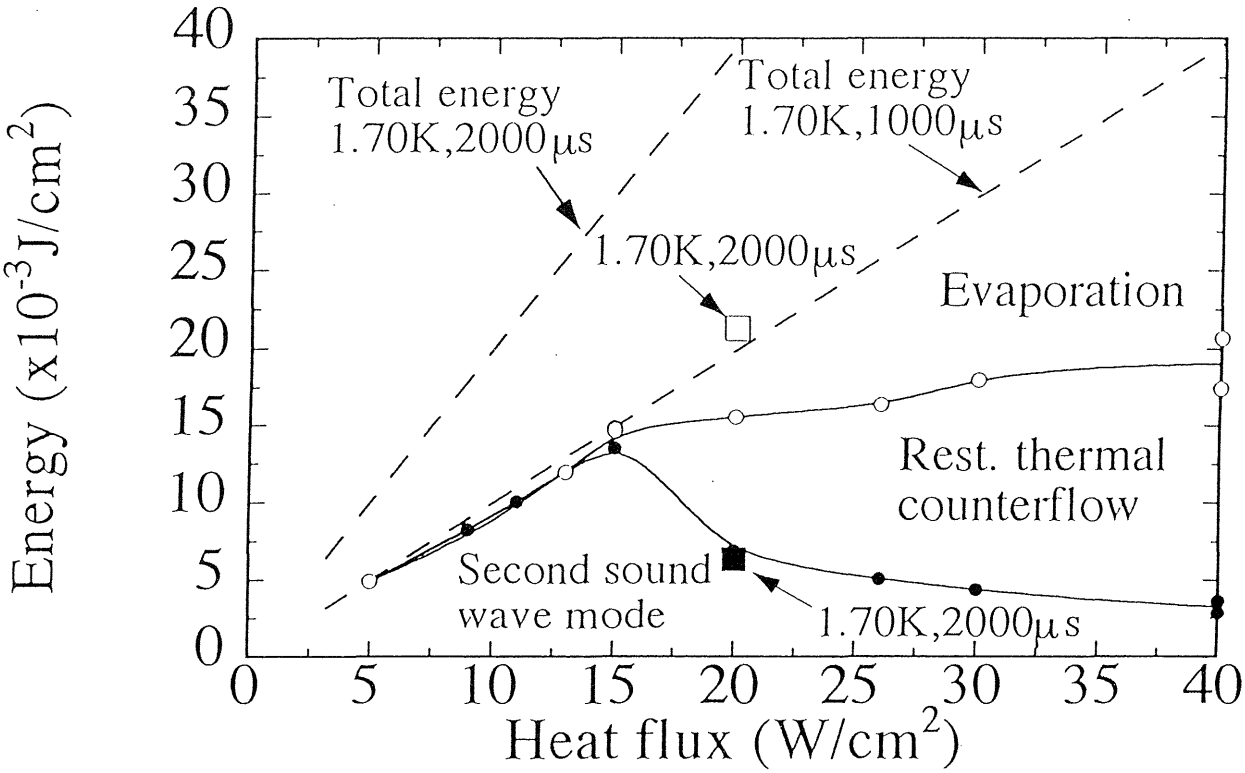

Figure 5.42 Absolute amount of heat transported by the three processes. Most of data plotted are those obtained at $T_B = 1.70K$, $t_H = 1000\mu s$, with a pair of data for $t_H = 2000\mu s$, $q_p = 20W/cm^2$ (denoted by squares) added for reference. Broken lines represent the total amount of heat transported per unit area for two cases of heating time.

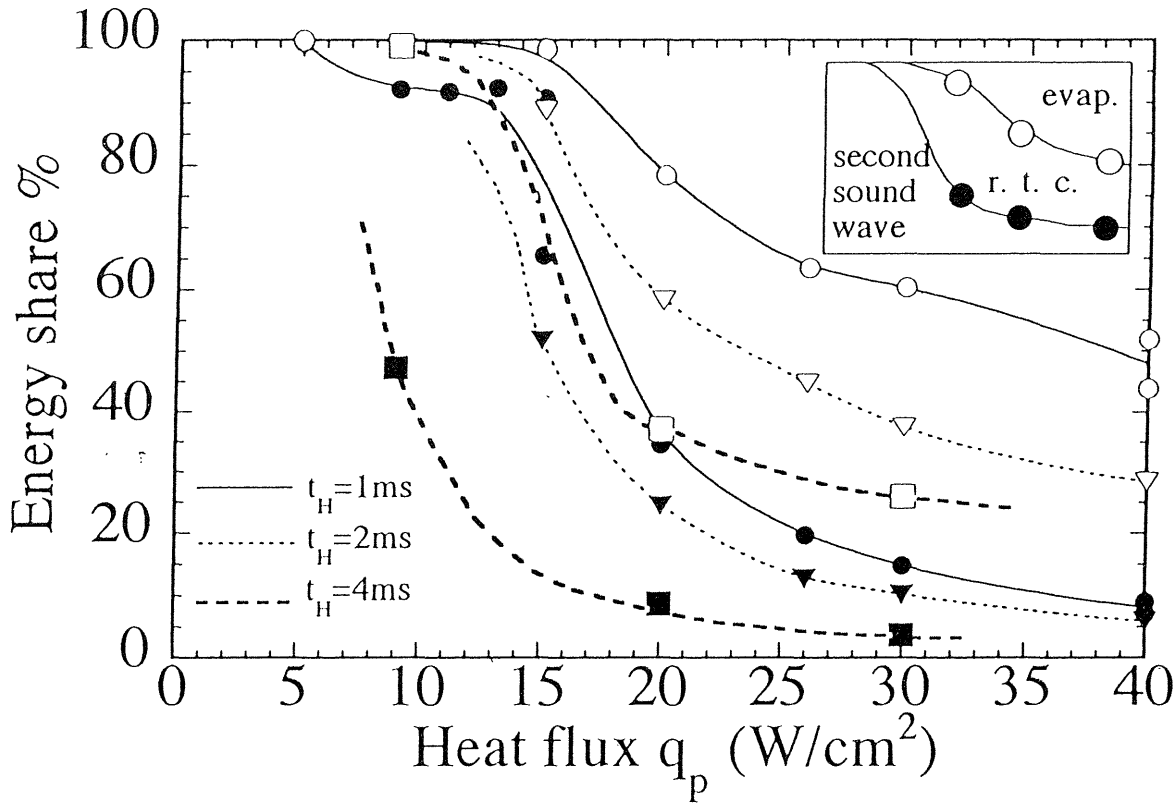

Figure 5.43 Ratio of amount of heat transported by the three processes for various heating time of $t_H = 1$, 2 and $4ms$. Filled symbols indicate the boundary between the second sound wave mode and that of the restricted thermal counterflow. Open symbols indicate the boundary between the restricted thermal counterflow and that of evaporation. Those boundaries are schematically drawn in the inset of the figure. (○ ●) : $t_H = 1ms$, (▽ ▼) : $t_H = 2ms$, (□ ■) : $t_H = 4ms$ and $T_B = 1.70K$.

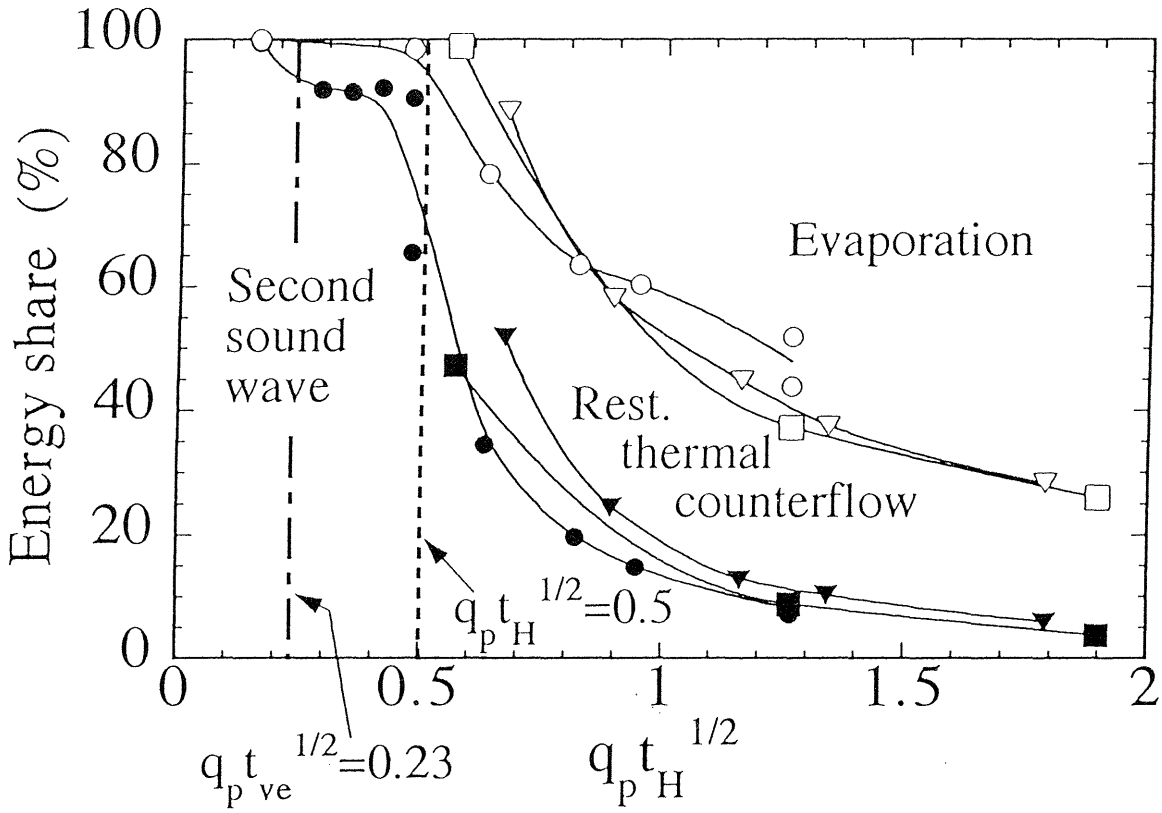

Figure 5.44 Ratio of the amount of heat transported by each process. The parameter of $q_p t_H^{\frac{1}{2}}$ are introduced as the abscissa. The dotted broken line indicates the value of $q_p t_H^{\frac{1}{2}}$ at which quantized vortex lines are dense enough to interact with a thermal shock wave according to the Fig. 5.13. The broken line represents the criterion of the onset of boiling obtained empirically by Tsoi and Lutset (○ ●) : $t_H = 1ms$, (▽ ▼) : $t_H = 2ms$, (□ ■) : $t_H = 4ms$ and $T_B = 1.70K$.

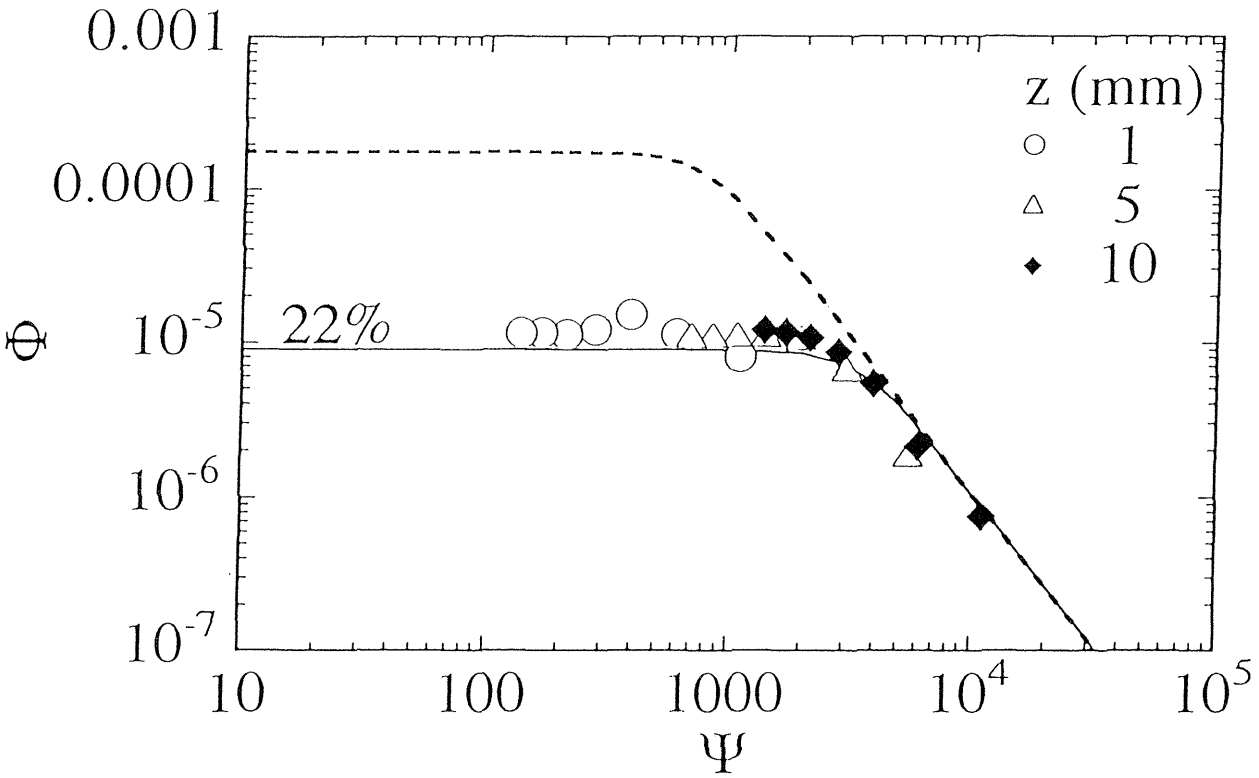

Figure 5.45 Comparison of the experimental data and the analytical solution. Experimental data obtained at the sensor location of, z of 1, 5 and $10mm$ are plotted. The theoretical curves represented by dotted and solid lines. The dotted line obtained by regarding the total input heat as Q. According to the Fig. 5.44, 22% of the applied heat is transported by the restricted thermal counterflow in this case. The solid line represents the analytical solution obtained by using the 22% of the applied heat as Q. $T_B = 1.70K$, $q_p = 40W/cm^2$ and $t_H = 2000\mu s$.

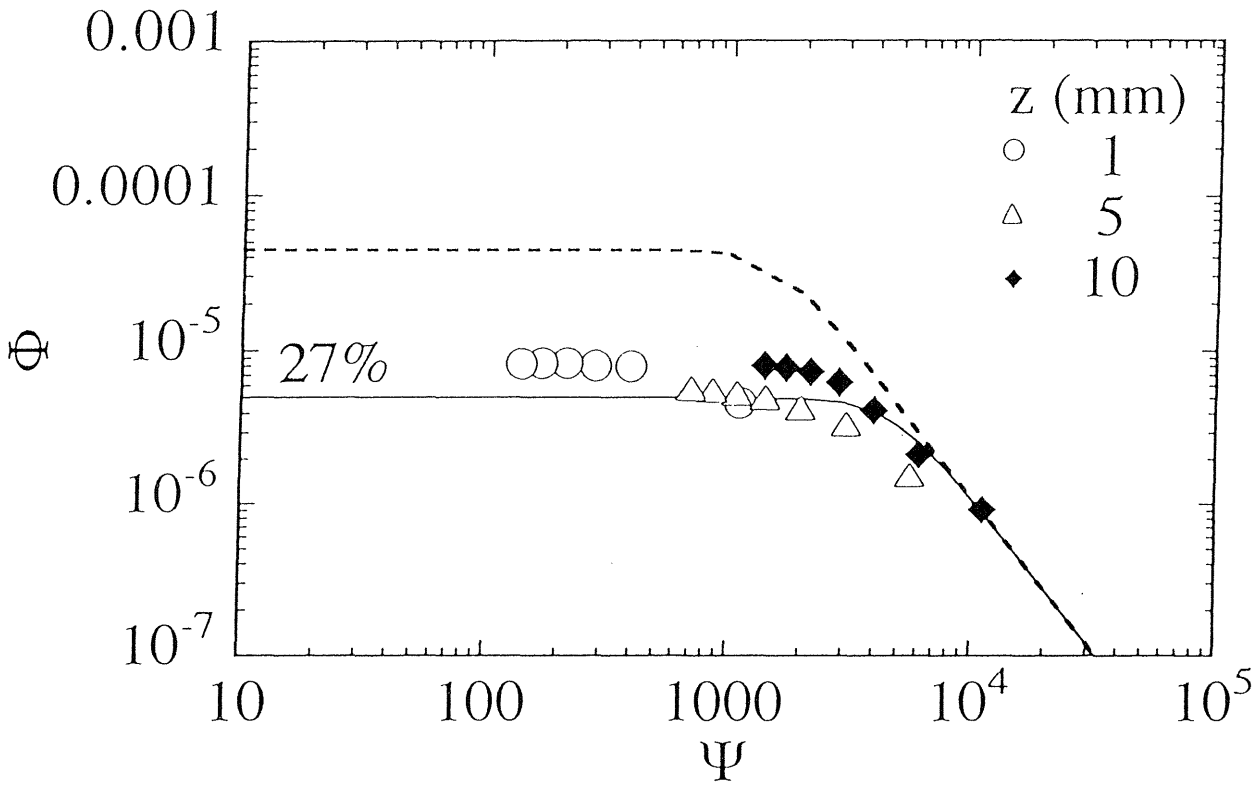

Figure 5.46 Comparison of the experimental data and the analytical solution in the case of $q_p = 20W/cm^2$. The amount of heat transported by the restricted thermal counterflow is 27% in this case. Other conditions are the same as those of Fig. 5.45.

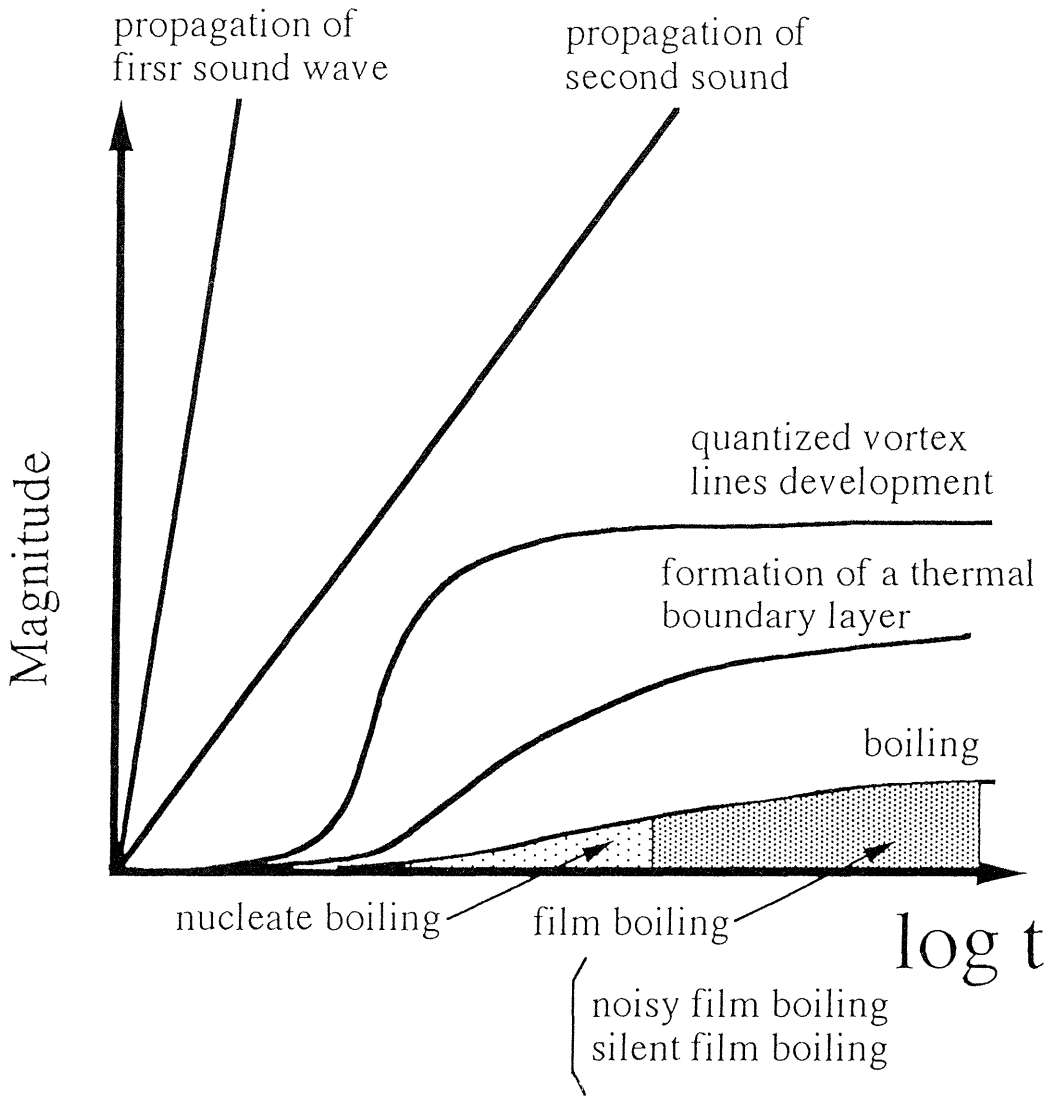

Figure 5.47 Schematic drawing of a series of highly transient thermo-fluid phenomena in He II occurring after the intense pulsed heating. The ordinate represents the magnitude of the physical quantity of the each phenomenon. It represents the propagation distance for the first and second waves. It represents the vortex line density and the thickness of the thermal boundary layer for the quantized vortex line development and the formation of a thermal boundary layer, respectively. For the boiling the ordinate represents the radius of the vapor bubble and the thickness of the vapor layer. The abscissa represents the logarithmic time t after the onset of the intense pulsed heating.